Astronomy Letters, Vol. 31, No. 6, 2005, pp. 359–364. Translated from Pis'ma v Astronomicheskiĭ Zhurnal, Vol. 31, No. 6, 2005, pp. 403–409.

Recombination Dynamics of Primordial Hydrogen and Helium (He I) in the Universe

V. K. Dubrovich[1,2] and S. I. Grachev[3*]

[1] *Special Astrophysical Observatory, St. Petersburg Branch, Russian Academy of Sciences, St. Petersburg, 196140 Russia*

[2] *Pulkovo Astronomical Observatory, Russian Academy of Sciences, Pulkovskoe sh. 65, St. Petersburg, 196140 Russia*

[3] *Sobolev Astronomical Institute, St. Petersburg State University, Universitetskiĭ pr. 28, St. Petersburg, 198504 Russia*

Received December 24, 2004

Abstract—We calculated the ionization fraction for hydrogen and helium (He I) as a function of the redshift z by including the two-photon decays of high hydrogen and parahelium levels and the radiative transfer in the helium $2\,^3P_1 \leftrightarrow 1\,^1S_0$ intercombination line. We show that this yields corrections of no more than a few percent to the ionization fraction for hydrogen and speeds up significantly the recombination for helium compared to the recent works by Seager *et al.* (1999, 2000), in which these effects were disregarded.

Key words: *cosmology, early Universe, primordial helium, recombination, radio astronomy, cosmic microwave background radiation.*

INTRODUCTION

The recombination dynamics of primordial hydrogen and helium in the Universe has been considered in several papers (for a brief overview and a list of references, see Seager *et al.* 2000). However, new and more accurate and detailed studies of this process are still of interest. This is attributable to the increasing accuracy of new cosmic microwave background radiation (CMBR) measurements aimed at separating the contributions from various new fundamental physical factors—hidden matter, dark energy, etc.

Seager *et al.* (2000) performed the most detailed calculations of the matter recombination dynamics in the Universe by numerically solving a system of nonstationary equations for the hydrogen (300), He I (200), and He II (100) level populations, the electron, proton, H^-, H_2, and H_2^+ densities together with an equation for the matter temperature. The mean intensity of the radiation was assumed to be Planckian, except the frequencies in the resonance lines, for which Sobolev's approximation was used. The authors took into account both radiative and collisional transitions; however, the contribution from the latter was insignificant (a result obtained previously by other authors). It should be emphasized that both singlet (parahelium) and triplet (orthohelium) states were included for He I.

The main result from Seager *et al.* (2000) regarding the He I recombination is that it is much slower than that in the equilibrium case (according to Saha's formula) and slower than that obtained by other authors. In this case, the transitions from the second parahelium level, the two-photon ($2\,^1S_0 \leftrightarrow 1\,^1S_0$) ones and those in the resonance line ($2\,^1P_1 \leftrightarrow 1\,^1S_0$), act as the main regulators of the recombination rate. It turned out that (as with hydrogen) the results of multilevel calculations could be satisfactorily described in terms of an effective three-level model atom (which was suggested previously for hydrogen by Peebles (1968) and Zel'dovich *et al.* (1968)) for parahelium with the appropriate fitting of the total recombination coefficient to all upper levels. Therefore, Seager *et al.* (1999) developed a simplified code, recfast.for, for computing the recombination dynamics in terms of the effective three-level model atoms of hydrogen (the $1s$, $2s$, $2p$ levels plus the combined continuum of the higher levels) and helium (the $1s\,^1S_0$, $2s\,^1S_0$, $2p\,^1P_1$ levels plus the combined continuum of the higher parahelium levels).

In this paper, we study the influence of additional factors, namely, the two-photon transitions from high hydrogen and parahelium levels to the ground state and the radiative transfer in the helium $2\,^3P_1 \leftrightarrow 1\,^1S_0$

*E-mail: stas@astro.spbu.ru

intercombination line, on the hydrogen and helium (He I) recombination dynamics. These factors were not included explicitly in the recfast.for code by Seager *et al.* (1999) and were probably disregarded in their multilevel calculations (Seager *et al.* 2000). We considered how these factors could be included in the recfast.for code and obtained a significant speedup of the He I recombination. We also wrote our own code for computing the helium recombination dynamics by including all of the factors mentioned above. Our code yielded results that agreed closely with those obtained with the modified recfast.for code.

BASIC EQUATIONS AND RELATIONS

The nonstationary equation for the ionization fraction of a chemical element (hydrogen or helium), $y = N^+/N$, in a homogeneous expanding Universe can be written as

$$(1+z)H(z)N(z)\frac{dy}{dz} = \sum_i R_i, \qquad (1)$$

where N is the total number density of its atoms and ions, N^+ is the number density of its ions, $H(z)$ is the Hubble factor, z is the redshift, and R_i is the number of uncompensated transitions from level i to the ground level 1 that determine the irreversible recombination. The relation $dz/dt = -(1+z)H(z)$ was used to pass from the time scale t to the redshift scale.

Equation (1) is valid under the assumption that the level populations of excited states satisfy the (stationary) statistical equilibrium equations at the current electron and ion number densities. This assumption in fact holds, since the population of excited states is determined by the permitted transitions (in a blackbody background radiation field), while the electron and ion number densities are determined by the much slower two-photon transitions and by the redshift of resonance photons due to the expansion of the Universe. We consider only radiative transitions, because collisional transitions are known (see, e.g., Seager *et al.* 2000) to play no role. In this case,

$$R_i = N_i(A_{i1} + B_{i1}J_{1i}) - N_1 B_{1i} J_{1i}, \qquad (2)$$

where N_i is the population of the ith level; A_{i1}, B_{i1}, and B_{1i} are the Einstein coefficients of the transitions between the ith and first levels; and J_{1i} is a "mean" intensity of the radiation at the transition frequency.

Until now, the two-photon decay of the second level ($2\,^1S_0$ for helium) and the redshift of photons in the principle resonance line ($2\,^1P_1 \to 1\,^1S_0$ for helium) have been considered as the only regulators of the hydrogen and helium recombination rates (see, e.g., Seager *et al.* (2000) and references therein). However, it is clear that similar processes should also be taken into account for the higher hydrogen and parahelium levels. In addition, as we show below, the intercombination transition from the lower state of orthohelium, $2\,^3P_1 \to 1\,^1S_0$, also plays a prominent role.

For two-photon transitions, Eq. (2) can be rewritten as

$$R_i^{(2q)} = N_i A_{i1}^{(2q)} \times \left[1 - \frac{N_1 g_i}{N_i g_1} e^{-h\nu_{1i}/kT}\right] \Big/ (1 - e^{-h\nu_{1i}/kT}); \qquad (3)$$

the reverse process is assumed to be the capture of two blackbody photons (with temperature T) with the total energy equal to the transition energy $h\nu_{1i}$. Here, ν_{1i} is the transition frequency, and g_i is the statistical weight of the ith level.

For the resonance transitions in the approximation of a complete frequency redistribution during scattering and on the condition that the intensity of the radiation in the short-wavelength line wing tends to the Planck function, we have

$$R_i = \beta_{1i} N_i A_{i1} \times \left[1 - \frac{N_1 g_i}{N_i g_1} e^{-h\nu_{1i}/kT}\right] \Big/ (1 - e^{-h\nu_{1i}/kT}), \qquad (4)$$

where β_{1i} is the probability of photon escape from the scattering process due to the expansion of the medium (the Universe). It is defined via the Sobolev optical depth τ_{ik}:

$$\beta_{ik} = (1/\tau_{ik})\left(1 - e^{-\tau_{ik}}\right), \qquad (5)$$
$$1/\tau_{ik} = \frac{4\pi}{hc}\frac{H(z)}{N_i B_{ik}}\left(1 - \frac{N_k g_i}{N_i g_k}\right)^{-1}.$$

Relations (4) and (5) correspond to the approximation of Sobolev (1947) (see also the review by Grachev (1994) devoted to generalizations of this approximation), although it yields an exact solution in terms of the kinematics (uniform expansion) under consideration. Substituting (5) in (4) yields

$$R_i = \frac{8\pi H(z)}{\lambda_{1i}^3}\frac{g_1 N_i}{g_i N_1}(1 - e^{-\tau_{1i}}) \times \frac{1 - (N_1 g_i/N_i g_1)e^{-h\nu_{1i}/kT}}{1 - N_i g_1/N_1 g_i} \Big/ (1 - e^{-h\nu_{1i}/kT}), \qquad (6)$$

where the transition wavelength $\lambda_{1i} = c/\nu_{1i}$. Since $h\nu_{1i} \gg kT$ and $N_i \ll N_1$ for the energy and the populations of excited states, respectively, even at the onset of He^+ recombination (at $z \approx 2700$), we may disregard the exponential term compared to unity in the last factor in Eqs. (3) and (6) and the second term in the denominator of the fraction in Eq. (6). The formulas mentioned above can then be rewritten as

$$R_i^{(2q)} = N_i A_{i1}^{(2q)}[1 - (N_1 g_i/N_i g_1)e^{-h\nu_{1i}/kT}] \qquad (7)$$

and

$$R_i = \frac{8\pi H(z)}{\lambda_{1i}^3}\frac{g_1 N_i}{g_i N_1}(1 - e^{-\tau_{1i}}) \times [1 - (N_1 g_i/N_i g_1)e^{-h\nu_{1i}/kT}], \quad (8)$$

where $N_1 = N - N^+$, since the overwhelming majority of neutral hydrogen and helium atoms (at the recombination epoch) are in the ground state.

Thus, the problem is reduced to solving Eq. (1) with R_i on the right-hand side given by formulas (7) and (8); the populations of excited states on the right-hand sides of these formulas can be determined from the statistical equilibrium equations at the current electron and ion number densities. Note that we used this approach previously (Grachev and Dubrovich 1991) to compute the hydrogen recombination dynamics in terms of a 60-level model atom. However, during almost the entire helium recombination period ($z = 2700-1800$), the radiation temperature remains high enough for the populations of excited He I states (offset by less than 5 eV from the continuum) to be close to their equilibrium values (with respect to the continuum), i.e., to be defined by the Boltzmann–Saha formulas at the electron temperature equal to the radiation temperature ($T_e = T$):

$$N_i = N_e N^+ \frac{g_i}{2g^+ g(T_e)} e^{h\nu_{ic}/kT_e}, \quad (9)$$

$$g(T_e) = (2\pi m k T_e)^{3/2}/h^3,$$

where N_e is the electron number density, and $h\nu_{ic}$ is the threshold energy of ionization from the ith level. Formulas (7) and (8) can then be rewritten as

$$R_i^{(2q)} = \frac{N(1-y)}{r_1} g_i A_{i1}^{(2q)} e^{h\nu_{ic}/kT} \times (1 - r_1 e^{-h\nu_{1c}/kT}), \quad (10)$$

$$R_i = \frac{8\pi H(z)}{\lambda_{1i}^3}\frac{1}{r_1} e^{h\nu_{ic}/kT} \times (1 - e^{-\tau_{1i}})(1 - r_1 e^{-h\nu_{1c}/kT}), \quad (11)$$

where $r_1 = (2g^+/g_1)g(T_e)(1-y)/(N_e y)$.

Since it is important to take into account the two-photon transitions from high helium levels, we give below a brief derivation of the formulas for the transition probabilities according to Dubrovich (1987). The simultaneous emission of two photons by excited atoms has long been known and described in textbooks (see Berestetskii *et al.* 1982). The role of this process in the hydrogen atom in producing continuum radiation in the interstellar medium (Kipper 1950) and in the early Universe (Zel'dovich *et al.* 1968) has also been known for a long time. However, only one hydrogen state, $2s$, is taken into account in these specific cases. At the same time, as Dubrovich (1987) showed, similar decays of higher levels can also make a significant and, in several cases, major contribution at certain parameters of the medium and the CMBR. Here, we consider this question only for the hydrogen and helium recombination dynamics in the early Universe.

It follows from the quantum-mechanical selection rules that, in fact, we must consider only the is and id states. According to Berestetskii *et al.* (1982) (Eq. (59.28)), the exact expression for the probability of a spontaneous two-photon transition can be written as

$$dW = \frac{2^{10}\pi^6 \nu^3 \nu'^3}{9h^2c^6} \times \left| \sum_{i',l'} \left[\frac{(d_\alpha)_{1s,i'l'}(d_\beta)_{i'l',il}}{\nu_{i'l',il} + \nu} + \frac{(d_\beta)_{1s,i'l'}(d_\alpha)_{i'l',il}}{\nu_{i'l',il} + \nu'} \right] \right|^2 d\nu, \quad (12)$$

where $\nu + \nu' = \nu_{il,1s}$; the subscripts il, $i'l'$, and $1s$ number the initial, intermediate, and final atomic states (i is the principal quantum number, and l is the orbital angular momentum); $(d_\alpha)_{il,i'l'}$ is the matrix element of the dipole moment; α and β number the spatial components of the dipole moment vector; ν and ν' are the frequencies of the emitted photons; h is Planck's constant; and c is the speed of light. The sharp maxima in Eq. (12) at ν or $\nu' = \nu_{ii'}$ correspond to the resonances of the cascade transition from the excited level downward with the emission of photons of a discrete atomic spectrum. The high transition probability corresponding to them for specific quasi-equilibrium conditions with external Planckian radiation also leads to a high capture probability of the same photons. Strictly speaking, this question should be studied in more detail, since the transition near but not quite at the resonance, can make a contribution through the Lyman photon escape into the wing. In principle, this additionally speeds up the recombination dynamics. However, a detailed analysis requires solving the transfer equations, which will be done in the next paper. Here, we consider only the transitions that give a continuous distribution of the emitted photons; i.e., we restrict our analysis to the case $\nu_{i1} - \nu' \sim \nu$. As a result, the derived recombination rate may be considered a lower limit.

Since we are interested in the two-photon transitions to the final state with a zero orbital angular momentum (the s state), according to the selection rules for dipole transitions, l can be only 0 (the s state) or 2 (the d state). For both values, l' can be only 1 (the p state). In this case, the expression for W is simplified significantly. It can be simplified even further

if we note that, according to the sum rule for dipole transitions (Berestetskii *et al.* 1982; Eq. (52.8)), the transitions from $i' = i$ give about 90% of the contribution (Berestetskii *et al.* 1982; Eq. (52.6)). As a result, we obtain an expression for the structure of the matrix element that is well known for the $2s - 1s$ transition in hydrogen. In our case, to calculate W, we must only take into account the frequency difference, i.e., multiply $A_{2s,1s}$ by $(\nu_{i1}/\nu_{21})^5$ and add up the two decay channels (from the s and d sublevels) with their statistical weights. Finally, we obtain the following expression for hydrogen:

$$W_{\rm H} \equiv g_i A_{i1}^{(2q)} = 54 A_{2s,1s} \left(\frac{i-1}{i+1}\right)^{2i} \frac{11i^2-41}{i}. \quad (13)$$

At large i, we have an approximate value of $W_{\rm H} = 89i\ {\rm s}^{-1}$. In fact, $W_{\rm H}$ increases with level number only to a certain value of i. This is because the dipole approximation has a validity limit—the wavelength of the emitted photon (in our case, $\sim 2/\nu_{i1} \to$ const) must be larger than the orbital size of the excited state ($\sim i^2$). For hydrogen, $i_{\max} \sim 30$ (Beigman and Syrkin 1983).

A similar analysis can also be performed for the decays of hydrogenic He I states. For $i > 6$–7, this approximation is quite legitimate for the matrix elements $i(s,d) - ip$. It also becomes accurate enough for our purposes for the square of the matrix element $ip \to 1s$ if we apply a correction by a factor of 1.15–1.20 that follows from a comparison of the tabulated oscillator strengths of these transitions for He I and hydrogen. Of course, we must again renormalize (13) to the frequency of the emitted photons, i.e., multiply W for hydrogen by $(24.6/13.6)^5 = 19.4$. Finally, we obtain for $W_{\rm He\,I}$

$$W_{\rm He\,I} \equiv g_i A_{i1}^{(2q)} = 1045 A \left(\frac{i-1}{i+1}\right)^{2i} \frac{11i^2-41}{i}. \quad (14)$$

The condition constraining i is here the same as that for hydrogen. If the validity condition for the dipole approximation (for $i < 40$) is satisfied, then $A = 10\ {\rm s}^{-1}$ should be taken in Eq. (14). Otherwise, there is an uncertainty attributable to the theoretically poorly calculated and experimentally unknown change of A with level number. The contribution from these levels (with $i > 40$) is most likely moderate. It can be approximately included by taking $A = 12\ {\rm s}^{-1}$. However, for highly accurate measurements of the power spectrum to obtain information about weak, but fundamentally important factors, A must be analyzed further.

The influence of the two-photon decays of upper levels on the recombination dynamics must be more significant for He I than for hydrogen. This is attributable to two factors. First, the absolute value of W is much higher. Second, the relationships between the populations of the $2s$ level and the Rydberg levels differ significantly, since the ratio of these populations contains the Boltzmann factor $\exp(-h\nu_{i2}/kT_r)$. This ratio is about 3×10^{-5} for hydrogen and is a factor of 85 larger for He I, for which the absolute value of the energy difference is approximately the same, but its recombination temperature is much higher. The contribution to the destruction rate of "superfluous" Lyman photons is determined by the product of the population by the decay probability.

We wrote a code for solving Eq. (1) for helium with terms of forms (10) and (11) on the right-hand side; apart from the two-photon transitions from the second parahelium level ($i = 2s \leftrightarrow 1$), we also included the transitions from higher levels ($i = 6$–40), which were assumed to be hydrogenic (Rydberg) ones. We take $h\nu_{ic} \approx 1{\rm Ry}/i^2$ for their energy measured from the ionization threshold and use formula (14) for the Einstein coefficients. In addition, apart from the resonance transition from the second parahelium level, $i = 2p\,^1P_1 \leftrightarrow 1s\,^1S_0$ (below, we write $i = 2p \leftrightarrow 1$ for simplicity), we also included the spin-forbidden one-photon transition from the second orthohelium level, $2p\,^3P_1 \leftrightarrow 1s\,^1S_0$, for which the Einstein coefficient is $A_{2\,^3P_1,1\,^1S_0} = 233\ {\rm s}^{-1}$ (Lin *et al.* 1977). It should be noted that we used Saha's formula (equilibrium ionization) for the hydrogen ionization fraction, which appears in $N_e = N_{\rm H}^+ + N_{\rm He}^+$; this is valid for fairly high z at which the He I recombination mainly takes place.

We also made appropriate modifications to the recfast.for code by Seager *et al.* (1999), in which the two-photon transitions from the second level alone ($i = 2s \leftrightarrow 1$) were included; the Einstein coefficients $A_{2s,1}^{(2q)}$ for hydrogen and parahelium ($\Lambda_{\rm H}$ and $\Lambda_{\rm He\,I}$ in the notation of Seager *et al.* (1999)) are $\Lambda_{\rm H} = 8.22\ {\rm s}^{-1}$ and $\Lambda_{\rm He\,I} = 51.3\ {\rm s}^{-1}$. Clearly, to include the two-photon transitions from higher levels, we must make the following substitution according to formula (10):

$$\Lambda \to \Lambda + \sum_{i=i_0}^{i_N} g_i A_{i1}^{(2q)} e^{h(\nu_{ic}-\nu_{2s,c})/kT}. \quad (15)$$

In the recfast.for code, the contribution from the $i = 2p \leftrightarrow 1$ transition for hydrogen and parahelium is described by the factors $K_{\rm H}$ and $K_{\rm He\,I}$, where $K = \lambda_{1,2p}/[8\pi H(z)]$. Therefore, according to formula (11), the contribution from other lines (for one-photon

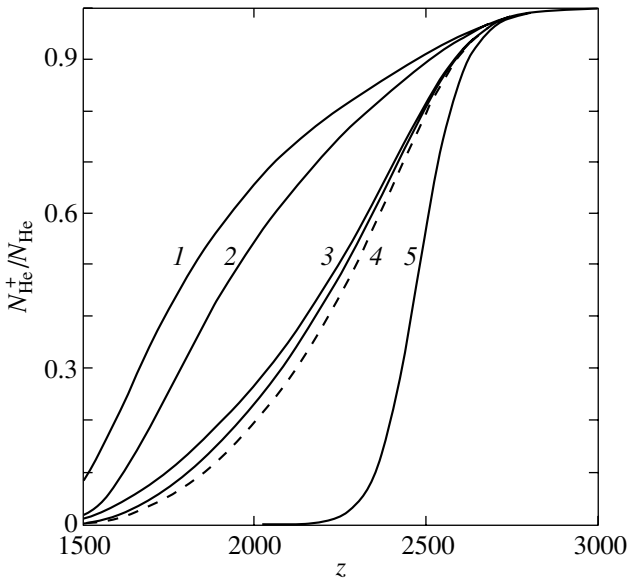

Fig. 1. Profiles of the helium ionization fraction. The numbers near the curves are: *1*—according to the standard recfast.for code; *2*, *3*, *4*—with the inclusion of additional channels of irreversible recombination (see also the text); *5*—the equilibrium case (Saha's equation). For the parameters, see the text.

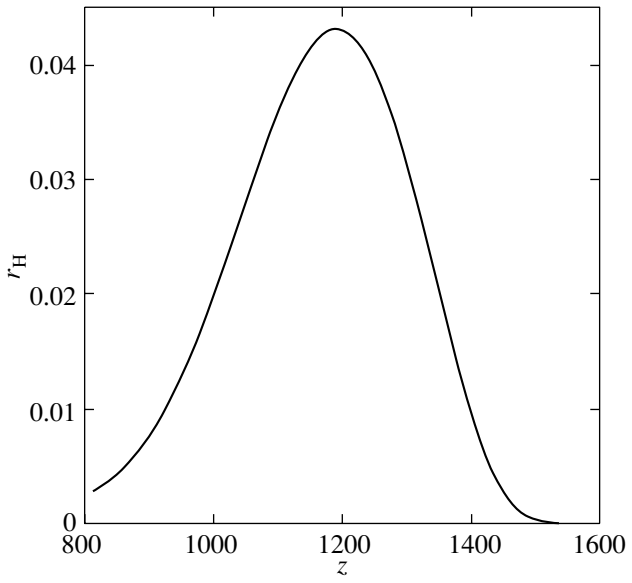

Fig. 2. Influence of additional transitions on the profile of the ionization fraction $y_H = N^+_H/N_H$. $r_H = 2(y^{old}_H - y^{new}_H)/(y^{old}_H + y^{new}_H)$, where y^{old}_H corresponds to the basic $2s \leftrightarrow 1$ and $2p \leftrightarrow 1$ transitions alone, and y^{new}_H corresponds to the basic transitions plus the transitions from high levels, is along the vertical axis. The values of the parameters are the same as those for Fig. 1.

transitions) can be included by the substitution

$$\frac{1}{K} \to \frac{1}{K}\left[1 + \sum_i \left(\frac{\lambda_{1,2p}}{\lambda_{1i}}\right)^3 e^{h(\nu_{ic}-\nu_{2p,c})/kT} \times \frac{1-e^{-\tau_{1i}}}{1-e^{-\tau_{1,2p}}}\right]. \quad (16)$$

Since the optical depth is $\tau_{1,2p} \gg 1$ for the principal resonance transition throughout the recombination, the corresponding exponential term may be disregarded.

As our calculations show, the results obtained using our code and the recfast.for code modified in the above way are virtually identical (at the currently adopted model parameters of the Universe).

COMPUTATIONAL RESULTS

The parameters in the problem include the equilibrium CMBR temperature T_0, the Hubble factor H_0, the total-to-critical density ratio Ω_{total}, the baryon-to-critical density ratio Ω_B, the dark matter-to-critical density ratio Ω_{DM}, the Λ-to-critical density ratio Ω_Λ at the current epoch, and the mass fraction of primordial helium Y. We performed test calculations for $T_0 = 2.728$ K, $\Omega_{total} = 1$, $Y = 0.24$, $H_0 = 70$ km s^{-1} Mpc^{-1}, $\Omega_B = 0.04$, $\Omega_{DM} = 0.26$, and $\Omega_\Lambda = 0.7$.

Figure 1 shows the results of our calculations. The numbers correspond to the successive inclusion of irreversible helium recombination channels: *1*, only the basic $2s \leftrightarrow 1$ and $2p \leftrightarrow 1$ transitions of parahelium; *2*, the basic transitions plus the transition in the orthohelium line; *3*, the basic transitions plus the transitions from high parahelium levels ($i = 6$–40) at $A = 10$ s^{-1} in formula (14); *4*, the basic transitions plus the two additional channels (the solid and dashed lines for $A = 10$ s^{-1} and $A = 12$ s^{-1} in formula (14), respectively); and *5*, the equilibrium case (Saha's formula). We see from this figure that successively including the additional irreversible recombination channels increases significantly the He I recombination rate. Our results are virtually identical (indistinguishable in the figure) to those obtained with the recfast.for code, modified as described in the previous section.

Using the recfast.for code, we also included additional irreversible recombination channels for hydrogen, namely, the two-photon transitions from the $i = 3$–40 levels to the first level and the radiative transfer in the corresponding Lyman lines. We used (13) and (15) to include the first channel and (16) for the second channel; the exponentials in parentheses in these formulas may be disregarded, since the Sobolev optical depths in the Lyman lines $\tau_{1i} \gg 1$. The first and second channel were found to lead to a decrease in the hydrogen ionization fraction by less than 4.2%

and 1%, respectively, and, collectively, by less than 4.3% (for the same model parameters as those for helium). The results are shown in Fig. 2. Note that we additionally performed similar calculations using our code (Grachev and Dubrovich 1991), which is based on the solution of Eq. (1) together with the statistical equilibrium equations for the hydrogen level populations in terms of the 60-level model atom, and obtained virtually the same result as that in Fig. 2.

CONCLUSIONS

We computed the hydrogen and He I recombination dynamics by including the two-photon decays of high hydrogen and parahelium levels and the radiative transfer in the helium $2\,^3P_1 \leftrightarrow 1\,^1S_0$ intercombination line. This was shown to lead to changes in the hydrogen recombination rate that could be detected through the PLANCK program. The results obtained are of importance in correctly estimating the contribution from the small factors attributable to the presence of dark matter, the baryonic and nonbaryonic mass fractions in the Universe, and the fraction of relativistic (at the recombination epoch) particles—neutrinos, possibly axions, and other light, weakly interacting particles. Our calculations for helium show that including new overequilibrium Lyman photon destruction factors speeds up significantly the He I recombination compared to that predicted by Seager *et al.* (1999, 2000), who disregarded these effects. This is also of importance in correctly assessing the role of helium in the hydrogen recombination. In addition, this is of great importance in determining the profiles and intensities of the hydrogen and He I recombination lines. In particular, the large role of high levels in irreversible recombination gives rise to the absorption lines in the CMBR spectrum attributable to the transitions in Balmer lines and in various more complex helium lines. This is of fundamental importance in detecting and identifying such lines. The role of weakly nonresonance transitions from high levels, which can cause an additional increase in the recombination of both hydrogen and helium, should be considered as the next step in this direction.

As regards the effect of our refinements of the He I recombination dynamics on the theoretical CMBR power spectra, it can be roughly estimated from Fig. 17 in the paper by Seager *et al.* (2000), who compared their results with those obtained by Hu *et al.* (1995) under the assumption of equilibrium He I ionization (using Saha's formula). Since our helium ionization fraction profile lies almost in the middle between the equilibrium (Saha) profile and the profile by Seager *et al.* (see Fig. 1), one might expect the deviation from the results by Hu *et al.* (1995) with our refinements to decrease by a factor of about 2 (e.g., for the multipole number $l = 1500$, 1% will be instead of 2%). In this case, the uncertainty in A (see Fig. 1, curves *4*), which is estimated to be about 20%, will give the same relative uncertainty in the correction to the theoretical power spectrum.

ACKNOWLEDGMENTS

This work was supported by the Russian Foundation for Basic Research (project no. 02-02-16535, a Presidential Grant for the Support of Leading Scientific Schools (no. NSh-1088.2003.2), the federal Astronomy program, and State Contract no. 40.022.1.1.1106.

REFERENCES

1. I. L. Beĭgman and M. I. Syrkin, Preprint No. 295, FIAN (Lebedev Phys. Inst. USSR Acad. Sci., Moscow, 1983).
2. V. B. Berestetskii, E. M. Lifshits, and L. P. Pitaevskii, *Quantum Electrodynamics* (Nauka, Moscow, 1989; Pergamon Press, Oxford, 1982).
3. V. K. Dubrovich, Opt. Spektrosk. **63**, 439 (1987) [Opt. Spectrosc. **63**, 256 (1987)].
4. S. I. Grachev, Tr. Astron. Obs. Sankt-Peterburg. Gos. Univ. **44**, 203 (1994).
5. S. I. Grachev and V. K. Dubrovich, Astrofizika **34**, 249 (1991) [Astrophys. **34**, 124 (1991)].
6. W. Hu, D. Scott, N. Sugiyama, and M. White, Phys. Rev. D **52**, 5498 (1995).
7. A. Ya. Kipper, in *On the Development of Soviet Science in ESSR 1940–1950* (Tallin, 1950) [in Russian].
8. C. D. Lin, W. R. Johnson, and A. Dalgarno, Phys. Rev. A **15**, 154 (1977).
9. P. J. E. Peebles, Astrophys. J. **153**, 1 (1968).
10. S. Seager, D. D. Sasselov, and D. Scott, Astrophys. J. **523**, L1 (1999).
11. S. Seager, D. D. Sasselov, and D. Scott, Astrophys. J., Suppl. Ser. **128**, 407 (2000).
12. V. V. Sobolev, *Moving Stellar Envelopes* (Leningr. Gos. Univ., Leningrad, 1947) [in Russian].
13. Ya. B. Zel'dovich, V. G. Kurt, and R. A. Sunyaev, Zh. Éksp. Teor. Fiz. **55**, 278 (1968) [Sov. Phys. JETP **28**, 146 (1968)].

Translated by V. Astakhov

Astronomy Letters, Vol. 31, No. 6, 2005, pp. 365–374. Translated from Pis'ma v Astronomicheskiĭ Zhurnal, Vol. 31, No. 6, 2005, pp. 410–421.

Analysis of the Spatial Distribution of Gamma-Ray Bursts in Their Host Galaxies

S. I. Blinnikov[1], K. A. Postnov[2], D. I. Kosenko[1,2*], and O. S. Bartunov[2]

[1] *Institute for Theoretical and Experimental Physics, ul. Bol'shaya Cheremushkinskaya 25, Moscow, 117218 Russia and MPA, Garching, D-85741, Germany*

[2] *Sternberg Astronomical Institute, Universitetskiĭ pr. 13, Moscow, 119992 Russia*

Received January 26, 2005

Abstract—We compare the radial distributions of known localized gamma-ray bursts (GRBs) relative to the centers of their host galaxies with the distributions of known objects in nearby galaxies (supernovae of various types, X-ray binaries), the hypothetical dark-matter profiles, and the distribution of luminous matter in galaxies in the model of an exponential disk. By comparing the moments of empirical distributions, we show that the radial distribution of GRBs in galaxies differs significantly from that of other sources. We suggest a new statistical method for comparing empirical samples that is based on estimating the number of objects within a given radius. The exponential disk profile was found to be in best agreement with the radial distribution of GRBs. The distribution of GRBs relative to the centers of their host galaxies also agrees with the dark matter profile at certain model parameters. © *2005 Pleiades Publishing, Inc.*

Key words: *gamma-ray bursts, supernovae, dark matter.*

INTRODUCTION

At present, gamma-ray bursts (GRBs) and their afterglows are intensively studied over the entire electromagnetic spectrum (from gamma rays to radio waves) by all available astronomical methods. Detailed studies of the spectra and light curves provide insights into what properties the gamma-ray generator must have and give an idea of what physical conditions of the medium must be near a GRB. The rich phenomenology of GRBs and their possible astrophysical models have been discussed in many reviews (see, e.g., Postnov 1999; Blinnikov 2000; Zhang and Meszaros 2004). That the afterglows of GRBs are associated with the synchrotron radiation of the ultrarelativistic shock waves produced by them in the interstellar medium surrounding the GRB source may be considered to have been established (see the review by Piran (2004) and references therein).

The situation with the GRBs proper is not so good. The belief that GRBs could be directly associated with the explosions of supernovae of a special type, an energetic subclass of collapsing Type-Ibc supernovae with kinetic explosion energies above 10^{51} erg (the so-called hypernovae), has been strengthened in recent years. The association of GRBs with supernovae has received strong observational confirmation after GRB 030329, when spectral features typical of Type-Ibc supernovae were detected in the spectra of its optical afterglow (Hjorth *et al.* 2003; Stanek *et al.* 2003; Matheson *et al.* 2003). However, a recent analysis of the latest observations of GRBs and their accompanying supernovae (Postnov 2004) leads us to conclude that only relatively weak GRBs (like GRB 980425 and GRB 031203) could be associated with bright supernovae. Thus, at present, we cannot unequivocally associate each GRB with the collapse of a massive star accompanied by a hypernova explosion and reject other GRB formation hypotheses, including those outside the scope of the standard model of modern physics. Note, in particular, the interesting possibility of the association of GRBs with the poorly studied dark matter in galaxies (Gurevich *et al.* 1997; Blinnikov 2000).

Thus, the association of GRBs with known astrophysical objects in galaxies (in particular, with Type-Ibc supernovae) should be verified by independent methods. The presence of objects that are spatially distributed in galaxies in the same way as GRBs could be evidence for their relationship. This is the main motivation for our study.

A comparison of the locations of GRBs in galaxies with known populations of astrophysical sources is not new. Previously, this problem was tackled by Tsvetkov *et al.* (2001) and Bloom *et al.* (2002). Tsvetkov *et al.* (2001) showed that the surface-density distribution of the then known GRBs in

* E-mail: lisett@xray.sai.msu.ru

galaxies is similar to the surface brightness distribution of spiral galaxies (the Kolmogorov–Smirnov test yields a probability of $P_{KS} = 68\%$). The distribution of GRBs is similar to the surface brightness distribution of elliptical galaxies with a lower probability ($P_{KS} = 40\%$). The authors found no statistically significant correlation between the distributions of GRBs and OB associations ($P_{KS} = 4\%$) as well as between GRBs and Type-Ib and Ic supernovae ($P_{KS} = 9\%$).

Bloom *et al.* (2002) collected detailed statistics on the angular distances of GRB sources from the centers of their host galaxies and took into account the errors in the GRB localization and in the estimation of the galaxy radii. They compared the spatial distribution of GRBs with the distribution of merging binary neutron stars and black holes (which was theoretically derived by the population-synthesis method). The Kolmogorov–Smirnov probability was $P_{KS} \lesssim 2 \times 10^{-3}\%$ in the latter case and $P_{KS} = 45\%$ when comparing the distributions of GRBs and regions of massive star formation (in the model of a galactic disk with an exponential surface brightness distribution). This result is commonly cited as an indirect confirmation of the collapsar hypothesis, according to which GRBs originate from the evolution of massive stars (Woosley 1993).

In this paper, we analyze more complete data on the localization of GRBs in their host galaxies (mid-2004) and compare their distribution with the radial distributions of Type-Ibc and Ia supernovae and (high-mass and low-mass) X-ray binaries in nearby galaxies as well as with the hypothetical dark matter profiles. The Kolmogorov–Smirnov method, which is commonly used to compare the various empirical distributions, is inapplicable due to the occasionally significant localization errors of GRBs in galaxies. Therefore, in contrast to previous studies, we use a method for comparing the moments of the derived distributions by taking into account the localization errors of the sources. We also suggest a new method for comparing the fractions of sources within the optical radius of the galaxy.

All of the methods used yield the following main result: the statistically radial distribution of GRBs in galaxies does not coincide with that for any class of (thermonuclear and collapsing) supernovae and X-ray binaries. We also show that the radial distribution of GRBs in distant galaxies is similar to the distribution of luminous matter in the model of an exponential disk (which confirms the results by Tsvetkov *et al.* (2001) and Bloom *et al.* (2002)) and resembles the dark matter profile with the parameters that correspond to the optical radius of the GRB host galaxies.

In this paper, we present the observational data and briefly describe the methods for comparing the statistics and their application to specific samples: GRBs, Type-Ibc and Ia supernovae, X-ray binaries, and dark matter. Subsequently, we discuss the results obtained and give our conclusions.

OBSERVATIONAL DATA

We analyzed the following groups of objects: GRBs, Type-Ia and Ibc supernovae, (high-mass and low-mass) X-ray binaries, and the hypothetical dark matter distributions in galaxies. Each group (except dark matter) is a set of data on the galactocentric distances of the objects. All distances were normalized to the characteristic radius of the host galaxy. In general, this is either the optical radius of the galaxy r_{opt} (within which 50% of the galaxy's B-band luminosity is contained), or the radius calculated from the 25-mag. R band isophote, or the mean of these two values (for the GRB hosts, the latter two values can differ by several factors). For the GRBs, we additionally took into account their localization errors recalculated in units of the host radii.

GRBs. Data on the GRBs localized before 2002 were taken from Bloom *et al.* (2002). The locations of the GRBs in their host galaxies localized after 2002 were determined from original reports (see Table 1).

The degree of reliability of the GRB association with its host galaxy was discussed in detail by Bloom *et al.* (2002). In general, it is assumed everywhere that the galaxy closest to (within 1 arcsec of) the GRB is the host and that the misidenification probability is negligible. The (approximate) geometrical center, which is defined as the image centroid (Bloom *et al.* 2002) or half the maximum size of the galaxy image, is taken as the center of the observed host galaxy. The galaxy radius is calculated at half light or from the empirical magnitude–radius relation

$$r_{\text{half light}} = 0''.6 \times 10^{-0.075(m-21)},$$

where $m = R_{host}$ is the R magnitude of the host galaxy (Odewhan *et al.* 1996; Bloom *et al.* 2002). The accuracy of the characteristic sizes of the galaxy is estimated to be ~30%. To take into account the projection effect of the galaxies onto the plane of the sky, the distances in Table 1 were multiplied by a projection factor of 1.15 (since the distances decrease, on average, by ≈13% when the spatial distribution of the sources is projected onto the plane of the sky; Bloom *et al.* 2002).

Supernovae. The radial distributions of various types of supernovae in galaxies were analyzed by Bartunov *et al.* (1992, 1994). To construct the radial distribution of supernovae, we used an updatable database of the Sternberg Astronomical Institute catalog of supernovae (http://virtual.sai.msu.ru/

~pavlyuk/distrib/radial.html). The centers of the host galaxies for supernovae are determined with an error of about 10% (Tsvetkov and Pavlyuk 2004).

X-ray binaries. We used data from Grimm *et al.* (2002) to construct the radial distribution of Galactic (high-mass and low-mass) X-ray binaries.

Dark matter. Since there is no generally recognized law for the dark matter density in galaxies at present, we used two model distributions. The Burkert (B) model (Burkert 1995; Gentile *et al.* 2004) without a central density peak explains satisfactorily the observed rotation curves of nearby galaxies. The spatial density distribution of dark matter in this model is described by the formula

$$\rho_{\rm B}(r) \propto \frac{1}{(r/r_{\rm core}+1)[(r/r_{\rm core})^2+1]}, \qquad (1)$$

where the scale parameter $r_{\rm core} \simeq 15$ kpc for current galaxies (see, e.g., Gentile *et al.* 2004).

In addition, we considered the Navarro–Frenk–White (NFW) theoretical model (Navarro *et al.* 1997; Wechsler *et al.* 2002; Gentile *et al.* 2004) with a central density peak, in which the density distribution of dark matter obeys the law

$$\rho_{\rm NFW}(r) \propto \frac{1}{(r/r_{\rm s})(1+r/r_{\rm s})^2}. \qquad (2)$$

Observational data for nearby galaxies yield $r_{\rm s} \simeq 30$ kpc (Gentile *et al.* 2004).

To properly compare the radial distributions of objects in spiral galaxies with the dark matter profile, we assumed that the observed GRBs (if they are associated with dark matter) isolate a disklike region in a spherically symmetric cloud of dark matter, since the presence of a dense interstellar gas is a necessary condition for bright optical afterglows of GRBs. The characteristic galactic disk thickness is less than one kiloparsec, and the dark matter density changes only slightly across the disk on such scales (see Stoehr *et al.* 2003; Hayashi *et al.* 2004). Therefore, the dark matter surface density $\Sigma_{\rm DM}(r)$ has the same radial dependence as the volume density: $\Sigma_{\rm DM}(r) \propto \rho_{\rm DM}(r)$. Since the surface density should be multiplied by r to be compared with the one-dimensional density of the radial distribution of objects $f(r)$ derived from observations, we used the relation $f(r)[{\rm DM}] = r\rho_{\rm DM}(r)$ to analyze the dark matter.

The parameter $r_{\rm core}$ for the Burkert model is related to the optical radius of the galaxy by an empirical relation obtained by Donato *et al.* (2004):

$$\log(r_{\rm core}) = (1.05 \pm 0.11)\log r_{\rm d} + (0.33 \pm 0.04), \qquad (3)$$

where $r_{\rm d} = 0.59 r_{\rm opt}$ is a parameter in the model of an exponential galactic disk (since Donato *et al.* (2004) used a different definition for $r_{\rm opt}$, the relationship to $r_{\rm d}$ is different). The parameter of the NFW model was taken to be $r_{\rm s} = 2r_{\rm core}$. Note that Stoehr *et al.* (2003) and Hayashi *et al.* (2004) provided evidence for the presence of a plateau in the spatial density distribution up to distances of 1 kpc in the NFW model, so the Burkert dark matter distribution may be considered as a fit to the NFW distribution without a central peak.

Table 1. New data on the localization of GRBs relative to the centers of their associated host galaxies

GRB	z	r_0	σ_r	References
000131	4.5	1.09	0.30	[1]
000210	0.846	1.50	0.99	[2]
000911	1.058	0.23	0.95	[3]
000926	2.038	0.13	0.01	[4]
010222	1.477	0.77	0.92	[5]
010921	0.45	1.28	0.44	[6]
011121	0.36	0.86	0.12	[7]
011211	2.14	1.15	0.38	[8]
020405	0.69	2.21	0.62	[9]
021004	2.3	0.00	0.94	[10]
021211	1.01	2.32	1.07	[11]
031203	0.1055	0.03	0.015	[12]
040701X	0.2146	0.00	0.86	[13]
040924	0.859	0.00	1.5	[14]
041006	0.0716	0.33	0.13	[15]

Note: z is the redshift of the galaxy, r_0 is the estimated distance between the centers of the GRB error region and the host galaxy (in units of the optical radius of this galaxy), and σ_r is the radius of the GRB error region. The data sources are: [1] Bloom *et al.* (GCN notice #1133); [2] Piro *et al.* (2002); [3] Price *et al.* (2002); [4] Castro *et al.* (2001); [5] Frail *et al.* (2001); [6] J.S. Bloom *et al.* (GCN notice #1135); [7] J.S. Bloom (GCN notice #1260); [8] D.W. Fox *et al.* (GCN notice #1311); [9] N. Masetti *et al.* (GCN notice #1375); [10] A. Fruchter *et al.* http://www-int.stsci.edu/~fruchter/GRB/021004/; [11] A. Levan *et al.* (GCN notice #1758); [12] A. Gal-Yam *et al.* (astro-ph/0403608); [13] E. Pian *et al.* (GCN notice #2638); [14] A. Henden (GCN notice #2811); [15] J.P.U. Fynbo *et al.* (GCN notice #2802).

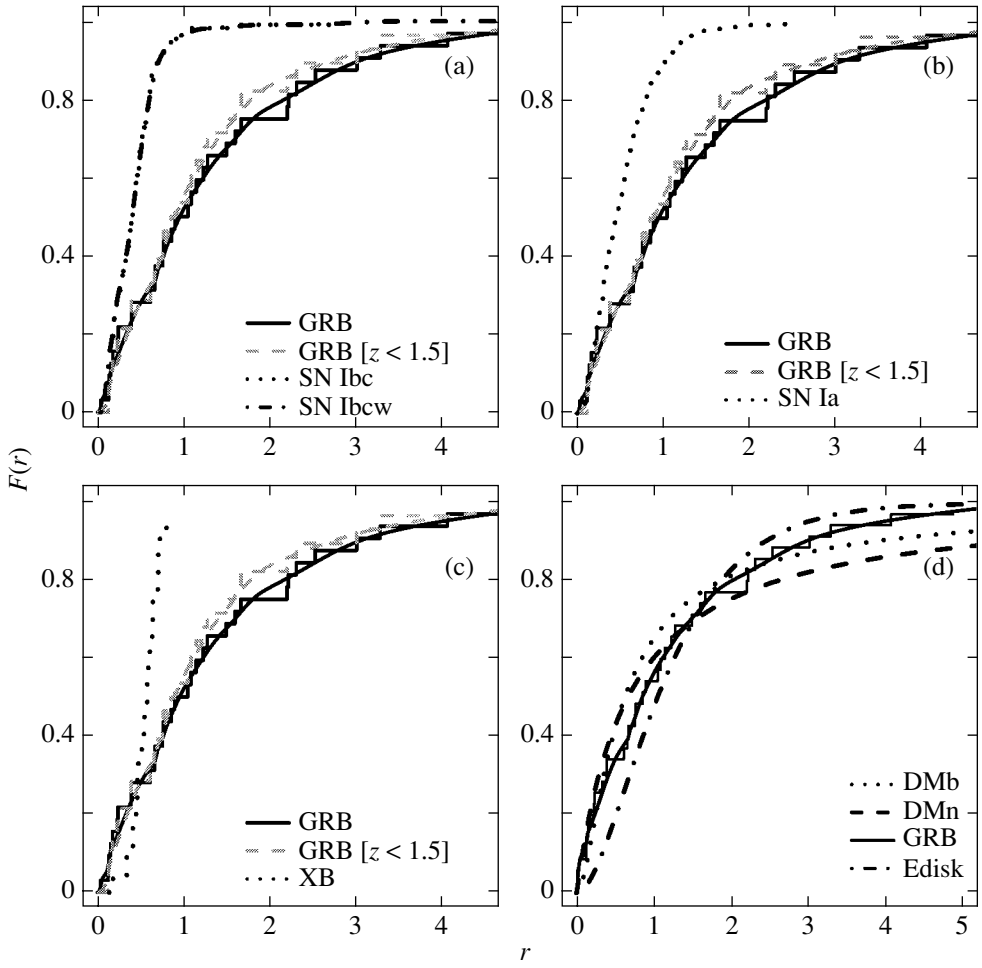

Fig. 1. Radial distributions of objects $F(r) = \int_0^r f(x)dx$, where $f(x)$ is the density of the distribution. We present data on GRBs (GRB), Type-Ibc (SN Ibc) and Ia (SN Ia) supernovae, X-ray binaries (XB), dark matter (DMb is the Burkert profile (1995), $r_{\rm core} = 0.83 r_{\rm opt}$; DMn is the NFW profile (Navarro *et al.* 1997), $r_{\rm s} = 1.67\, r_{\rm opt}$ and the exponential disk (Edisk). The step distributions were constructed for the GRBs without smoothing. The smooth curves represent the smoothed (with localization errors) cumulative distributions of GRBs (GRBw), supernovae (SN Ibcw), and GRBs at $z < 1.5$ (GRB [$z < 1.5$]).

We also used the surface-density profile of luminous matter in galaxies in the model of an exponential disk:

$$\Sigma_{\rm exp}(r) \propto \exp(-r/r_{\rm d}), \qquad (4)$$

for which the radial distribution is

$$f(r)[\exp] = r\exp(-r/r_{\rm d}). \qquad (5)$$

Radial Distributions of the Objects under Study

We begin by constructing the radial distributions of the objects under study. We use the dimensionless galactocentric distances (i.e., each galactocentric distance was normalized to the optical radius of the corresponding host galaxy). On average, $\langle r_{\rm opt}\rangle \simeq 2.5$ kpc for the distant galaxies in which GRBs were observed (Bloom *et al.* 2002) and $\langle r_{\rm opt}\rangle \simeq 15$ kpc for the nearby galaxies in which the supernovae under study are located. The radial distribution of the measured GRBs (without localization errors) as a function of the galactocentric distance is indicated in Fig. 1 by the step line for all the GRBs under consideration (black line) and GRBs with redshifts less than 1.5 (gray line).

Due to the GRB localization errors, the probability density of finding the source at a given radius, $p(r)$, should be taken in place of the galactocentric distance r. The probability density $f(r)$ for N sources can be calculated by adding the individual probability densities: $f(r) = \sum_{i=1}^{N} p_i(r)$. The localization errors are taken into account as follows. If r_0 is the measured galactocentric distance of the center of the error region for an individual GRB and σ_r is the error in the GRB location (i.e., the error region is assumed to be

Table 2. Central moments of the radial distributions of GRBs, supernovae, and X-ray binaries calculated without localization errors

$\mu^i(r), i = 1, 2$	$\mu^1(r) \pm \sigma_{\mu^1(r)}$	$\mu^2(r) \pm \sigma_{\mu^2(r)}$	$r^{\rm med} \pm \sigma_{r^{\rm med}}$
GRBs	1.18 ± 0.21	1.45 ± 0.42	0.82 ± 0.20
Nearby GRBs, $z < 1.5$	1.00 ± 0.17	1.03 ± 0.33	0.76 ± 0.18
Type-Ibc supernovae (SN Ibc)	0.43 ± 0.03	0.12 ± 0.06	0.40 ± 0.03
Type-Ia supernovae (SN Ia)	0.54 ± 0.02	0.14 ± 0.02	0.47 ± 0.03
X-ray binaries (LMXB and HMXB)	0.54 ± 0.03	0.029 ± 0.01	0.58 ± 0.04

Note: $\mu^1(r)$ is the mean, $\mu^2(r)$ is the variance, and $r^{\rm med}$ is the median. The rms deviations were calculated by the bootstrap method.

circular in shape, which is not always the case), then the probability density of finding the source at distance r from the center of the host galaxy is described by the Rice distribution (Bloom *et al.* 2002)

$$p(r; r_0, \sigma_r)dr = \frac{r}{\sigma_r^2}\, e^{-\frac{r^2+r_0^2}{2\,\sigma_r^2}} I_0\left(\frac{r\, r_0}{\sigma_r^2}\right) dr, \qquad (6)$$

where I_0 is a modified Bessel function of the zeroth order. In the case of a small localization error, the probability distribution of the source's location is close to the $\delta(r - r_0)$-function. A large localization error leads to a probability density with broad wings. Thus, more accurate data are more significant, and the weight (significance) of each observation is taken into account.

In analyzing the radial distributions of supernovae, the error with which the center of the galaxy image is determined rather than the localization error of the supernova itself makes a major contribution to the error in their galactocentric distances. Since analysis indicates (Tsvetkov and Pavlyuk 2004) that this error does not exceed 10% of the optical radius, we took $\sigma_r = 0.1r$ for supernovae.

The profiles of the GRB distribution function $F(r) = \int\limits_0^r f(x)dx$ are represented in Fig. 1 by the smooth curves. For comparison, this figure also shows the smoothed radial distributions of supernovae (Figs. 1a and 1b) and X-ray binaries (Fig. 1c). In addition to the distributions of GRBs with and without localization errors, Fig. 1d shows the theoretical dark matter profiles $F(r)[\mathrm{DM}] = \int\limits_0^r \rho_{\rm DM}(x)xdx$ in models (1) and (2) for the parameters calculated using relation (3), $r_{\rm core} = 0.83\, r_{\rm opt}$ and $r_{\rm s} = 1.67\, r_{\rm opt}$, respectively. This figure also shows the radial distribution of galactic luminous matter in the model of an exponential disk (4) for $r_{\rm d} = 0.59 r_{\rm opt}$, $F(r)[\exp] = \int_0^r \rho_{\exp}(x)xdx$.

THE METHODS FOR COMPARING THE POPULATIONS OF OBJECTS

We used the following methods to compare the empirical distributions of the objects under study in galaxies: (1) estimating the moments of the empirical distributions and (2) counting the number of objects within a given radius. These methods were applied to the observed distributions of objects in galaxies with and without localization errors.

Let us consider these methods successively.

Estimates of the Distribution Moments

The moments of the probability distribution functions are important in various astrophysical problems (see, e.g., the review by Blinnikov and Moessner 1998). Let us consider the estimates for the first two moments (mean and variance) of the distributions of the objects under study. The mean relative galactocentric distances (the first moment) in the distributions of various objects provide information about the characteristic localization (centroid) of the population under study. The variance (the second central moment) is indicative of the degree of scatter about the mean.

The mean (the first moment) and variance (the second central moment) of the empirical distributions were estimated using standard formulas (see, e.g., G. Korn and T. Korn 1968):

$$\mu^1(r) \equiv \langle r \rangle \simeq \frac{1}{N}\sum_{i=1}^{N} r_i, \qquad (7)$$

$$\mu^2(r) \simeq \frac{1}{N-1}\sum_{i=1}^{N} (r_i - \langle r \rangle)^2.$$

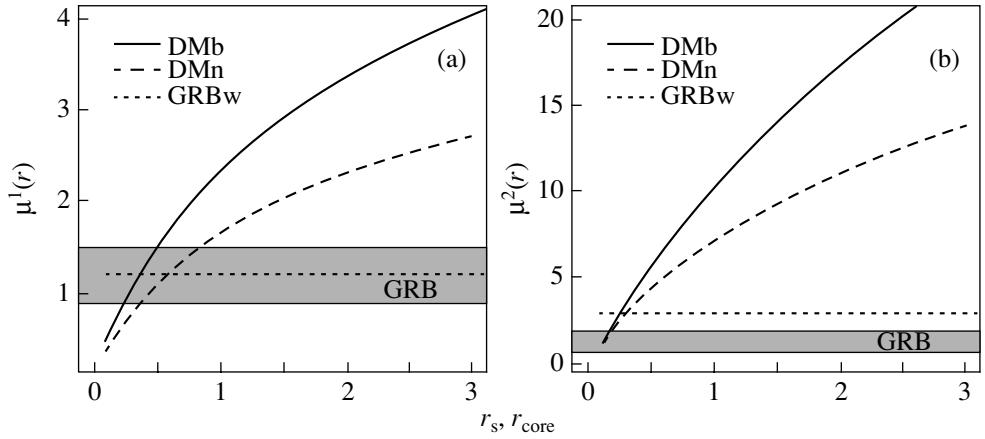

Fig. 2. First (a) and second (b) moments of the dark matter distribution versus Burkert and NFW model parameters.

Since the estimate of the mean for small samples with outliers can be strongly biased, in addition to the first two moments, the medians are considered. The median can be estimated from the condition $F(r_{\rm med}) \simeq 1/2$ (F is the empirical distribution function of the random variable r); i.e., a value of r above and below which there is half of all data is found.

We estimated the errors in the moments of the empirical distributions using the bootstrap method (Éfron 1988; see the Appendix). Table 2 gives our estimates for the first two moments of the distributions and the medians with the rms deviations estimated by the bootstrap method for gamma-ray bursts (GRB), Type-Ibc supernovae (SN Ibc), Type-Ia supernovae (SN Ia), and X-ray binaries (XB). We emphasize that the localization errors of the sources themselves are ignored in this analysis.

Including the localization errors of the sources allows us to directly consider the probability densities $f(r)$ rather than the distribution functions $F(r)$. If the probability density is known, the moments of the distributions can be calculated using the formulas

$$\bar{\mu}^i(r) = \frac{\int\limits_0^\infty x^i f(x)dx}{\int\limits_0^\infty f(x)dx}. \qquad (8)$$

Table 3 gives the calculated moments of the distributions, $\bar{\mu}^1$ and $\bar{\mu}^2$, for GRBs with localization errors (GRBw) and Type-Ibc supernovae with localization errors (SN Ibcw). In Fig. 2, the first and second moments are plotted against the parameters $r_{\rm s}$ and $r_{\rm core}$ for the dark-matter models under consideration. The first moments for GRBs taken from Tables 2 and 3 are shown for comparison. We emphasize that, in contrast to the moments calculated using formulas (7), moments (8) are not central, but ordinary; therefore, only the first moments can be compared; the second moments μ^2 and $\bar{\mu}^2$ cannot be compared.

Table 3. Moments of the observed radial distributions $f(r)$ of GRBs and Type-Ibc supernovae with localization errors, moments of the theoretical radial dark matter distributions for the two models, and moments of the radial luminous-matter distribution in the exponential disk model

$\mu^i(r), i = 1, 2$	$\bar{\mu}^1(r)$	$\bar{\mu}^2(r)$
Gamma-ray bursts (GRBw)	1.22	2.94
Nearby gamma-ray bursts, $z < 1.5$ (GRBw)	1.07	2.35
Type-Ibc supernovae (SN Ibcw)	0.43	0.30
Dark matter		
Burkert (DMb: $r_{\rm core} = 0.83 r_{\rm opt}$)	2.11	8.61
NFW (DMn: $r_{\rm s} = 1.67 r_{\rm opt}$)	2.13	9.70
Exponential disk ($r_{\rm d} = 0.59 r_{\rm opt}$)	1.18	2.09

Counting the Objects within $r_{\rm opt}$

Consider another quantitative comparison test for empirical samples, which allows the localization errors of the sources to be taken into account.

Let us calculate the number of objects within $r_{\rm opt}$ of the galaxy for each sample. To take into account the localization errors, we proceed as follows. We specify the brightness profile of the galaxy in the form of the function

$$K(x) \simeq \begin{cases} 1, r < r_{\rm opt} \\ 0, r > r_{\rm opt}. \end{cases} \qquad (9)$$

The approximate equality implies that we assume the error in the radius to be 30% and fit the edges

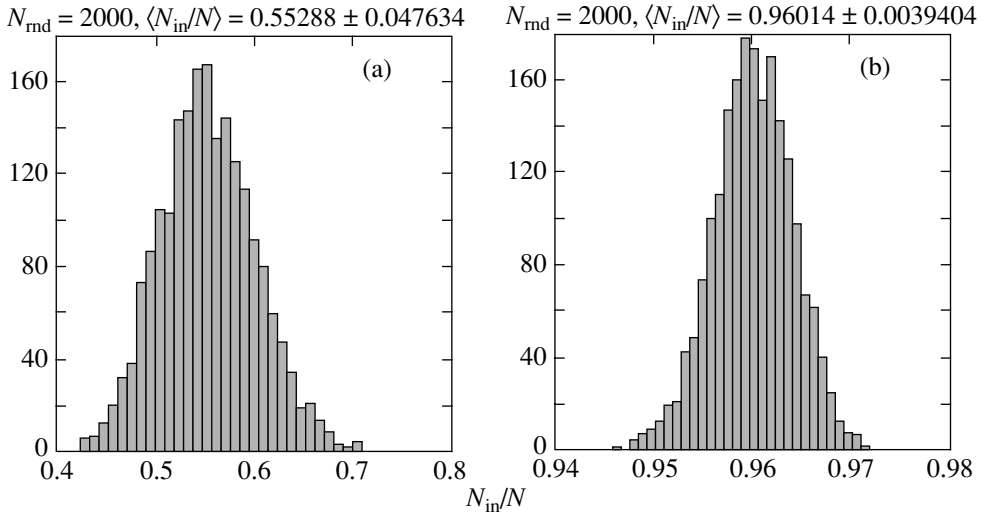

Fig. 3. Histograms of N_{in}/N obtained through numerical simulations for (a) GRBs and (b) Type-Ibc supernovae.

of the galaxy by a smooth monotonic function. For definiteness, the wings of the galaxy are assumed to be described by a normal (cumulative) distribution function with a dispersion of $\sigma = 0.3$.

Let the location of the object relative to the galactic center r_i and its (presumably normal) error σ_i be known. To count the fraction of objects within r_{opt}, we can use the random variable

$$\frac{N_{in}}{N} = \frac{1}{N}\sum_{i=1}^{N}\int_{-\infty}^{\infty} f^i(x)K(x)dx, \qquad (10)$$

where $f^i(x) \equiv f(x, r_i, \sigma_i)$ is the probability density of the normal distribution with mean r_i and dispersion σ_i (x varies within the range $-\infty$ to ∞).

Let us find the distribution of the random variable N_{in}/N. For this purpose, we draw a new random variable x for each source r_i in accordance with the initial distribution function $f^i(x)$ with known mean and dispersion. We repeat the procedure n times for each value of r_i. The estimate of the number of objects within r_{opt} is then

$$\left(\frac{N_{in}}{N}\right)_k \simeq \frac{1}{N}\sum_{i=1}^{N} K(x_{i,k}), \quad k = 1, n. \qquad (11)$$

In the limit of a large number of trials, a normally distribution random variable $(N_{in}/N)_k$ must be obtained, and its rms error can be estimated. The result of our numerical simulations for 2000 trials is given in Table 4 (column 2). Figure 3 shows the histograms of N_{in}/N for GRBs (Fig. 3a) and Type-Ibc supernovae (Fig. 3b) derived from numerical simulations.

For sources with a given radial distribution function (e.g., for dark matter and an exponential distribution of luminous matter in galactic disks), N_{in}/N can be estimated using the formula

$$\frac{N_{in}}{N} \simeq \frac{\sum\limits_{i=1}^{\infty} K(x_i)f(x_i)}{\sum\limits_{i=1}^{\infty} f(x_i)}, \qquad (12)$$

where f is specified by relations (1), (2), and (5). The values of N_{in}/N are given in Table 5; N_{in}/N is plotted against r_s and r_{core} for dark matter in Fig. 4.

For discrete empirical samples, there is a different method for counting the number of objects within a given radius. Let us define the random variable

$$y_i = \begin{cases} 1, & |r_i| \le 1 \\ 0, & |r_i| > 1, \end{cases} \qquad (13)$$

which has a discrete probability distribution. The probability of an object being within the optical radius of the host galaxy ($y_i = 1$) is

$$p_i = \int_{-1}^{1} f^i(x)dx, \qquad (14)$$

while the probability $P(y_i = 0) = (1 - p_i)$ for the ith object under study. The estimates of the mean and variance of y_i (see G. Korn and T. Korn 1968) are

$$\mu^1(y_i) = p_i, \quad \mu^2(y_i) = p_i(1 - p_i). \qquad (15)$$

The sum of the means y_i for all objects of a given class

Table 4. Fractions of the sources within the galaxy radius, $N_{\rm in}/N$, for various types of objects

Tested sample	$N_{\rm in}/N$	$[N_{\rm in}/N]$
Gamma-ray bursts (GRB)	0.553 ± 0.048	0.5602 ± 0.054
Type-Ibc supernovae (SN Ibc)	0.960 ± 0.004	0.966 ± 0.007

Note: The second and third columns give the results of our numerical simulations for 2000 trials using formulas (11) and (16), respectively.

yields an estimate of $[N_{\rm in}/N]$ and its dispersion:

$$[N_{\rm in}/N] = \sum_{i=1}^{N} \mu^1(y_i)/N,$$
$$\sigma_{[N_{\rm in}/N]} = \sqrt{\sum_{i=1}^{N} \mu^2(y_i)/N}. \qquad (16)$$

The values of $[N_{\rm in}/N]$ and $\sigma_{[N_{\rm in}/N]}$ for GRBs and Type-Ibc supernovae calculated by this method are listed in the third column of Table 4; these are in close agreement with the values obtained by our numerical simulations using the first method.

DISCUSSION

Analyzing the moments of the empirical distributions of the objects under study (Tables 2 and 3) and counting the number of sources within the optical radius of the galaxy (Tables 4 and 5) led us to conclude that the radial distribution of GRBs in galaxies differs significantly from the distributions of supernovae of various types and X-ray binaries. GRBs are, on average, farther from the galactic centers and are distributed more widely than other objects. This conclusion is in conflict with the hypothesis that all GRBs are associated with the corresponding supernovae, but it is consistent with the assumption that only nearby GRBs with relatively small energy release are associated with bright hypernovae, while more energetic GRBs seen at high redshifts are not accompanied by bright supernovae.

Table 5. Fractions of the sources within the galaxy radius, $N_{\rm in}/N$, for the theoretical dark-matter and luminous-matter profiles in the exponential disk model calculated using formula (12)

Tested distributions	$N_{\rm in}/N$
Burkert dark matter (DMb: $r_{\rm core} = 0.83 r_{\rm opt}$)	0.38
NFW dark matter (DMn: $r_{\rm s} = 1.67 r_{\rm opt}$)	0.425
Exponential disk ($r_{\rm d} = 0.59 r_{\rm opt}$)	0.50

All GRBs are distant objects, and the typical redshift of the galaxies under consideration is $\sim$1; at such large distances, the morphology of the galaxies may differ from their current morphology. The typical optical radii of the GRB host galaxies and the galaxies in the closest neighborhood are $\sim$2–3 and 10–15 kpc, respectively. Such a large difference in the radii cannot be explained in terms of cosmological effects, which cause an effective decrease in the optical radius by only a few percent. Spectroscopic observations of the host galaxies of GRBs (Sokolov *et al.* 2001) lead one to conclude that these are galaxies with an enhanced star formation rate and significant internal extinction, although, in general, the properties of these galaxies (Hurley *et al.* 2003) correspond to those of late-type field galaxies at the corresponding redshifts. A small optical radius could be indicative of the actual small size (compact galaxies) or the existence of a significant part of the gaseous galactic disk unaffected by star formation (Begum *et al.* 2005).

If we associate GRBs with the evolution of massive stars, then the assumption about a nonstandard pattern of star formation in the GRB host galaxies, which causes the initial mass function of young stars to change in favor of a larger number of very massive stars, could be a possible way out of the disagreement between our radial distributions of Type-Ibc supernovae and GRBs in galaxies. This could explain why GRBs are associated mostly with late-type galaxies, because the (secondary) star formation in such galaxies proceeds under conditions of slow differential rotation. A detailed determination of the chemical composition of the gas in GRB host galaxies can serve as a test of this hypothesis.

Since no data are available for high-redshift Type-Ibc supernovae, a comparison is made using supernovae in nearby galaxies. We could attempt to attribute the difference between the derived radial distributions of GRBs and supernovae in galaxies to different radial distributions of massive stars in galaxies at high redshifts. However, this explanation is in conflict with the satisfactory description of the GRB distribution by the model of luminous matter with an exponential surface density.

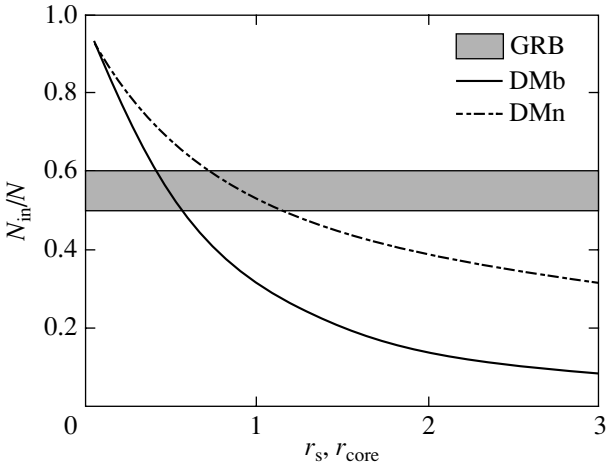

Fig. 4. N_{in}/N versus r_s and r_{core} for the dark matter models.

A comparison of Tables 4 and 5 shows that the observed fraction of GRBs within the optical radius differs only slightly from the fraction of dark matter in the disk. One would think that the behavior of the second moment for dark matter (see, in particular, Fig. 2) rejects the association of GRBs with dark matter. However, it should be kept in mind that the second (noncentral!) moment increases sharply the weight of the distant galactic regions. We calculated this moment directly for the dark matter density; of course, the GRB localization observations were selected by the presence of an ordinary gas, which also has a quasi-exponential radial distribution in the galaxy. Including this truncation changes only slightly the numbers in Tables 4 and 5 and the first moment, but reduces greatly the second moment for dark matter.

CONCLUSIONS

Our analysis shows that the distribution of luminous matter in galaxies in the model of an exponential disk with the parameter $r_d = 0.59r_{opt}$ is in best agreement with the spatial distribution of GRBs in their host galaxies. This is confirmed by previous studies (Tsvetkov *et al.* 2001; Bloom *et al.* 2002). However, this result cannot be unequivocally interpreted as evidence that GRBs originate from young massive stars, since the disk brightness follows the distribution of all (including low-mass) population-I stars and gas.

It can also be asserted that the radial distribution of GRBs agrees with the distributions of dark matter in galaxies at quite realistic parameters r_s and r_{core} under the assumption that the decrease in the scale parameter of the spatial dark matter distribution is proportional to the optical radius of the GRB host galaxies.

ACKNOWLEDGMENTS

This work was supported in part by the Russian Foundation for Basic Research (project nos. 05-02-17480 and 03-02-16110). We wish to thank O.K. Sil'chenko and A.V. Zasov for helpful discussions.

APPENDIX

The Bootstrap Method

The main idea behind the method is to approximate the unknown distribution function of a random variable by an empirical distribution. This approximate distribution function is used to estimate the moments of the random variable (mean and variance).

In accordance with this empirical distribution, various realizations (samples) of the random variable are modeled by the Monte Carlo method. Obtaining a sample each time, we determine the moment (mean and dispersion) of the distribution of interest. Modeling the sample of the random variable many times, we obtain the mean value of the moment and its distribution function. According to the central limit theorem, the derived distribution function of the parameters approaches a normal law. Thus, the confidence intervals for the moments of the empirical distribution can be estimated.

REFERENCES

1. O. S. Bartunov, I. N. Makarova, and D. Yu. Tsvetkov, Astron. Astrophys. **264**, 428 (1992).
2. O. S. Bartunov, D. Yu. Tsvetkov, and I. V. Filimonova, Publ. Astron. Soc. Pac. **264**, 1276 (1994).
3. A. Begum, J. N. Chendalur, and I. D. Karachentsev, Astron. Astrophys. (2005, in press); astro-ph/0502307.
4. S. I. Blinnikov, Surv. High Energy Phys. **15**, 37 (2000).
5. S. Blinnikov and R. Moessner, Astron. Astrophys., Suppl. Ser. **130**, 193 (1998).
6. J. S. Bloom, S. R. Kulkarni, and S. G. Djorgovski, Astron. J. **123**, 1111 (2002).
7. A. Burkert, Astrophys. J. **447**, L25 (1995).
8. S. Castro, T. J. Galama, F. A. Harrison, *et al.*, astro-ph/0110566 (2001).
9. F. Donato, G. Gentile, and P. Salucci, Mon. Not. R. Astron. Soc. **353**, L17 (2004).
10. B. Éfron, *Non-traditional Methods of Multivariate Statistical Analysis* (Finansy i Statistika, Moscow, 1988) [in Russian].
11. D. A. Frail, F. Bertoldi, G. H. Moriarty-Schieven, *et al.*, astro-ph/0108436 (2001).
12. G. Gentile, P. Salucci, U. Klein, *et al.*, Mon. Not. R. Astron. Soc. **351**, 903 (2004).
13. H.-J. Grimm, M. Gilfanov, and R. Sunyaev, Astron. Astrophys. **391**, 923 (2002).

14. A. V. Gurevich, K. P. Zybin, and V. A. Sirota, Usp. Fiz. Nauk **167**, 913 (1997) [Phys. Usp. **40**, 869 (1997)].
15. E. Hayashi, J. F. Navarro, C. Power, *et al.*, Mon. Not. R. Astron. Soc. **355**, 794 (2004).
16. J. Hjorth, J. Sollerman, P. Meller, *et al.*, Nature **423**, 847 (2003).
17. K. Hurley, R. Sari, and S. G. Djorgovki, *Compact Stellar X-ray Sources*, Ed. by W. Lewin and M. van der Klis (Cambridge Univ. Press, Cambridge, 2003); astro-ph/0211620.
18. G. A. Korn and T. M. Korn, *Mathematical Handbook for Scientists and Engineers* (McGraw-Hill, New York, 1968; Nauka, Moscow, 1984).
19. T. Matheson, P. M. Garnavich, K. Z. Stanek, *et al.*, Astrophys. J. **599**, 394 (2003).
20. J. F. Navarro, C. S. Frenk, and S. D. M. White, Astrophys. J. **490**, 493 (1997).
21. S. C. Odewhan, R. A. Windhorst, S. P. Driver, and W. C. Kee, Astrophys. J. **472**, L13 (1996).
22. T. Piran, astro-ph/0405503 (2004).
23. L. Piro, D. A. Frail, J. Gorosabel, *et al.*, Astrophys. J. **577**, 680 (2002).
24. K. A. Postnov, Usp. Fiz. Nauk **169**, 545 (1999) [Phys. Usp. **42**, 469 (1999)].
25. K. A. Postnov, in *Proceedings of the International Workshop QUARKS-2004*, Ed. by D. V. Levkov, V. A. Matveev, and V. A. Rubakov; astro-ph/0409755 (2004).
26. P. A. Price, E. Berger, S. R. Kulkarni, *et al.*, Astrophys. J. **573**, 85 (2002).
27. V. V. Sokolov, T. A. Atkhullin, A. J. Castro-Tirado, *et al.*, Astron. Astrophys. **372**, 438 (2001).
28. K. Z. Stanek, T. Matheson, P. M. Garnavich, *et al.*, Astrophys. J. **591**, L17 (2003).
29. F. Stoehr, S. D. M. White, V. Springel, *et al.*, Mon. Not. R. Astron. Soc. **345**, 1313 (2003).
30. D. Yu. Tsvetkov and N. N. Pavlyuk, private communication (2004).
31. D. Yu. Tsvetkov, S. I. Blinnikov, and N. N. Pavlyuk, Pis'ma Astron. Zh. **27**, 483 (2001) [Astron. Lett. **27**, 411 (2001)].
32. R. H. Wechsler, J. S. Bullock, J. R. Primack, *et al.*, Astrophys. J. **568**, 52 (2002).
33. S. A. Woosley, Astrophys. J. **405**, 273 (1993).
34. B. Zhang and P. Meszaros, Int. J. Mod. Phys. A **19**, 2385 (2004).

Translated by V. Astakhov

Astronomy Letters, Vol. 31, No. 6, 2005, pp. 375–379. Translated from Pis'ma v Astronomicheskiĭ Zhurnal, Vol. 31, No. 6, 2005, pp. 422–426.

The Brightest OH Maser in the Sky: A Flare of Emission in W75 N

A. V. Alakoz*, V. I. Slysh, M. V. Popov, and I. E. Val'tts

Astrospace Center, Lebedev Physical Institute, Russian Academy of Sciences, Profsoyuznaya ul. 84/32, Moscow, 117997 Russia

Received December 30, 2004

Abstract—A flare of maser radio emission in the 1665-MHz OH line with a flux density of about 1000 Jy was discovered in the star-forming region W75 N in 2003. At the time of its observations, it was the strongest OH maser in the entire history of research since the discovery of cosmic OH masers in 1965. The linear polarization of the flare emission reached 100%. A weaker flare with a flux density of 145 Jy was observed in this source in 2000–2001; this was probably a precursor of the intense flare. The intensity of two other spectral features decreased when the flare emerged. This change in the intensity of the emission from maser condensations (a brightening of some of them and a weakening of others) can be explained by the passage of a magnetohydrodynamic shock through regions of enhanced gas concentration.

Key words: *interstellar medium, OH masers, variability.*

INTRODUCTION

W75 N is an active region of star formation in the Galaxy that is accompanied by maser emission in OH, methanol, and H_2O lines. Mapping observations of masers with a high angular resolution have shown that the maser emission sources are associated with ultracompact H II regions (Hunter *et al.* 1994; Minier *et al.* 2000; Slysh *et al.* 2002) and are, possibly, located in protoplanetary disks surrounding young massive stars. In this paper, we report the discovery of an intense flare of emission as a result of which W75 N became the brightest OH cosmic maser in the entire history of observations.

OBSERVATIONS

Polarization observations of the maser emission from W75 N in all four Stokes parameters were performed with the Nançay radio telescope (France) (van Driel *et al.* 1996) in October 2003 and with the Kalyazin 64-m radio telescope (Russia) (Slysh *et al.* 2001) in July and October 2004 in two circular polarizations in the 1665- and 1667-MHz OH lines. Digital autocorrelators with a spectral resolution of 0.137 km s^{-1} were used at both telescopes to analyze the spectra. The number of channels at Nançay was 8192 divided in eight sections with 1024 channels each (both frequencies were observed simultaneously, and an individual polarization corresponded to each section); the bandwidth was 0.781 MHz. At Kalyazin, there was only one section of 4096 channels with a bandwidth of 3.125 MHz; therefore, the right- and left-hand circular polarizations were measured sequentially. In addition, several records were made on magnetic tape in the S-2 VLBI system on April 12, 2001, at the 64-m radio telescope in the Bear Lakes (Russia) and on July 22, 2004, at Kalyazin (the bandwidth in both cases was 8 MHz). A spectral analysis was performed with a software correlator (the resolution could be varied over a wide range). The sensitivity was 1.0 K Jy^{-1} for the Nançay radio telescope and 0.65 K Jy^{-1} for the Bear Lakes and Kalyazin radio telescopes. The flux density calibration for the Bear Lakes and Kalyazin radio telescopes was performed with the continuum sources Cygnus A and 3C 274. The beam width of the Nançay radio telescope was $3\farcm5$ in the east–west direction and $19'$ in the north–south direction. The Bear Lakes and Kalyazin radio telescopes had circular beams with a width of $8'$. In addition to our own observations, we also analyzed observational data for this source in OH lines from the NRAO VLBA archive for November 2000 and January 2001 (the observations by Fish and Migenes).

RESULTS

The spectra of W75 N obtained with the VLBA in 1998 (Slysh *et al.* 2002) and 2001 (the VLBA archive) as well as at Nançay in 2003 and Kalyazin in 2004 in the 1665-MHz OH line in right-hand circular polarization are shown in Fig. 1. Some differences between the VLBA spectra and the three

*E-mail: rett@asc.rssi.ru

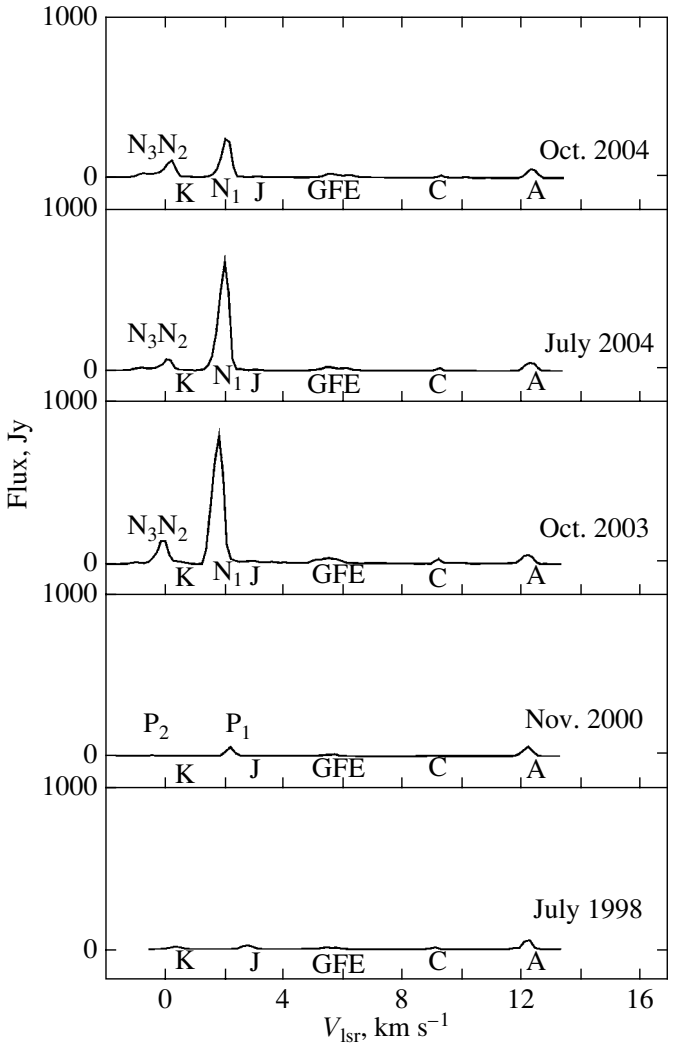

Fig. 1. Spectra for the OH maser W75 N in the 1665-MHz line (right-hand circular polarization) taken at different epochs. July 1998: VLBA array, July 1, 1998; Nov. 2000: VLBA array, November 22, 2000; Oct. 2003: Nançay radio telescope, October 24, 2003; July 2004: Kalyazin radio telescope, July 14, 2004; Oct. 2004: Kalyazin radio telescope, October 20, 2004; A–K are the spectral features identified by Slysh *et al.* (2002), and P_1, P_2 and N_1, N_2, N_3 are the new spectral features of the precursor (P) and the flare (N). The VLBA spectra are shown in interferometric mode, in which contribution from the nearby maser W75 S at a distance of 14′ is eliminated.

remaining spectra stem from the fact that these were taken in VLBI mode, while the single-dish spectra were taken in the total-power mode. We do not show the total-power spectra from individual VLBA antennae, because, unfortunately, these are distorted by the emission from the nearby maser W75 S due to a large beam. Several features, which were designated as A, C, E, F, G, J, and K in the paper by Slysh *et al.* (2002), were observed in the first 1998 spectrum obtained during the VLBA mapping. These were also present in the previous observations of 1983 (Baart *et al.* 1986) with approximately the same intensity, except features J and K at radial velocities of 3.0 and 0.65 km s^{-1} with a variable intensity. The subsequent VLBA observations in November 2000 and January 2001 (the VLBA archive) showed that the spectrum of the source remained unchanged in the range of radial velocities from 4 to 14 km s^{-1}, while significant changes occurred at lower radial velocities. A strong spectral feature at a radial velocity of 2.3 km s^{-1} with a flux density of 145 Jy and a line width of 0.35 km s^{-1} (75 Jy in the right-hand circular polarization shown in Fig. 1) and a weaker feature at a radial velocity of -0.2 km s^{-1} with a flux density of 35 Jy appeared. We designate these as P_1 and P_2, respectively. At the same time, features J and K dimmed by a factor of 2 to 3. The subsequent observations with the Bear Lakes 64-m telescope in April 2001 (the spectrum is not shown) demonstrated that the flared features P_1 and P_2 dimmed by a factor

of 2 to 5 while remaining at the same radial velocities. This flare of features P_1 and P_2 may be assumed to have been a precursor of the even brighter flare of maser emission that we first observed 2.5 years later with the Nançay radio telescope on October 24, 2003. The spectrum in Fig. 1 exhibits a very intense feature at a radial velocity of 1.8 km s^{-1} with a flux density of 750 Jy and a line width of 0.35 km s^{-1} (N_1) and two weaker features at radial velocities of 0 (N_2) and -1 km s^{-1} (N_3). The polarization measurements at Nançay show that all features of the flare (N_1, N_2, and N_3) have a high ($\geq$80%) degree of linear polarization. The difference between the radial velocities of the new features N_1 and N_2 and those of the precursor, about -0.5 km s^{-1}, and the decay of the precursor in April 2001 suggest that a flare of the new spectral features rather than a brightening of the old features was observed. At the same time, the flux densities and radial velocities of features A–G remained unchanged. Features J and K, if present, have a flux density of no more than 10 Jy. The subsequent observations performed at Kalyazin in July 2004 confirmed the existence of flared features almost at the same radial velocities and with the same flux densities. The more recent observations at Kalyazin in October–December 2004 point to a decay of the strongest spectral feature N_1 with the simultaneous growth of the weaker flare features N_2 and N_3. In the other OH line at a frequency of 1667 MHz observed at Nançay, new spectral features also appeared, but their intensity did not exceed 20 Jy and was comparable to that of the remaining spectral features.

DISCUSSION

Although the variability of OH masers is well established, no OH maser emission flares with such high flux densities have been reported previously. However, a spectral feature with a flux density of 960 Ju in left-hand circular polarization was observed in the source G351.78-0.54 in 1980 (Caswell and Haynes 1983). At present, there is no known OH maser with a flux density higher than or comparable to that of W75 N. An intense flare of maser emission has been observed twice in the 1.35-cm water-vapor line in Orion (Abraham *et al.* 1981; Matveyenko *et al.* 1981; Omodaka *et al.* 1998) with a flux density above 10 MJy. Since the flux density of water masers, on average, exceeds that of OH masers by a factor of $10–10^3$, it is not surprising that the scale of the flare is, accordingly, larger for water masers.

Slysh *et al.* (2002) suggested a model for the maser W75 N in which the maser spots are located in disks rotating around two massive stars, which, in turn, excite the ultracompact H II regions VLA 1 and VLA 2 (Torrelles *et al.* 1997) (Fig. 2). The spectral features from A to I at radial velocities from 12.45 to 3.70 km s^{-1} are associated with VLA 1 (some of the weaker features are unseen on the scale of our diagram and have no designations); only two features, J and K at radial velocities of 3.0 and 0.65 km s^{-1}, respectively, are associated with VLA 2. Judging by the radial velocities of the new spectral features of the flare at 2 and 0 km s^{-1}, these could also be associated with VLA 2. VLA 1 and VLA 2 are the separate centers of maser emission also in H_2O and, probably, methanol lines. These ultracompact H II regions are excited by young massive stars of spectral type B1 or B2 with a mass of 10 $M_\odot$ (Shepherd *et al.* 2004). The separation between the stars is $\sim$ 1400 AU. Torrelles *et al.* (1997) suggested a model for the source W75 N in which the stars are the sources of a wind and a shock that excite the maser emission. The maser system associated with VLA 2 is more compact and, apparently, more active. This is evidenced by the observations of the flare of the high-velocity masers in the 1667-MHz OH line in 1986 (Hutawarakorn *et al.* 2002) and the variability of the H_2O maser emission with a period of 11.5 yr associated with VLA 2 (Lekht and Krasnov 2000). The new flare in the 1665-MHz OH line with a flux density of 1000 Jy that is reported in this paper also occurred in the maser system associated with VLA 2. Within the framework of the model of a stellar-wind shock, we can assume that the flare began upon the arrival of the shock to a region of enhanced abundance of H_2O and hydroxyl molecules and elevation of the kinetic temperature in this region or was triggered by the enhancement of abundance of H_2O and hydroxyl molecules caused by the shock.

Almost simultaneously with the rise in the flux of the spectral features of the precursor flare at radial velocities of 2.3 and -0.2 km s^{-1}, the flux of the spectral features J and K at radial velocities of 3.0 and 0.65 km s^{-1} decreases. We see from Fig. 1 that these features are absent in the 2001 spectrum of W75 N, at least at a level of 10 Jy, while in 1998 these were comparable in flux to the brightest feature A (Slysh *et al.* 2002). Features J and K were even brighter in the past: the peak flux of feature J was observed in 1993 (Hutawarakorn *et al.* 2002), and this feature was weaker at earlier epochs, 1983 and 1986 (Baart *et al.* 1986; Hutawarakorn *et al.* 2002), as well as at later epochs (1998) (Argon *et al.* 2000; Slysh *et al.* 2002). Using this data, we can estimate the duration of the emission from feature J at a half-intensity level, $t = 11$ yr, with a peak in 1993. It is well known from the VLBA maps (Fig. 2) (Slysh *et al.* 2002) that feature J (like feature K) is extended and in the shape of a thin 10.7×2.4-mas strip with a position angle of 114°. At a distance of 2 kpc to W75 N, this

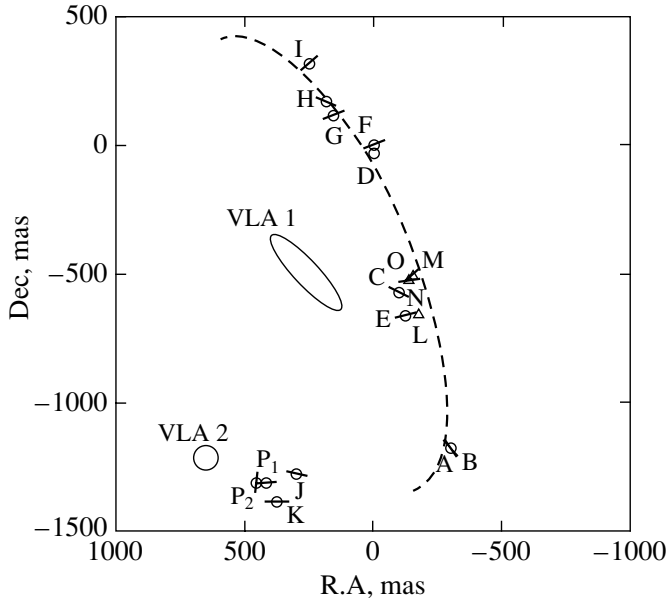

Fig. 2. Positions of the flare precursors P_1 and P_2 (in the vicinity of VLA 2) and the direction of the magnetic field in them (determined from the archival VLBA observations for November 2000 and January 2001; Slysh, private communication). Features P_1 and P_2 are plotted on the VLBA map of OH maser condensations in W75 N taken from the paper by Slysh *et al.* (2002). The circles and triangles denote the 1665- and 1667-MHz features, respectively. The direction of the magnetic field is indicated by the vectors. The positions of the ultracompact H II regions VLA 1 and VLA 2 are indicated by the ellipse and the circumference, respectively. The dashed line shows the disk that is possibly associated with VLA 1.

corresponds to linear sizes of the maser condensation $l_1 \times l_2 = (21.4 \times 4.8)$ AU. If the emission from feature J is assumed to have been produced by the passage of a shock through a clump of matter with the above sizes, then the shock velocity must be no less than $l_1/t = 9.3$ km s^{-1} if the clump lies in the plane of the sky or more if the projection effect is taken into account.

It is unlikely that normal supersonic shocks can propagate with such a velocity, since the speed of sound in molecular clouds is low, less than 1 km s^{-1}. However, magnetohydrodynamic waves propagating with the Alfvèn velocity may well be an agent exciting the maser emission. It is well known that the magnetic field in maser emission regions can exceed 5×10^{-3} G, as follows from Zeeman splitting measurements. Thus, for example, two maser condensations in W75 N have a magnetic field of 5.2×10^{-3} and 7.7×10^{-3} G, respectively (Slysh *et al.* 2002). Taking the magnetic field to be $H = 3 \times 10^{-3}$ G and the gas density to be $n_{H_2} = 10^5$–10^6 cm^{-3}, we obtain Alfvèn velocities of 15 and 5 km s^{-1}, respectively, in agreement with the estimates of the propagation velocity of the disturbance that generated the maser emission of component J. We can assume that having passed through component J, the disturbance traveling with the Alfvèn velocity reached the next condensation, which gave rise to another flare of maser emission. This time, its intensity was a factor of about 50 higher than that of component J, which can be explained by more favorable conditions for the maser emission. More detailed information about the evolution of the maser emission flare with time can be obtained from high-angular-resolution VLBI mapping and from the Radioastron space interferometer.

CONCLUSIONS

We have discovered the brightest flare of maser emission in the OH line in the entire history of observations since 1965. The flare is associated with the activity of the young massive star that excites the ultracompact H II region VLA 2 in the star-forming region W75 N. The onset of the flare was accompanied by a weakening of the emission from other maser condensations associated with VLA 2. Such behavior can be explained by the passage of a magnetohydrodynamic shock through regions of enhanced gas concentration.

ACKNOWLEDGMENTS

We wish to thank B.Z. Kanevskii, A.I. Smirnov, S.V. Logvinenko, V.I. Vasil'kov, and S.V. Kalenskii from the Astrospace Center of the Lebedev Physical Institute and R. Escoffier (NRAO, USA), who designed the receiver and the correlator. We also wish

to thank J.-M. Martin, E. Gerard (the Meudon Observatory, France), and V. Migenes (the University of Guanojuato, Mexico) for their help with the observations, and NRAO data analysts for access to the archive of observations. This work was supported in part by the Russian Foundation for Basic Research (project no. 04-02-17057), CRDF (grant no. RP1-2392-MO-02), the Russian Academy of Sciences' Extended Objects in the Universe basic research program, and the federal Astronomy program and was performed as part of the preparation of the the observational program for the Radioastron space interferometer.

REFERENCES

1. Z. Abraham, N. L. Cohen, R. Opher, *et al.*, Astron. Astrophys. **100**, L10 (1981).
2. A. L. Argon, M. J. Reid, and K. M. Menten, Astrophys. J., Suppl. Ser. **129**, 159 (2000).
3. E. E. Baart, R. J. Cohen, R. D. Davies, *et al.*, Mon. Not. R. Astron. Soc. **219**, 145 (1986).
4. J. L. Caswell and R. F. Haynes, Austr. J. Phys. **36**, 361 (1983).
5. T. R. Hunter, G. B. Taylor, M. Felli, *et al.*, Astron. Astrophys. **284**, 215 (1994).
6. B. Hutawarakorn, R. J. Cohen, and G. C. Brebner, Mon. Not. R. Astron. Soc. **330**, 349 (2002).
7. E. E. Lekht and V. V. Krasnov, Pis'ma Astron. Zh. **26**, 45 (2000) [Astron. Lett. **26**, 38 (2000)].
8. L. I. Matveyenko, Pis'ma Astron. Zh. **7**, 100 (1981) [Sov. Astron. Lett. **7**, 54 (1981)].
9. V. Minier, R. S. Booth, and J. E. Conway, Astron. Astrophys. **362**, 1093 (2000).
10. T. Omodaka, T. Maeda, and N. Mochiduki, IAU Circ., No. 6893 (1998).
11. D. S. Shepherd, S. E. Kurtz, and L. Testi, Astrophys. J. **601**, 952 (2004).
12. V. I. Slysh, M. V. Popov, B. Z. Kanevsky, *et al.*, Pis'ma Astron. Zh. **27**, 323 (2001) [Astron. Lett. **27**, 277 (2001)].
13. V. I. Slysh, V. Migenes, I. E. Val'tts, *et al.*, Astrophys. J. **564**, 317 (2002).
14. J. M. Torrelles, J. F. Gómez, L. F. Rodríguez, *et al.*, Astrophys. J. **489**, 744 (1997).
15. W. van Driel, J. Pezzani, and E. Gerard, *High Sensitivity Radio Astronomy*, Ed. by N. Jackson and R. J. Davis (Cambridge Univ. Press, Cambridge, 1996).

Translate by A. Alakoz

Astronomy Letters, Vol. 31, No. 6, 2005, pp. 380–387. Translated from Pis'ma v Astronomicheskiĭ Zhurnal, Vol. 31, No. 6, 2005, pp. 427–436.

Long-Term INTEGRAL and RXTE Observations of the X-Ray Pulsar LMC X-4

S. S. Tsygankov* **and A. A. Lutovinov**

Space Research Institute, Russian Academy of Sciences, Profsoyuznaya ul. 84/32, Moscow, 117810 Russia

Received January 27, 2005

Abstract—We analyze the observations of the X-ray pulsar LMC X-4 performed by the INTEGRAL observatory and the All-Sky Monitor (ASM) of the RXTE observatory over a wide energy range. The observed hard X-ray flux from the source is shown to change by more than a factor of 50 (from ∼70 mCrab in the high state to ∼1.3 mCrab in the low state) on the time scale of the accretion-disk precession period, whose mean value for 1996–2004 was determined with a high accuracy, $P_{\rm prec} = 30.275 \pm 0.004$ days. In the low state, a flare about 10 h in duration was detected from the source; the flux from the source increased by more than a factor of 4 during this flare. The shape of the pulsar's broadband spectrum is essentially invariable with its intensity; no statistically significant features associated with the possible resonance cyclotron absorption line were found in the spectrum of the source. © *2005 Pleiades Publishing, Inc.*

Key words: *pulsars, neutron stars, X-ray sources.*

INTRODUCTION

The X-ray pulsar LMC X-4 in the Large Magellanic Cloud (LMC) (the distance to the object is $d = 50$ kpc) is a high-mass binary with a pulsation period of ∼13.5 s (Kelley *et al.* 1983), in which the compact object is eclipsed by its optical companion, an O8 star of the 14th magnitude with a mass of $20M_\odot$ (Chevalier and Ilovaisky 1977), every ∼1.408 days (Li *et al.* 1978; Lang *et al.* 1981; Levine *et al.* 2000). Levine *et al.* (2000) provided the following orbital parameters for the binary: $a_x \sin i = 26.333 \pm 0.019$ light seconds, the eccentricity $e < 0.003(2\sigma)$, and the epoch of the zero orbital phase $T_0 =$ MJD51110.86571.

Lang *et al.* (1981) pointed to the existence of a superorbital period in the binary, ∼30.5 days, within which the intensity of the source changes by a factor of about 60. These authors also assumed that this effect is produced by the blockage of direct X-rays by a precessing accretion disk tilted with respect to the orbital plane, much as is the case in the binary Her X-1 (Tananbaum *et al.* 1972). Based on the measurements of almost the same X-ray flux observed from the source during eclipses in its low and high states, Woo *et al.* (1995) concluded that the intrinsic luminosity of the pulsar is constant, which also confirms the assumption made by Lang *et al.* (1981). Having analyzed the RXTE and GINGA observations, Paul and Kitamoto (2002) estimated the rate of decrease in the precession period of the accretion disk to be $\dot{P} \sim -2 \times 10^{-5}$ s s^{-1}.

The flaring activity of LMC X-4 has been widely discussed in the literature (see, e.g., Epstein *et al.* 1977; Skinner *et al.* 1980; Kelley *et al.* 1983; Levine *et al.* 1991). A flare with a duration from dozens of seconds to dozens of minutes is detected from the source during its high state, on average, once a day. However, there is also evidence (Woo *et al.* 1995) for the presence of bursts in the low state.

In different periods, the pulsar LMC X-4 demonstrates both a spin-down and a spin-up, suggesting that its period is close to its equilibrium value. In this case, according to the disk-accretion theory (Ghosh and Lamb 1979), a neutron star with an equilibrium period of ∼13.5 s and an X-ray luminosity of $\sim 4 \times 10^{38}$ erg s^{-1} would have a very high magnetic moment, $\sim 10^{31.5}$ G cm^3 (Woo *et al.* 1996).

The spectrum of the source above several keV is described by a power law with a high-energy cutoff. The measured absorption column density toward the source (along with the best-fit parameters) does not depend on the phase of the precession period; its value, $N_{\rm H} \sim 5.5 \times 10^{20}$ atoms cm^{-2}, is close to the Galactic column density, suggesting the absence of strong internal absorption in the binary (Naik and Paul 2003). Different authors (Levine *et al.* 1991; Mihara 1995; Woo *et al.* 1996; La Barbera *et al.* 2001) obtained several estimates for the presence of a cyclotron absorption line in the source's spectrum in the

*E-mail: st@hea.iki.rssi.ru

energy range 19 to 100 keV, but as yet there are no reliable measurements of its intensity and, accordingly, the surface magnetic field of the neutron star.

In this paper, we present the results of our timing and spectral analyses for the pulsar LMC X-4 performed by using INTEGRAL and RXTE observations over a wide (1–100 keV) energy range. Preliminary results were obtained by Lutovinov *et al.* (2004).

OBSERVATIONS

The INTEGRAL International observatory (Winkler *et al.* 2003), which carries four scientific instruments that allow the emission from astrophysical objects to be studied over a wide wavelength range (from optical to hard γ rays), was placed in orbit by a Russian Proton launcher on October 17, 2002 (Eismont *et al.* 2003).

In this paper, we analyze the data obtained with the ISGRI detector of the IBIS gamma-ray telescope (Ubertini *et al.* 2003) and the JEM-X X-ray monitor of the INTEGRAL observatory (Lund *et al.* 2003). The ISGRI detector has an effective area of $\sim$960 cm^2 at 50 keV, is effectively sensitive to photons in the energy range 20 to 200 keV (the energy resolution is $\sim$7% at 100 keV), and allows the image of the sky within a $29^\circ \times 29^\circ$ field of view (the full coding zone is $9^\circ \times 9^\circ$) to be reconstructed with a nominal spatial resolution of $\sim$12 arcmin (the angular size of the mask element). See Lebrun *et al.* (2003) for a more detailed description of the detector. The main elements of the two identical JEM-X modules (JEM-X1 and JEM-X2) are coded mask xenon–methane gas chambers placed at about 3.2 m from the plane of the detectors. Each module of the telescope has the following technical characteristics: the energy range 3–35 keV, the field of view (the full coding zone) 13.2° (4.8°) in diameter, and the detector area 500 cm^2 (Lund *et al.* 2003).

About 500 individual pointings were made as part of the studies of the LMC region performed by the INTEGRAL observatory from January 2 through January 28, 2003, during which the pulsar LMC X-4 was within the field of view of the INTEGRAL instruments. The total observing time for the source was $\sim 10^6$ s; at all pointings, it was in the full coding zone. We also used data from the All-Sky Monitor (ASM) of the RXTE observatory (http://xte.mit.edu/ASM_lc.html) to analyze the long-period characteristics of the source. These data are daily averaged fluxes from the source in the energy range 1.3–12.2 keV.

We constructed an X-ray image and performed a spectral analysis of the IBIS data using the methods described by Revnivtsev *et al.* (2004) and Lutovinov *et al.* (2003). An analysis of a large set of calibration observations for the Crab Nebula revealed a systematic error of $\sim$10% in the estimated absolute flux from the source over a wide energy range; the spectral shape was reconstructed with an accuracy as high as 3–5%. We took this into account in our spectral analysis by adding a systematic error of 5%. All of the errors given in this paper are purely statistical. The standard OSA software of version 4.1, which was provided by the INTEGRAL Science Data Center (http://isdc.unige.ch), was used for our timing analysis of the source on pulsation period time scales and for our analysis of the JEM-X data.

Figure 1 shows the IBIS 20–60 keV map of the LMC region. This map was constructed over the entire period of the source's observations in January 2003. Apart from the pulsar LMC X-4 itself, the black hole LMC X-1 and the single pulsar PSR 0540–69 are detected in the image at a statistically significant level. No emission is detected from the SN 1987A remnant (Shtykovskiy *et al.* 2005).

TIMING ANALYSIS

The Precession Period

As was said in the Introduction, there is a period of about 30 days in the binary LMC X-4 that is most likely related to the eclipse of the neutron star's emitting regions by a precessing tilted accretion disk. To determine the exact precession period, we used the ASM/RXTE data obtained from January 1996 through July 2004. The best precession period of the accretion disk was found by the epoch-folding technique (Leahy *et al.* 1983) to be 30.275 days. We used the following method to estimate the error of this measurement: for each point on the light curve of the source within a 1σ error in the flux, we randomly chose a point that was used as a new flux from the source. In this way, we modeled another light curve for which, in turn, the best period was determined. We obtained a total of about 100 periods whose spread was considered to be a 1σ confidence interval. Such an analysis yielded the following mean precession period of the accretion disk for 1996–2004: $P_{\rm prec} = 30.275 \pm 0.004$ days.

The hard X-ray (20–50 keV) light curve of the source shown in Fig. 2a has a characteristic shape. About 2 days after the beginning of its observations, the pulsar switched to the high state; in another 5 days, its flux increased by a factor of about 6–8 and reached a peak ($\sim$70 mCrab). The arrows in the figure indicate the switch-on and switch-off times estimated more than 20 years ago by Lang *et al.* (1981); the switch-on time was calculated by using the ephemerides derived by these authors; the

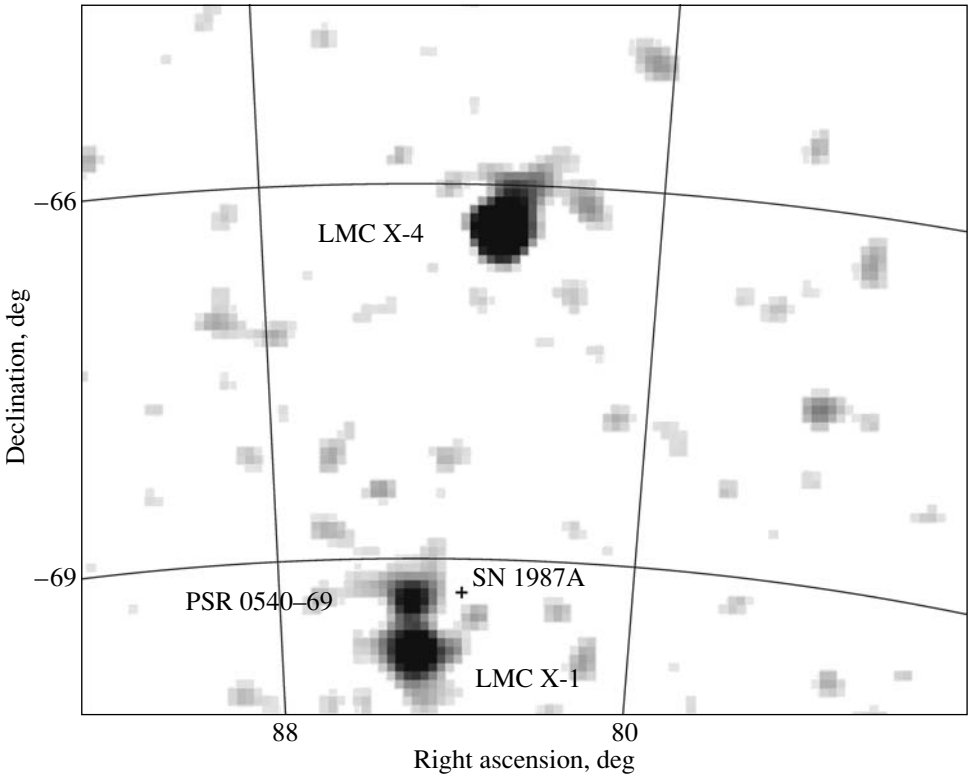

Fig. 1. IBIS/INTEGRAL 20–60 keV image of the LMC region containing the X-ray pulsar LMC X-4. The sources detected at a statistically significant level are labeled; the position of the SN 1987A remnant is indicated by the cross.

switch-off time was determined by assuming that the high state of the source lasted ~60% of the entire precession period (Lang *et al.* 1981). We see that the presumed zero phase (switch-on time) of the superorbital cycle is greatly shifted relative to the current INTEGRAL measurements. Note that the same relationship between the durations of the high and low states is also obtained from the INTEGRAL observations of the source (Fig. 2a).

Unfortunately, the switch-on time of the object under study was not observed by the INTEGRAL observatory directly, and we had to use interpolation to determine the zero phase of the precession period. The switch-on time of the pulsar LMC X-4 estimated in this way is MJD 52644.5 ± 1.0. Owing to good statistics and a long series of observations, we were able to determine the mean precession period with a high accuracy (see above), which ensures the determination of the presumed zero phase 20 years ago with an accuracy of ~1 day by assuming the period to be constant. Using our value of the precession period, we can calculate the presumed zero phase closest to that measured by Lang *et al.* (1981). Our result is either ~18.5 days before or ~12 days after this time. Thus, the precession period of the accretion disk, on average, must either increase with $\dot{P} \sim 1.3 \times 10^{-3}$ s s^{-1} or decrease with $\dot{P} \sim -2 \times 10^{-3}$ s s^{-1}. Here, we give lower limits on the rate of change in the period, since we disregard the change that is a multiple of an integer number of periods.

On the other hand, the mean rate of change in the precession period can be estimated by using our values and those obtained by Lang *et al.* (1981). This estimation yields a value of $\dot{P} = (-2.5 \pm 0.8) \times 10^{-5}$ s s^{-1}, which is much lower than our previous estimate obtained by extrapolating the switch-on times and agrees, within the error limits, with the value determined by Paul and Kitamoto (2002).

The observed discrepancy in the estimated rates of change in the precession period may stem from the fact that the precession period of the accretion disk for the pulsar LMC X-4 has evolved not uniformly, but with spinups/spindowns much higher than the average level.

Using long-term ASM/RXTE observations (January 1996–August 2002), Klarkson *et al.* (2003) constructed a dynamic power spectrum for the source under study. Throughout the period of observations, the precession period was constant near 30.28 days. However, due to the 3σ error of ± 0.46 days, no firm conclusion about the precession-period variations can be reached.

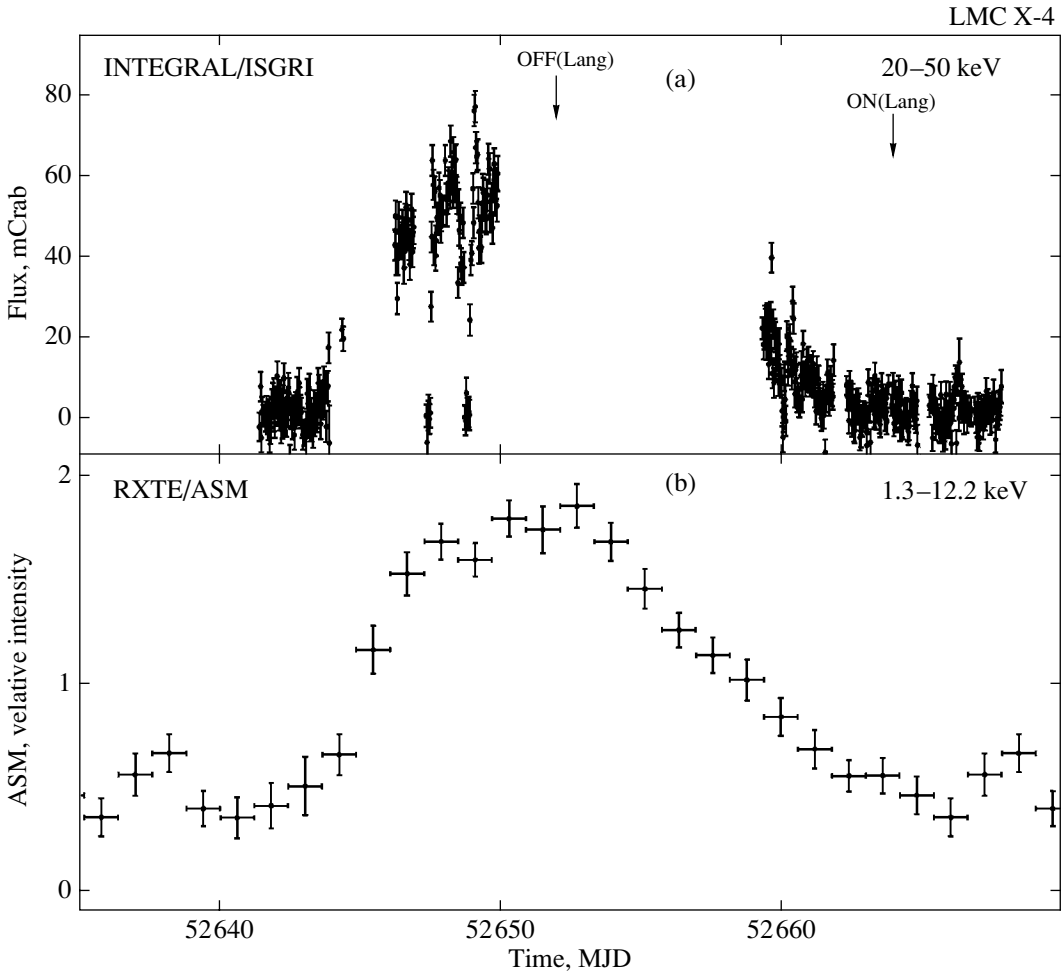

Fig. 2. (a) Hard X-ray (20–50 keV) light curve for the pulsar LMC X-4 constructed from IBIS/INTEGRAL data. The arrows indicate the switching-on and switching-off times for the source, as estimated by other authors. (b) The light curve for the source constructed from ASM/RXTE data over eight years of observations and folded with the best period derived from these data. The errors correspond to one standard deviation.

Figure 2b shows the averaged light curve of the pulsar LMC X-4 constructed from ASM/RXTE data over ~8.5 years of its observations and folded with the best period of 30.275 days. Interestingly, there is a statistically significant rise in the source's intensity with a duration of about three days near phase ~0.8 of this cycle. A similar feature in the light curve of the pulsar can be seen in Figs. 1 and 3 from Lang *et al.* (1981). A similar rise in the source's intensity during the off state is also observed in another X-ray pulsar, Her X-1 (Jones and Forman 1976).

The Orbital Period

Figure 3a shows the 20–50 keV light curve for the pulsar LMC X-4 when the source was near the peak of its observed X-ray flux. The times of the eclipses of the X-ray source by its optical companion are clearly seen from this figure. The ingress and egress were accompanied by smooth variations in the pulsar's observed intensity. However, a significant rise in the flux from the source with a duration of about three hours was observed a short time (on the order of an hour) after the egress. The ingress and egress duration can be estimated from the source's light curve, ~3 ks. At the neutron star's orbital velocity of about 500 km s^{-1} (Kelley *et al.* 1983), this corresponds to the transition region's size of $\sim 1.5 \times 10^6$ km, which is comparable to the sizes of the atmospheres of late-O main sequence stars (Woo *et al.* 1996).

The time dependence of the hardness, which is defined as the ratio of the fluxes from the source in the 40–60 and 20–40 keV energy bands, is shown in Fig. 3b. We see a tendency for the radiation from the object under study to soften as it approaches an eclipse, but this dependence breaks down immediately after the eclipse. The hardness during the eclipses themselves is not shown in the figure, be-

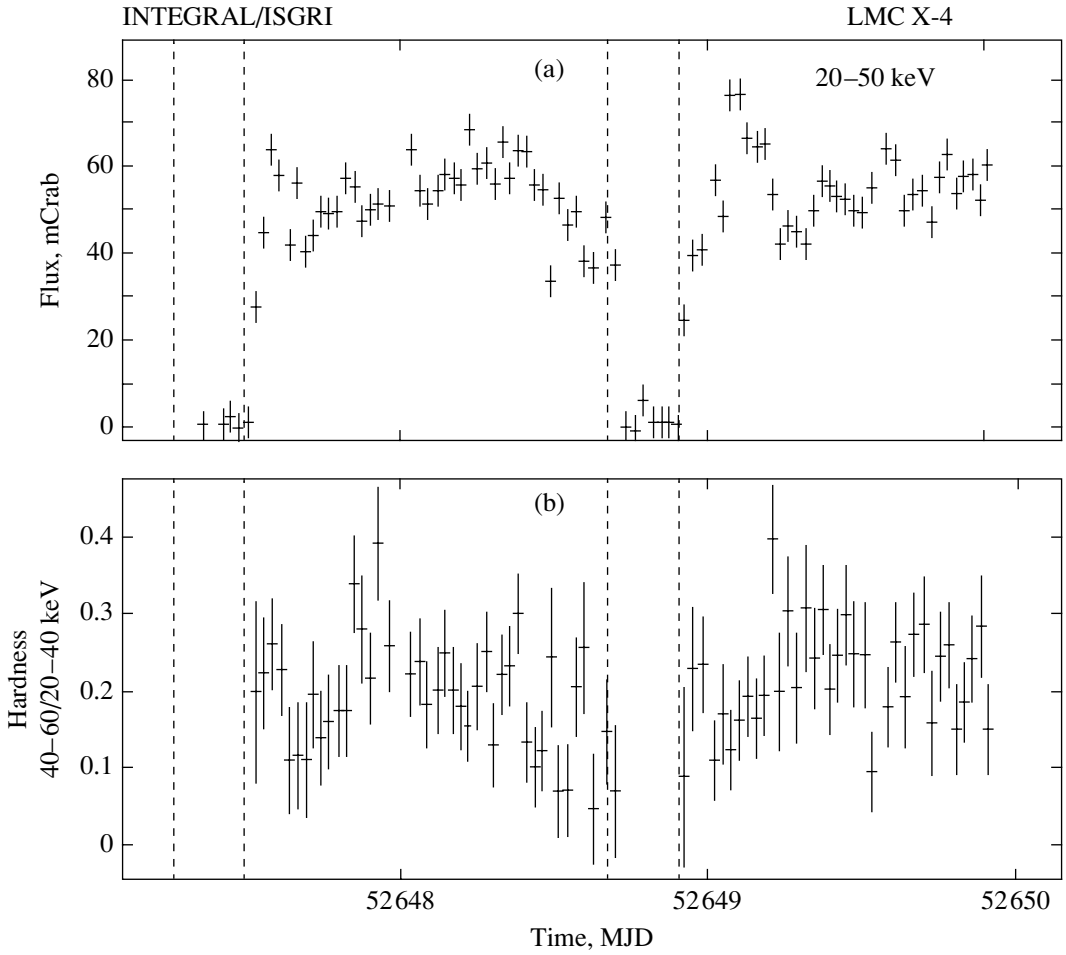

Fig. 3. (a) Orbital light curve for the pulsar LMC X-4 constructed from IBIS data during its high state. The dashed lines indicate the ingress and egress times estimated by Lang *et al.* (1981). (b) Variations of the source's hardness on the time scale of the orbital period. The errors correspond to one standard deviation.

cause no statistically significant flux can be recorded from the source.

The dashed lines indicate the eclipse ephemerides taken from the papers by Li *et al.* (1978), Lang *et al.* (1981), and Levine *et al.* (2000). Note that the orbital period in the binary is highly stable and has been almost constant over more than twenty years of the pulsar's studies. The INTEGRAL observations of the source in 2003 confirm this conclusion (see Fig. 3). Several authors (Woo *et al.* 1996; Levine *et al.* 2000) have attempted to measure the rate of change in the orbital period, but the significance of the values obtained is low ($\dot{P}_{\rm orb}/P_{\rm orb} = (-5.3 \pm 2.7) \times 10^{-7}$ yr^{-1} and $\dot{P}_{\rm orb}/P_{\rm orb} = (1.1 \pm 0.8) \times 10^{-6}$ yr^{-1}, respectively) and is consistent with the observational data.

Note that the low-state flux from the source does not drop to zero and is recorded by the INTEGRAL instruments, although it decreases. Thus, for example, according to the observational data spanning the time interval MJD 52662.5–52665, the 20–50 keV flux from the source was 2.6 ± 0.4 mCrab, while several days later, MJD 52667–52668, it decreased by almost a factor of 2, 1.3 ± 0.5 mCrab.

The intensity of the pulsar LMC X-4 decreases sharply during its X-ray eclipses. We analyzed the flux during eclipses for two time intervals, when the source was in its high and low states (MJD 52648.8 and MJD 52665, respectively). In both cases, no emission was detected from the object under study at a statistically significant level, and we obtained only upper limits on its 20–50 keV flux, which proved to be identical, $\sim$1.2 mCrab (1σ). Note that during the X-ray eclipse on January 20, 2003, (MJD 52659.94–52660.17), when the source's intensity decreased, its observed 20–50 keV flux was significantly higher than the above upper limits, 3.7 ± 1.0 mCrab, but the significance of this measurement is low. A similar analysis for the soft (0.1–2.4 keV) X-ray emission was performed by Woo *et al.* (1995). The results obtained by these authors suggest that the source's

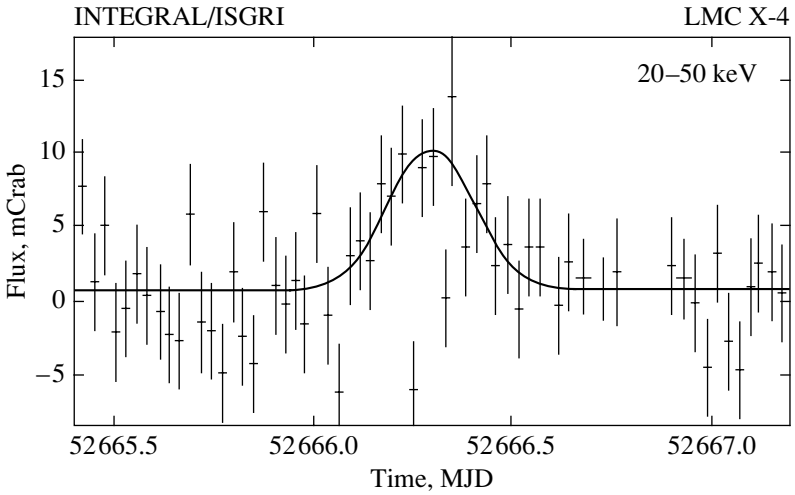

Fig. 4. Flare detected by the IBIS telescope of the INTEGRAL observatory from the pulsar LMC X-4 on January 27, 2003, during the low state. The solid line indicates a Gaussian fit to the flare profile.

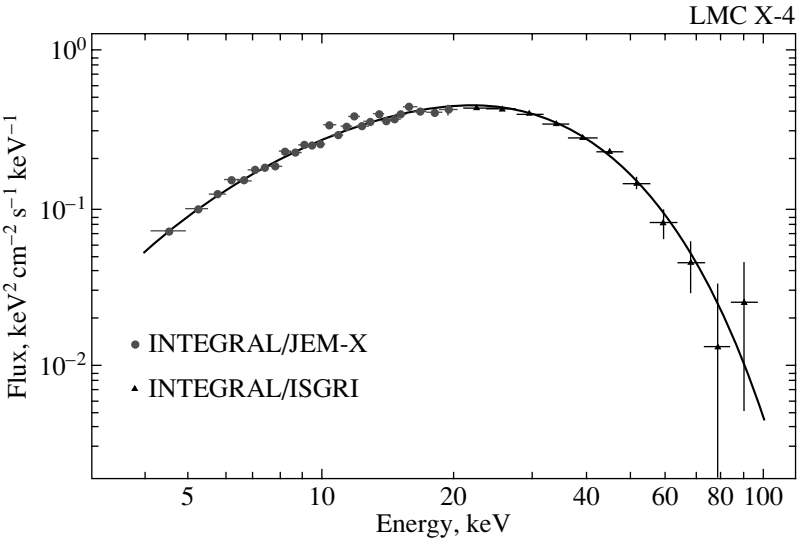

Fig. 5. Energy spectrum of the source LMC X-4 during its high state constructed from JEM-X and IBIS data. The dots indicate the experimental spectrum; the solid line represents its power-law fit with a high-energy cutoff.

intensity is constant during its eclipses, which they interpreted as evidence that the pulsar's intrinsic luminosity is constant. This conclusion was based on the assumption that the X-rays observed during an eclipse are scattered by the widely distributed matter around the source, possibly the corona above the outer edges of the accretion disk, much as is the case in the pulsar Her X-1 (Lutovinov *et al.* 2000).

Flares

Many authors have described the flaring activity of the pulsar LMC X-4. Short flares (up to 1000 s in duration), during which the pulsar's intensity changes by a factor of 2 to 5, are most characteristic of the source under study (Levine *et al.* 2000).

An rise in the observed flux from the source was recorded during its low state (MJD 52666) on a time scale atypical of it. The flare duration was about 10 h (orbital phase 0.3–0.6), and the peak intensity ($\sim$10 mCrab) exceeded the average low-state level by a factor of about 4. Figure 4 shows the flare profile constructed from IBIS data in the 20–50 keV energy band.

SPECTRAL ANALYSIS

In the previous section, we showed that a significant number of features could be distinguished in the light curve of the pulsar LMC X-4. Therefore, studying the spectral evolution of the source with time is of considerable interest. Another goal of the spectral analysis was the search for the possible cyclotron

Best-fit parameters for the spectrum of LMC X-4 derived from INTEGRAL data (JEM-X + IBIS)[a]

State	Luminosity, 10^{37} erg s^{-1} [b]	α	E_c, keV	E_f, keV	$\chi^2_N(N)$[c]
High (MJD 52646–52650)	38.7	0.20 ± 0.15	9.1 ± 0.8	11.0 ± 0.6	0.88(128)
Flares (in high state)	47.9	0.44 ± 0.20	8.9 ± 1.0	11.9 ± 0.8	0.82(126)
Low (MJD 52662.5–52668)	1.4	0.2[d]	9.1[d]	14.8 ± 3.2	1.19(4)
Flare (MJD 52666)	3.1	0.2[d]	9.1[d]	17.1 ± 5.3	0.41(6)

[a] All errors are given at a 1σ level.
[b] The 4–100 keV luminosity at an assumed distance to the source of 50 kpc.
[c] The χ^2 value normalized to the number of degrees of freedom N.
[d] The parameters were fixed at the values obtained for the high state.

resonance absorption line whose existence was mentioned by several authors (see the Introduction).

A power law with an exponential high-energy cutoff (White *et al.* 1983), which is typical of this class of objects, was chosen as a basis for the spectral analysis of the source over a wide (4–100 keV) energy range:

$$I(E) = AE^{-\alpha} \times \begin{cases} 1, & E < E_c \\ \exp[-(E - E_c)/E_f], & E \geq E_c, \end{cases} \quad (1)$$

where E is the photon energy in keV, A is the normalization of the power-law component, α is the photon index, E_c is the cutoff energy, and E_f is the e-folding energy in the source's spectrum. We identified a total of four states in which an independent analysis of the pulsar's spectrum was performed: the high state (without including the X-ray eclipse times), the bursts immediately after the source's egress, the low state (without including the X-ray eclipse times), and the flare occurred on January 27, 2003 (MJD 52666).

The best-fit parameters for the source's spectra based on model (1) are given in the table. We were able to reconstruct the spectra over a wide energy range (using JEM-X data) only in the high state. Since the JEM-X monitor is not sensitive enough, the source was detected at a statistically significant level only by the IBIS telescope. Therefore, when fitting the spectra in this state, we fixed the parameters in the standard X-ray energy range (<20 keV) at the values obtained for the high state. We see from the table that the shape of the source's spectrum and its parameters (slope and cutoff parameters) remain almost constant with the pulsar's intensity variations. Figure 5 shows the energy spectrum of LMC X-4 reconstructed from INTEGRAL data in a wide energy range for the high state.

To test the hypothesis about the presence of a cyclotron feature in the source's spectrum within the energy range 4–100 keV, we modified the fitting model by adding the corresponding component:

$$\exp\left[-\frac{A_{cyc}W_{cyc}^2(E/E_{cyc})^2}{(E - E_{cyc})^2 + W_{cyc}^2}\right], \quad (2)$$

where E is the photon energy in keV, E_{cyc} is the cyclotron energy, W_{cyc} is the width of the cyclotron line, and A_{cyc} is its depth.

Using the modified model, we fitted the pulsar's spectrum during the high state, except the X-ray eclipse times. We used the same procedure that was employed to study the X-ray pulsar KS 1947+300 (Tsygankov and Lutovinov 2005): the energy of the center of the presumed cyclotron line E_{cyc} was varied over the range 5–100 keV at 5-keV step, while its width was fixed at 5 keV; for each trial energy of the line center, we tested the significance of an improvement in statistics using the $\Delta\chi^2$ test. As a result, we found no such energy of the cyclotron line E_{cyc} in the energy range under study whose inclusion in the model would lead to an improvement in the quality of the spectral fit by more than 2σ.

The result obtained could mean that either the energy of the cyclotron line lies outside our energy range (4–100 keV) or the INTEGRAL instruments are not sensitive enough for the cyclotron line to be detected in the spectrum of the source LMC X-4. The relationship between the spin period of the neutron star and its luminosity, assuming that the period is close to its equilibrium value, argues for the hypothesis of a strong magnetic field (>10^{13} G) in the binary (Woo *et al.* 1996).

CONCLUSIONS

We presented the results of our long-term timing and spectral analyses for the X-ray pulsar LMC X-4 performed by using the INTEGRAL observations in January 2003 and the long-term (1996–2004)

ASM/RXTE observations. We determined the precession period (30.275 ± 0.004 days) averaged over the last ~8.5 years with high accuracy. Since the source's switch-on times predicted by different authors do not coincide, we showed that this parameter is not constant and most likely varies nonuniformly. The IBIS/INTEGRAL data revealed small bursts that emerged after the egress of the X-ray source. We detected a flare about 10 h in duration during the low state. On the time scales of the orbital period, its value determined more than 20 years ago is stable and satisfies well our observational data. We performed a spectral analysis for different states distinguishable by the object's intensity. The spectrum of the source is described by a power law with a high-energy cutoff, which is characteristic of this class of objects. To test the hypothesis about the presence of a cyclotron feature in the source's spectrum within the energy range 4–100 keV, we properly modified the fitting model. This analysis showed that there is no such feature in the source's spectrum at a confidence level exceeding 2σ. A comparison of the derived constraints with the results of other authors (Woo *et al.* 1996) is more likely indicative of a strong magnetic field ($>10^{13}$ G) on the neutron-star surface than a weak field ($<5 \times 10^{11}$ G).

ACKNOWLEDGMENTS

We wish to thank E.M. Churazov, who developed the methods and software for analyzing the data from the IBIS telescope of the INTEGRAL observatory. This work was supported by the Russian Foundation for Basic Research (project no. 04-02-17276). We used the data retrieved from the High-Energy Astrophysics Archive at the Goddard Space Flight Center of NASA and the data retrieved from the Archive of the INTEGRAL Science Data Center (Versoix, Switzerland) and the Russian INTEGRAL Science Data Center (Moscow, Russia). This study was performed in part during the visits to the INTEGRAL Science Data Center (Versoix, Switzerland), and we are grateful to its staff for hospitality. A.A. Lutovinov is also grateful to the ESA for financial support of some of these visits.

REFERENCES

1. C. Chevalier and S. Ilovaisky, Astron. Astrophys. **59**, L9 (1977).
2. W. I. Clarkson, P. A. Charles, M. I. Coe, *et al.*, Mon. Not. R. Astron. Soc. **343**, 1213 (2003).
3. N. A. Eismont, A. V. Ditrikh, G. Janin, *et al.*, Astron. Astrophys. **411**, L37 (2003).
4. A. Epstein, J. Delvaille, H. Helmken, *et al.*, Astrophys. J. **216**, 103 (1977).
5. P. Ghosh and F. Lamb, Astrophys. J. **234**, 296 (1979).
6. C. Jones and W. Forman, Astrophys. J. **209**, L131 (1976).
7. R. L. Kelley, J. G. Jernigan, A. Levine, *et al.*, Astrophys. J. **264**, 568 (1983).
8. A. La Barbera, L. Burderi, T. Di Salvo, *et al.*, Astrophys. J. **553**, 375 (2001).
9. F. L. Lang, A. M. Levine, M. Bautz, *et al.*, Astrophys. J. **246**, L21 (1981).
10. D. A. Leahy, R. F. Elsner, and M. C. Weisskopf, Astrophys. J. **272**, 256 (1983).
11. F. Lebrum, J. P. Leray, P. Lavocat, *et al.*, Astron. Astrophys. **411**, L141 (2003).
12. A. Levine, S. Rappaport, A. Putney, *et al.*, Astrophys. J. **381**, 101 (1991).
13. A. Levine, S. Rappaport, and G. Zojcheski, Astrophys. J. **541**, 194 (2000).
14. F. Li, S. Rappaport, and A. Epstein, Nature **271**, 37 (1978).
15. N. Lund, S. Brandt, C. Budtz-Joergesen, *et al.*, Astron. Astrophys. **411**, L231 (2003).
16. A. A. Lutovinov, S. A. Grebenev, M. N. Pavlinsky, and R. A. Sunyaev, Pis'ma Astron. Zh. **26**, 803 (2000) [Astron. Lett. **26**, 765 (2000)].
17. A. A. Lutovinov, S. V. Mol'kov, and M. G. Revnivtsev, Pis'ma Astron. Zh. **29**, 803 (2003) [Astron. Lett. **29**, 713 (2003)].
18. A. A. Lutovinov, S. S. Tsygankov, M. G. Revnivtsev, *et al.*, in *Proceedings of the V INTEGRAL Workshop*, ESA SP **552**, 253 (2004).
19. T. Mihara, PhD Thesis (Univ. Tokyo, Tokyo, 1995).
20. S. Naik and B. Paul, Astron. Astrophys. **401**, 265 (2003).
21. B. Paul and S. Kitamoto, J. Astrophys. Astron. **23**, 33 (2002).
22. M. G. Revnivtsev, R. A. Syunyaev, D. A. Varshalovich, *et al.*, Astron. Lett. **30**, 382 (2004).
23. P. E. Shtykovskiy, A. A. Lutovinov, M. R. Gilfanov, and R. A. Sunyaev, Pis'ma Astron. Zh. **31**, 284 (2005) [Astron. Lett. **31**, 258 (2005)].
24. G. K. Skinner, S. Shulman, and G. Share, Astrophys. J. **240**, 619 (1980).
25. H. Tananbaum, H. Gursky, E. Kellog, *et al.*, Astrophys. J. **174**, L143 (1972).
26. S. S. Tsygankov and A. A. Lutovinov, Pis'ma Astron. Zh. **31**, 99 (2005) [Astron. Lett. **31**, 88 (2005)].
27. P. Ubertini, F. Lebrum, G. Di Cocco, *et al.*, Astron. Astrophys. **411**, L131 (2003).
28. N. White, J. Swank, and S. Holt, Astrophys. J. **270**, 771 (1983).
29. C. Winkler, T. J.-L. Courvoisier, G. Di Cocco, *et al.*, Astron. Astrophys. **411**, L1 (2003).
30. J. W. Woo, G. W. Clark, and A. M. Levine, Astrophys. J. **449**, 880 (1995).
31. J. W. Woo, G. W. Clark, A. M. Levine, *et al.*, Astrophys. J. **467**, 811 (1996).

Translated by V. Astakhov

Astronomy Letters, Vol. 31, No. 6, 2005, pp. 388–397. Translated from Pis'ma v Astronomicheskiĭ Zhurnal, Vol. 31, No. 6, 2005, pp. 437–446.

Temperature Behavior of Elemental Abundances in the Atmospheres of Magnetic Peculiar Stars

T. A. Ryabchikova*

Institute of Astronomy, Russian Academy of Sciences, ul. Pyatnitskaya 48, Moscow, 119017 Russia

Received January 25, 2005

Abstract—We analyze the temperature dependence of the abundances of the chemical elements Si, Ca, Cr, and Fe in the atmospheres of normal, metallic-line (Am), magnetic peculiar (Ap), and pulsating magnetic peculiar (roAp) stars in the range 6000–15 000 K. The Cr and Fe abundances in the atmospheres of Ap stars increase rapidly as the temperature rises from 6000 to 9000–10 000 K. Subsequently, the Cr abundance decreases to values that exceed the solar abundance by an order of magnitude, while the Fe abundance remains enhanced by approximately +1.0 dex compared to the solar value. The temperature dependence of the abundances of these elements in the atmospheres of normal and Am stars is similar in shape, but its maximum is several orders of magnitude lower than that observed for Ap stars. In the range 6000–9500 K, the observed temperature dependences for Ap stars are satisfactorily described in terms of element diffusion under the combined action of gravitational settling and radiative acceleration. It may well be that diffusion also takes place in the atmospheres of normal stars, but its efficiency is very low due to the presence of microturbulence. We show that the magnetic field has virtually no effect on the Cr and Fe diffusion in Ap stars in the range of effective temperatures 6000–9500 K. The Ca abundance and its variation in the atmospheres of Ap stars can also be explained in terms of the diffusion model if we assume the existence of a stellar wind with a variable moderate rate of $\sim(2-4)\times10^{-15}M_\odot$ yr^{-1}.

Key words: *Peculiar stars, chemical content, diffusion.*

INTRODUCTION

Magnetic chemically peculiar (Ap) stars are upper-main-sequence stars with anomalously strong lines of certain chemical elements (Si, Cr, Sr, Eu) in their spectra. They also possess global poloidal magnetic fields whose longitudinal components vary over a wide range, from dozens of gauss (Aurière *et al.* 2005) to dozens of kilogauss, as in the well-known star HD 215441 of Babcock (1960). The anomalous chemical elements gave names to the subtypes of Ap stars: Si, SiCr, and SrCrEu stars. Despite the observed anomalies, the global characteristics of Ap stars (their spectral energy distribution, photometric indices, and hydrogen-line intensities) do not differ greatly from those of normal stars of the same spectral type, which makes it possible to study their atmospheres in the first approximation by standard methods. An analysis of the atmospheric chemical composition for Ap stars shows that the abundances of the anomalous elements exceed those in the solar atmosphere by several orders of magnitudes. Of course, these anomalies do not refer to the chemical composition of a star as a whole; otherwise, its global characteristics would not correspond to main-sequence stars. They are localized only in a small part of the star, the stellar atmosphere. Michaud (1970) considered the formation of chemical anomalies in stellar atmospheres stable to turbulent motions in which element diffusion proceeds under the combined action of gravitational settling and radiative acceleration. Depending on which of the processes predominates, a chemical element can sink down from the bottom of the convection zone (helium is the best example) or rise and accumulate in the atmosphere. The convection zone (e.g., the H II zone) acts as a reservoir that ensures element accumulation in the upper radiative atmospheric layers. Michaud *et al.* (1976) computed the diffusion of chemical elements in the envelopes of stars with masses from one to five solar masses. Here, by "the envelopes" we mean the layers beneath the photosphere. These first approximate computations showed that certain elements (Mg, Ca) must be underabundant in (1.2–2.0) $M_\odot$ stars, while the iron-peak elements must exhibit an overabundance starting from a mass of $1.4M_\odot$, which corresponds to an effective temperature of 6500 K. Interestingly, the iron itself must be underabundant up to $T_{\rm eff} = 9000$ K. These authors

*E-mail: ryabchik@inasan.rssi.ru

1063-7737/05/3106-0388$26.00

pointed out that all computations for stars with $M \geq 2.6 M_\odot$ are subject to large errors, because for hotter stars with $T_{\rm eff} > 10\,000$ K, the H II convection zone disappears completely, and the computations begin from the layers where the diffusion approximation for the radiative flux, which is valid for large optical depths, is no longer applicable. It is necessary to consider the detailed atomic structure of each element in the first ionization stages and to solve the transport equation for a large number of frequencies. Such computations were performed by Babel (1992) for Ca, Ti, Cr, Mn, and Sr and a temperature of 8500 K; this author showed for the first time that diffusion in a stellar atmosphere leads to steep gradients in the distribution of elemental abundances. In the first approximation, this distribution can be represented by a step function with a jump at the depth of the upper boundary of the H II convection zone, which corresponds to $\log \tau_{5000} \sim -0.6$ according to Schwarzschild's criterion. Recently, diffusion computations have been introduced in model atmosphere computations (see, e.g., LeBlanc and Monin 2004), and it has become possible to construct self-consistent diffusion models to be compared with observations. However, such computations are time-consuming and have been carried out so far only for a few effective temperatures near 8000 K.

In this paper, we analyze the determinations of the Si, Ca, Cr, and Fe abundances in the atmospheres of peculiar stars over a wide range of effective temperatures (6000–15 000 K) and compare them with those in the atmospheres of normal main sequence stars and with predictions of the diffusion theory.

THE TEMPERATURE DEPENDENCE OF ELEMENTAL ABUNDANCES FOR STARS

From the literature, we selected normal stars (51), metallic-line Am stars (20), magnetic peculiar Ap stars (32), and pulsating magnetic peculiar roAp stars (14), which represent the coolest Ap stars. Homogeneity of the method for determining the chemical composition and a low rotational velocity, $v_{\rm e} \sin i \leq 50$ km s^{-1}, served as the selection criteria. For example, we took the elemental abundances in the atmospheres of normal and Am stars from a series of papers of Adelman's team (see references in the table), from Varenne and Monier (1999), and from Hill and Landstreet (1993). A comparison of the results for the same stars in these papers showed agreement between the model atmosphere parameters and the derived abundances, within the typical error limits of the abundance analysis: ±150 K for the effective temperature and ±0.15 dex for the abundances. The elemental abundances in the atmospheres of peculiar stars were taken mostly from our own papers and from those of Adelman's team. For two stars, HD 153882 (Ryabchikova *et al.* 1995) and α^2 CVn (Kochukhov *et al.* 2002), we used the weighted means determined from the maps of element distribution over the stellar surface. In all the remaining cases, the spectroscopic variability characteristic of many peculiar stars was disregarded; therefore, part of the scatter in elemental abundances may be attributable to this fact. Only five of the 32 Ap stars have no magnetic-field measurements, with two of them exhibiting spectroscopic and photometric variability typical of magnetic stars. The methods for determining the chemical composition used by different teams were also compared by Ryabchikova *et al.* (2004a). Almost all the determinations of the stellar atmospheric abundances use model atmospheres computed with the ATLAS9 code (Kurucz 1993). Atomic data, mainly the oscillator strengths of spectral lines, are of greatest importance in determining the chemical composition. Since for the elements Si, Ca, Cr, and Fe under consideration, the overwhelming majority of works used the oscillator strengths included in the Vienna atomic line database, VALD (Kupka *et al.* 1999; Ryabchikova *et al.* 1999), the inhomogeneity effect of the atomic data in our sample of elemental abundances was minimized. In those cases where the abundance of an element was determined from lines in two ionization stages and the numbers of lines were comparable, we used a mean for the two stages. If the results differed by more than 0.3 dex, we took the elemental abundance in the ionization stage with the predominant number of lines. The Si, Ca, Cr, and Fe abundances in the atmospheres of all stars in our sample are presented in the table, where the first and second columns give the star's HD number and its effective temperature, respectively. The last column gives a reference to the paper from which the elemental abundances were taken. The table contains no abundance errors, but these are shown in the corresponding figures for Ap stars, which exhibit the largest scatter.

In Figs. 1 and 2, the abundances of the elements under study are plotted against the stellar effective temperature. The horizontal lines indicate the solar abundances of the elements. Although, in general, the Si and Ca abundances in Ap stars show a correlation with the effective temperature (the abundances increase up to $T_{\rm eff} = 10\,000$–$12\,000$ K and then decrease almost to their solar values), fairly large deviations that can be attributed in part to a nonuniform Si distribution over the stellar surface are encountered. One of the two Ap stars with the largest Si underabundance, HD 108662 (17 Com A), is a spectroscopic variable, and, depending on the phase of observations, both an overabundance and an underabundance can be observed (Savanov *et al.* 1996).

Si, Ca, Cr, and Fe abundances in the atmospheres of normal and chemically peculiar B–F stars

Star HD	$T_{\rm eff}$, K	$\log(N/N_{\rm tot})$				References
		Si	Ca	Cr	Fe	
Normal main-sequence stars						
165908	6100	−4.86	−6.12	−6.56	−4.85	Adelman *et al.* (2000)
30810	6109	−4.51	−5.66		−4.62	Varenne and Monier (1999)
222368	6177	−4.11	−5.76	−6.30	−4.51	Adelman *et al.* (1997)
27383	6179	−4.42	−5.90		−4.50	Varenne and Monier (1999)
28363	6348	−4.54	−5.53		−4.58	Varenne and Monier (1999)
27991	6431	−4.46	−5.60		−4.55	Varenne and Monier (1999)
30869	6456	−4.50	−5.55		−4.60	Varenne and Monier (1999)
28406	6530	−4.45	−5.72		−4.65	Varenne and Monier (1999)
27848	6548	−4.37	−5.66		−4.55	Varenne and Monier (1999)
31845	6631	−4.39	−5.70		−4.57	Varenne and Monier (1999)
28736	6646	−4.37	−5.63		−4.54	Varenne and Monier (1999)
27534	6675	−4.40	−5.77		−4.64	Varenne and Monier (1999)
18404	6680	−4.38	−5.63		−4.55	Varenne and Monier (1999)
27561	6681	−4.44	−5.79		−4.65	Varenne and Monier (1999)
26345	6690	−4.37	−5.65		−4.55	Varenne and Monier (1999)
61421	6696	−4.46	−5.73		−4.56	Varenne and Monier (1999)
28911	6710	−4.40	−5.70		−4.61	Varenne and Monier (1999)
128167	6744	−4.73	−5.65	−6.60	−4.89	Adelman *et al.* (1997)
185395	6810	−4.23	−6.05	−6.20	−4.40	Adelman *et al.* (1997)
26015	6828	−4.40	−5.71		−4.60	Varenne and Monier (1999)
26462	6874	−4.53	−5.76		−4.72	Varenne and Monier (1999)
37954	7170	−4.75	−5.89	−6.68	−4.88	Bikmaev *et al.* (2002)
32115	7250	−4.53	−5.63	−6.33	−4.54	Bikmaev *et al.* (2002)
27819	8189	−4.42	−5.67		−4.60	Varenne and Monier (1999)
60825	9000	−4.41	−5.62	−6.21	−4.46	Adelman and Davis Philip (1996)
89021	9000	−4.36	−5.57	−5.81	−4.31	Adelman (1999)
1280	9000		−5.32	−6.10	−4.22	Kocer *et al.* (2003)
198001	9050	−4.42	−6.14	−6.33	−4.60	Kocer *et al.* (2003)
14252	9260	−4.76	−5.75	−6.48	−4.54	Hill and Landstreet (1993)
154029	9325	−4.35	−5.22	−5.78	−4.12	Adelman (1999)
47105	9440	−4.43	−5.65	−6.25	−4.41	Hill and Landstreet (1993)
176437	9550	−4.45	−6.40	−6.48	−4.87	Adelman *et al.* (2001)
87887	9875	−4.63	−5.89	−6.32	−4.54	Pintado and Adelman (2003)
123299	10025	−4.94	−6.33	−6.30	−4.76	Adelman (1994)
85504	10135	−4.45	−5.13	−5.88	−4.33	Adelman and Davis Philip (1996)
193432	10250	−4.69	−5.55	−6.13	−4.52	Adelman (1991)
192907	10325	−4.61	−5.75	−6.22	−4.61	Adelman (1996)
185872	10750	−4.70	−6.11	−6.22	−4.58	Adelman (1999)
38899	10825	−4.51	−5.33	−6.41	−4.57	Adelman (1991)
222173	11600	−4.60	−6.14	−6.42	−4.68	Kocer *et al.* (2003)

Table. (Contd.)

Star HD	T_{eff}, K	$\log(N/N_{\text{tot}})$				References
		Si	Ca	Cr	Fe	
155763	12500	−4.48	−5.82	−6.67	−4.69	Adelman (1998)
179761	12900	−4.40	−5.66	−6.64	−4.80	Adelman (1991)
17081	13150	−4.52	−5.72	−6.54	−4.62	Adelman (1991)
197392	13306	−5.00	−5.45	−6.58	−4.66	Adelman *et al.* (2001)
195810	13679	−4.41	−5.73	−6.19	−4.52	Kocer *et al.* (2003)
14051	14051	−4.57	−6.24	−6.52	−4.76	Pintado and Adelman (2003)
188892	14156	−4.64	−5.37	−6.87	−4.85	Adelman (1998)
138764	14230	−4.56	−5.20	−6.58	−4.55	Adelman and Davis Philip (1994)
41692	14330	−4.29		−6.58	−4.58	Adelman and Davis Philip (1996)
28114	14690	−4.47		−6.63	−4.89	Adelman and Davis Philip (1996)
147394	15000	−4.46	−5.74	−6.55	−4.67	Adelman *et al.* (2001)
Am stars						
27628	7321		−6.28		−4.42	Varenne and Monier (1999)
33204	7646	−4.40	−5.91		−4.35	Varenne and Monier (1999)
189849	7700	−4.63	−6.04	−6.42	−4.75	Adelman *et al.* (1997)
209625	7700	−4.60	−6.15	−6.12	−4.42	Adelman *et al.* (1997)
28546	7800	−4.43	−5.94		−4.36	Varenne and Monier (1999)
173648	8155	−4.69	−5.94	−6.02	−4.21	Adelman *et al.* (1999)
27962	9025	−4.45	−5.79	−5.70	−4.15	Adelman (1994)
182564	9125	−4.44	−5.57	−5.93	−4.20	Adelman (1996)
95608	9250	−4.54	−6.19	−5.90	−4.11	Adelman *et al.* (1999)
43378	9295	−4.87	−5.65	−6.38	−4.69	Caliskan and Adelman (1997)
97633	9450	−4.57	−5.82	−6.30	−4.45	Hill and Landstreet (1993)
58142	9500	−4.57	−6.04	−6.46	−4.66	Adelman (1994)
188728	9534	−4.34	−5.62	−5.82	−4.12	Caliskan and Adelman (1997)
95418	9600	−4.51	−5.77	−6.11	−4.33	Adelman (1996)
214994	9680	−4.50	−5.70	−6.16	−4.30	Hill and Landstreet (1993)
48915	9870	−4.35	−6.10	−5.89	−4.21	Hill and Landstreet (1993)
94334	10026	−4.58	−5.70	−6.20	−4.30	Caliskan and Adelman (1997)
147550	10100	−4.53	−5.96	−5.99	−4.39	Lopez-Garcia and Adelman (1994)
213320	10125	−4.58	−6.15	−6.21	−4.37	Adelman and Albayrak (1998)
196724	10200	−4.73	−6.16	−6.25	−4.52	Adelman and Albayrak (1998)
Nonpulsating AP stars						
115708	7510	−4.46		−5.75	−4.95	Ryabchikova *et al.* (2001)
75445	7700	−4.29	−5.68	−5.50	−4.44	Ryabchikova *et al.* (2004a)
29578	7800	−4.01	−5.11	−4.83	−3.98	Ryabchikova *et al.* (2004a)
62140	7900	−4.66		−4.60	−4.20	Ryabchikova *et al.* (2001)
116114	8000	−4.41	−5.22	−5.40	−4.19	Ryabchikova *et al.* (2004a)
137909	8000	−4.09	−5.10	−4.64	−3.80	Ryabchikova *et al.* (2004a)
18610	8100	−3.82	−5.18	−4.18	−3.83	Ryabchikova *et al.* (2004a)
204411	8400	−4.13	−5.17	−4.80	−4.04	Ryabchikova *et al.* (2005)

Table. (Contd.)

Star HD	$T_{\rm eff}$, K	$\log(N/N_{\rm tot})$				References
		Si	Ca	Cr	Fe	
188041	8500	−4.00	−4.82	−4.07	−3.80	Ryabchikova *et al.* (2004a)
108945	8800	−4.53	−6.50	−4.80	−4.00	Savanov *et al.* (1996)
110066	9000	−3.25	−5.03	−3.48	−3.10	Ryabchikova *et al.* (2004a)
212385	9200	−4.29	−4.60	−4.52	−3.77	Ryabchikova *et al.* (2004a)
133792	9200	−4.13	−6.10	−3.81	−3.24	Ryabchikova *et al.* (2004b)
66318	9200	−3.20	−6.40	−3.80	−3.05	Bagnulo *et al.* (2003)
153882	9250			−4.20	−3.13	Ryabchikova *et al.* (1995)
183806	10070	−3.90	−4.70	−4.07	−3.43	Ryabchikova *et al.* (2004a)
108662	10300	−5.45		−3.11	−3.02	Savanov *et al.* (1996)
116458	10300	−4.25		−4.64	−3.70	Nishimura *et al.* (2004)
40312	10450	−3.47		−3.90	−3.35	Van Rensbergen *et al.* (1984)
170973	10750	−3.82	−4.91	−4.80	−3.50	Lopez-Garcia *et al.* (2001)
192913	10900	−4.06	−5.33	−4.92	−3.36	Lopez-Garcia and Adelman (1999)
26385	11100	−3.29		−5.13	−3.95	Bolcal *et al.* (1991)
133029	11200	−3.36	−5.72	−4.15	−3.28	Lopez-Garcia and Adelman (1999)
43819	11300	−3.88	−5.12	−5.02	−3.57	Lopez-Garcia and Adelman (1994)
112413	11600	−4.12		−5.30	−3.60	Kochukhov *et al.* (2002)
10221	11900	−3.36		−4.43	−3.36	Glagolevskii *et al.* (2005)
22316	12000	−5.20		−4.98	−3.54	Nielsen and Wahlgren (2000)
25823	12750	−3.67		−4.98	−3.90	Bolkal *et al.* (1987)
37808	13100	−4.19	−5.68	−4.87	−3.47	Leone *et al.* (1993)
79158	13300	−4.20		−5.20	−3.50	Wade *et al.* (2005)
5737	13900	−4.07		−5.58	−4.00	Lopez-Garcia *et al.* (2001)
168733	14000	−4.19		−5.20	−3.29	Ryabchikova *et al.* (2004a)
Pulsating roAp stars						
213637	6400	−4.85	−6.14	−6.60	−5.37	Kochukhov (2003)
101065	6600	−4.38	−6.67	−6.12	−5.34	Cowley *et al.* (2000)
217522	6750	−4.27	−6.14	−6.54	−5.64	Gelbmann (1998)
122970	6930	−4.45	−5.48	−6.03	−4.47	Ryabchikova *et al.* (2000)
24712	7250	−4.43	−5.69	−5.82	−5.00	Ryabchikova *et al.* (1997a)
203932	7450	−4.39	−5.17	−5.64	−4.42	Gelbmann *et al.* (1997)
176232	7550	−4.19	−5.28	−5.10	−4.18	Ryabchikova *et al.* (2000)
137949	7550	−4.24	−5.10	−5.29	−4.20	Ryabchikova *et al.* (2004a)
166473	7700	−4.10	−5.34	−5.43	−4.32	Gelbmann *et al.* (2000)
201601	7700	−4.42	−5.40	−5.55	−4.30	Ryabchikova *et al.* (1997b)
12098	7800	−4.50	−5.20	−5.20	−4.25	Ryabchikova *et al.* (2004a)
128898	7900	−4.20	−5.15	−5.74	−4.50	Kupka *et al.* (1996)
60435	8100	−4.13	−5.12	−5.12	−4.30	Ryabchikova *et al.* (2004a)
42659	8100	−4.90	−5.60	−5.20	−4.60	Ryabchikova *et al.* (2001)

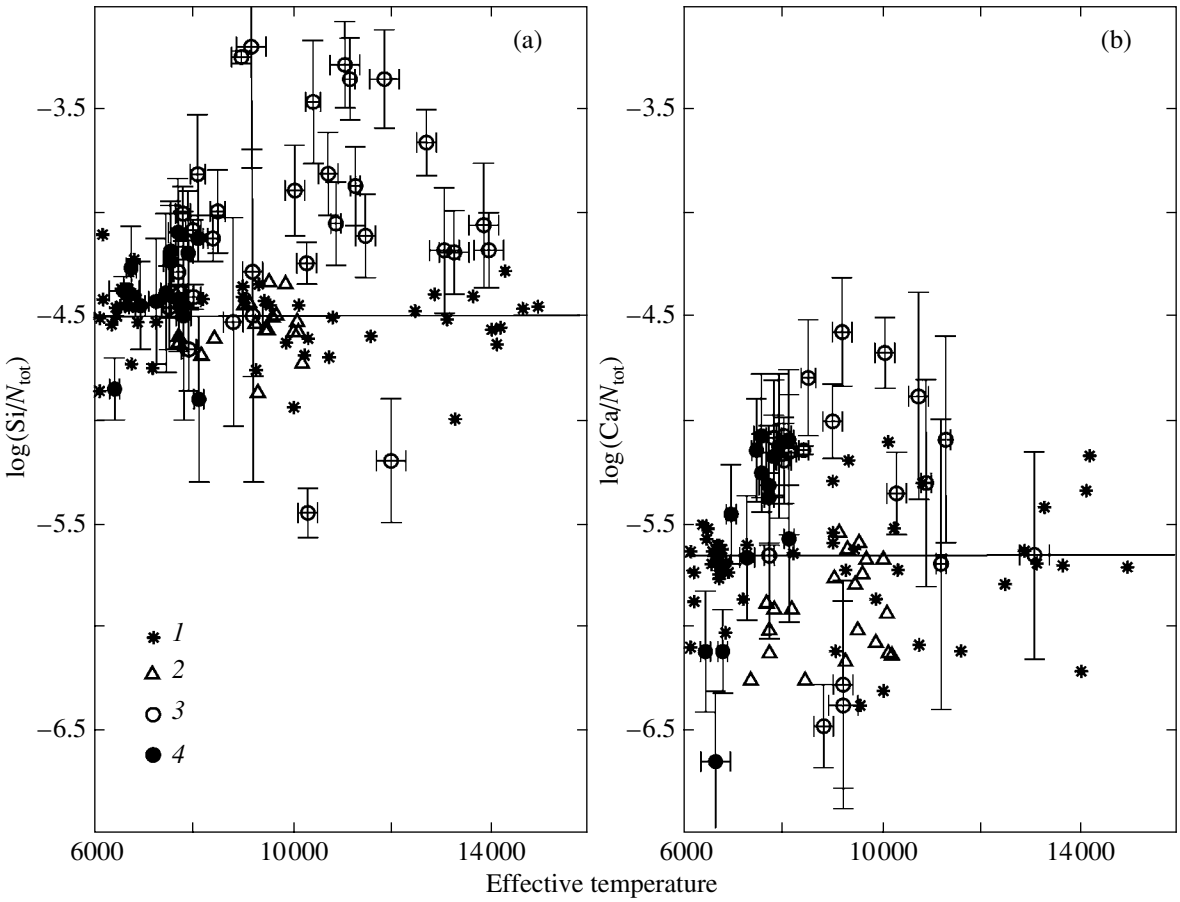

Fig. 1. Si (a) and Ca (b) abundances versus effective temperature for normal stars (*1*), Am stars (*2*), Ap stars (*3*), and roAp stars (*4*). The horizontal lines indicate the solar abundances of these elements.

For normal and metallic-line stars, the Si abundances tightly cluster around the solar value with a mean and a dispersion of -4.51 ± 0.16 and without any temperature correlation.

Calcium is underabundant in most Am stars and, on average, has a solar abundance in normal stars, although the scatter is larger than that for Si (-5.72 ± 0.27). This may be attributable in part to the lines that were used to derive the abundances. These are Ca I lines in cooler stars, while the abundance in hotter stars is derived from the single resonance Ca II 3933 Å line, which may be subject to non-LTE effects. In Ap stars, the Ca abundance increases with temperature, with the maximum near 10 000 K and with the subsequent decline to the solar value. However, several stars drop out of this dependence, with the deviations being not due to abundance errors. These cases are discussed in the next section.

The temperature behavior of the Cr and Fe abundances shown in Fig. 2 is most impressive. The abundances of these elements in the atmospheres of Ap stars increase rapidly as the temperature rises from 6000 to 9000–10 000 K; subsequently, the Cr abundance decreases to values that exceed the solar abundance by an order of magnitude, while the Fe abundance remains enhanced by approximately +1.0 dex compared to the solar value. At maximum, the Cr and Fe abundances are almost the same; as a result, the peculiar stars were classified as Cr or SiCr stars in this temperature range. It should be noted that, whereas Fe could be underabundant in the coolest Ap stars (roAp stars), with the underabundance reaching an order of magnitude in the most extreme cases, the Cr abundance is nearly solar for these stars. The rate of increase of the Cr abundance with temperature is a factor of 1.5 higher than that for Fe. The behavior of the abundances of these elements in the atmospheres of normal and Am stars is of particular interest. The temperature dependence exhibits a maximum near the same effective temperatures as those for peculiar stars, with the only difference that this maximum is lower by several orders of magnitude. Hot normal stars have Cr and Fe abundances below their solar values.

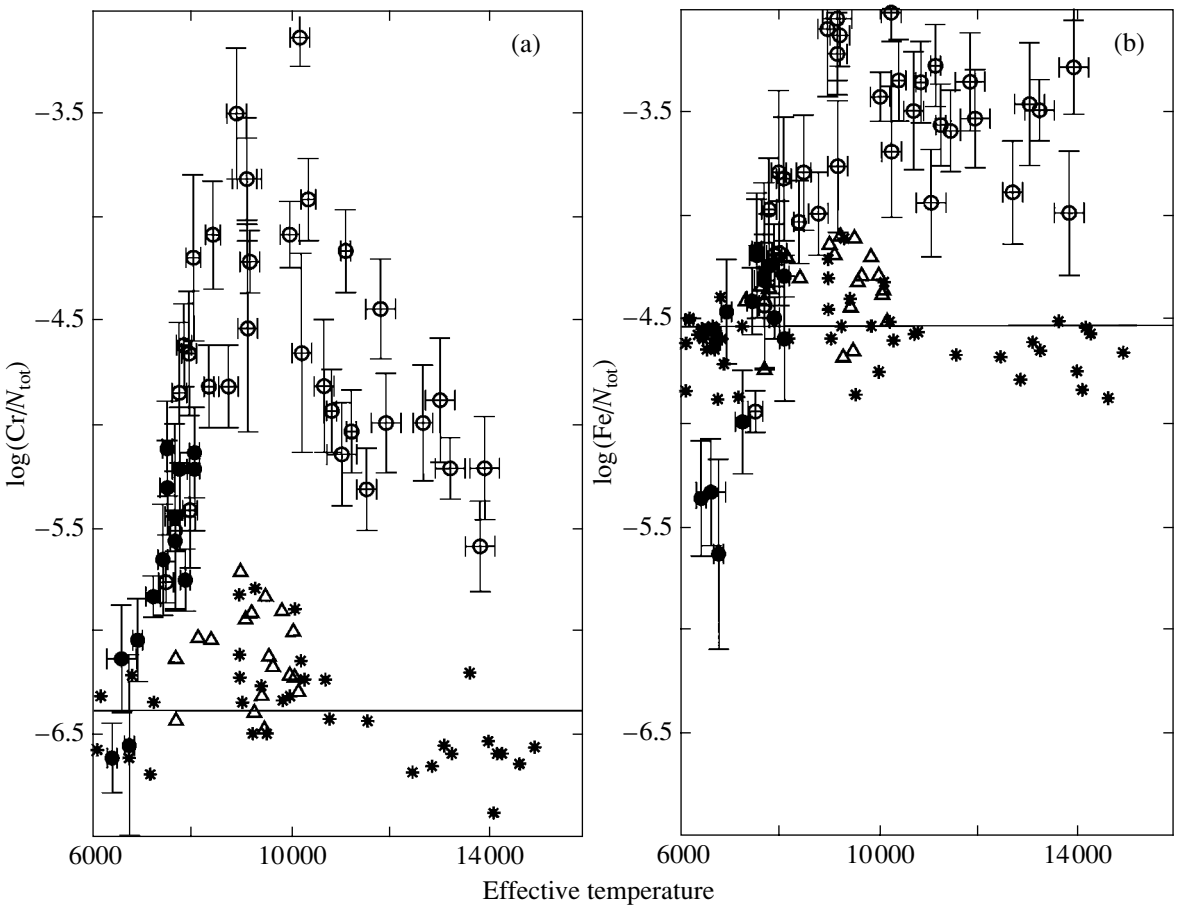

Fig. 2. Same as Fig. 1 for the Cr (a) and Fe (b) abundances.

COMPARISON WITH PREDICTIONS OF THE DIFFUSION THEORY

According to the diffusion calculations by Michaud *et al.* (1976) and LeBlanc (private communication), silicon must have a nearly solar abundance in the temperature range 6000–9500 K, with a possible small underabundance. In Ap stars, a silicon overabundance is almost always observed at temperatures above 8300 K.

In general, we can say that, although the temperature behavior of the Ca abundance corresponds to predictions of the diffusion theory (the abundance increases with $T_{\rm eff}$ in the range 6000–9500 K), the observed abundance itself is higher than that predicted by the theory, according to which Ca must remain underabundant. The causes of the increase in Ca abundance are considered below.

The above temperature dependences of the Cr and Fe abundances in peculiar stars up to the maximum are in excellent agreement with predictions of previous diffusion calculations (Michaud *et al.* 1976) and those performed by computing the radiation spectrum in detail (LeBlanc, private communication). An extension of these calculations to the higher temperatures and a comparison with observations will give a complete picture of the formation of chemical anomalies in the atmospheres of magnetic peculiar stars.

Let us consider the processes that weaken or strengthen the diffusion separation of elements in stellar atmospheres.

The Influence of Turbulence

It was shown in the previous section that the temperature dependence of the atmospheric abundances of the main elements, Cr and Fe, for normal and Am stars is similar in shape to that for Ap stars, but has a much smaller scale. In principle, diffusion must take place in the radiative atmospheres of any stars, but the typical rates of this process are very low, and any turbulent motions destroy stratification, creating a homogeneous medium. The weaker the turbulence, the more favorable the conditions in stellar atmospheres for the diffusion separation of elements. The microturbulence is zero in all Ap stars (not to be

confused with the broadening due to magnetic intensification), while in normal and Am stars it is from 1.5 to 5 km s^{-1} in the range of effective temperatures 6000–10 000 K. Clearly, this enhanced microturbulence is a factor that inhibits the diffusion of Cr and Fe in normal and Am stars at these temperatures. However, the microturbulence disappears in normal stars at higher temperatures, but we observe no Cr and Fe overabundances characteristic of hot Ap stars. In the latter, the magnetic field probably plays an important role in the diffusion process.

The Magnetic Field

The main role of the magnetic field is generally believed to be the stabilization of the atmosphere. However, the magnetic field can influence the diffusion of elements directly. First, the diffusion of ions changes when they move across the magnetic field, and this difference in the diffusion of neutral particles and ions is regarded as the main formation mechanism of the surface abundance inhomogeneities observed in most Ap stars (Michaud *et al.* 1981). Second, the Zeeman splitting of spectral lines changes the distribution of the energy flux, causing the radiative acceleration to change (usually to increase) (Alecian and Stift 2004). These effects have not yet been included in the diffusion calculations, but certain conclusions about the role of the magnetic field can be reached by comparing the elemental abundances in stars with equal temperatures, but with greatly differing magnetic fields. As an example, let us consider three stars: HD 110066 ($T_{\rm eff} = 9000$ K, $B_{\rm s} = 3.6$ kG), HD 133092 ($T_{\rm eff} = 9200$ K, $B_{\rm s} \approx 1$ kG), and HD 66318 ($T_{\rm eff} = 9200$ K, $B_{\rm s} = 14.5$ kG), where $B_{\rm s}$ is the mean magnitude of the surface magnetic field taken from the corresponding papers listed in the table. The Cr and Fe abundances in these stars are identical, within the error limits, suggesting a negligible influence of the magnetic field on the diffusion of these elements at a given temperature. The dependences constructed for Ap stars with different magnetic field strengths (Fig. 2) confirm the conclusion that the temperature has a predominant effect on the diffusion of Cr and Fe in the range 6000–9500 K.

The Si abundance in the stars with 3.6 and 14.5 kG fields is much higher than that in the star with a weak magnetic field, in qualitative agreement with the Si diffusion calculations (Vauclair *et al.* 1979). The latter predict that stars without a magnetic field or with weak radial fields must have a solar Si abundance (HD 133092), while the Si overabundance in stars with strong horizontal magnetic field components (HD 110066 and HD 66318) can reach two orders of magnitude. Note, however, that Vauclair *et al.* (1979) carried out their calculations for hotter stars, with $T_{\rm eff} \geq 12\,000$ K.

The Stellar Wind

These three stars exhibit a different abundance pattern for Ca, which has the same significant underabundance in HD 133092 and HD 66318 and an overabundance of the same order of magnitude in HD 110066. As was first shown by Babel (1992) and subsequently confirmed by LeBlanc's more detailed calculations (private communication), the Ca diffusion produces a distribution in a quiet atmosphere that corresponds to the abundances $\log({\rm Ca}/{\rm N_{tot}}) \sim$ from −6.0 to −6.2 observed in HD 133092 and HD 66318. Including a stellar wind with a rate of $\sim (2–4) \times 10^{-15} M_\odot$ yr^{-1} affects significantly the depth distribution of Ca, increasing its abundance at the maximum of the distribution by an order of magnitude or more (see Fig. 3 in Babel's paper), which results in a solar Ca abundance or even overabundance. Different moderate mass loss rates by the stars can be assumed to be responsible for the appearance of overabundances and Ca abundance variations in the atmospheres of Ap stars.

CONCLUSIONS

The observed temperature dependences of the Cr and Fe abundances in the atmospheres of magnetic peculiar stars begin with a solar Cr abundance and an order-of-magnitude Fe underabundance at $T_{\rm eff} \sim$ 6500 K and show a maximum near $T_{\rm eff} \sim 9500$ K. The abundances of both elements at the maximum are almost equal ($\log({\rm Fe}/N_{\rm tot}) \sim -3.3$), although the solar abundances of these elements differ by almost two orders of magnitude. As the temperature increases further, the Cr abundance decreases, while the Fe abundance remains approximately at a constant level corresponding to a +1.0-dex overabundance. The observed dependences in the range 6000–9500 K can be satisfactorily described in terms of the element diffusion under the combined action of gravitational settling and radiative acceleration. The temperature dependences of the abundances of these elements in the atmospheres of normal and Am stars are similar in shape, but have a maximum that is several orders of magnitude lower than that observed in Ap stars. It may well be that the diffusion process also takes place in the atmospheres of normal stars, but its efficiency is very low due to the presence of microturbulence. We showed that in the range of effective temperatures 6000–9500 K, the magnetic field had virtually no effect on the diffusion of Cr and Fe in Ap stars.

The Si and Ca abundances can also be explained in terms of the diffusion model. The diffusion of Si ions in the magnetic field can produce the observed Si overabundances. The Ca overabundances that cannot be produced in terms of the simple model of the element diffusion separation can be explained

by the presence of a stellar wind. Different mass-loss rates within the range $(2–4) \times 10^{-15} M_\odot$ yr^{-1} can account for the Ca-abundance variations in the atmospheres of Ap stars.

ACKNOWLEDGMENTS

This work was supported in part by the Russian Foundation for Basic Research (project no. 03-02-16342), the Nonstationary Processes in Astrophysics program of the Presidium of the Russian Academy of Sciences, and a Grant for the Support of Leading Scientific Schools (NSh-162.2003.2).

REFERENCES

1. S. J. Adelman, Mon. Not. R. Astron. Soc. **252**, 116 (1991).
2. S. J. Adelman, Mon. Not. R. Astron. Soc. **271**, 355 (1994).
3. S. J. Adelman, Mon. Not. R. Astron. Soc. **280**, 130 (1996).
4. S. J. Adelman, Mon. Not. R. Astron. Soc. **296**, 856 (1998).
5. S. J. Adelman, Mon. Not. R. Astron. Soc. **310**, 146 (1999).
6. S. J. Adelman and B. Albayrak, Mon. Not. R. Astron. Soc. **300**, 359 (1998).
7. S. J. Adelman, H. Caliskan, D. Kocer, and C. Bolcal, Mon. Not. R. Astron. Soc. **288**, 470 (1997).
8. S. J. Adelman, H. Caliskan, T. Cay, *et al.*, Mon. Not. R. Astron. Soc. **305**, 391 (1999).
9. S. J. Adelman, H. Caliskan, D. Kocer, *et al.*, Mon. Not. R. Astron. Soc. **316**, 514 (2000).
10. S. J. Adelman, H. Caliskan, D. Kocer, *et al.*, Astron. Astrophys. **371**, 1078 (2001).
11. S. J. Adelman and A. G. Davis Philip, Publ. Astron. Soc. Pac. **106**, 1239 (1994).
12. S. J. Adelman and A. G. Davis Philip, Mon. Not. R. Astron. Soc. **282**, 1181 (1996).
13. G. Alecian and M. J. Stift, Astron. Astrophys. **416**, 703 (2004).
14. R. Aurière, J. Silvester, G. A. Wade, *et al.*, in *Magnetic Stars, Proceedings Int. Conf.*, Ed. by Yu. V. Glagolevskij, D. O. Kudryavtsev, and I. I. Romanyuk (Nizhnii Arkhyz, 2005), p. 114 (Spec. Astrophys. Obs., 2005) (in press).
15. H. W. Babcock, Astrophys. J. **132**, 521 (1960).
16. J. Babel, Astron. Astrophys. **258**, 449 (1992).
17. S. Bagnulo, J. D. Landstreet, G. Lo Curto, *et al.*, Astron. Astrophys. **645**, 167 (2003).
18. I. F. Bikmaev, T. A. Ryabchikova, H. Bruntt, *et al.*, Astron. Astrophys. **389**, 537 (2002).
19. C. Bolcal, D. Kocer, and A. Duzgelen, Astrophys. Space Sci. **139**, 295 (1987).
20. C. Bolcal, D. Kocer, T. Koktay, and T. Gžel, Astrophys. Space Sci. **185**, 237 (1991).
21. H. Caliskan and S. J. Adelman, Mon. Not. R. Astron. Soc. **288**, 501 (1997).
22. C. R. Cowley, T. Ryabchikova, F. Kupka, *et al.*, Mon. Not. R. Astron. Soc. **317**, 299 (2000).
23. M. Gelbmann, Contrib. Astron. Obs. Scalnaté Pleso **27**, 280 (1998).
24. M. Gelbmann, F. Kupka, W. W. Weiss, and G. Mathys, Astron. Astrophys. **319**, 630 (1997).
25. M. Gelbmann, T. A. Ryabchikova, W. W. Weiss, *et al.*, Astron. Astrophys. **356**, 200 (2000).
26. Yu. V. Glagolevskiĭ, T. A. Ryabchikova, and G. A. Chuntonov, Pis'ma Astron. Zh. **31**, 363 (2005).
27. G. M. Hill and J. D. Landstreet, Astron. Astrophys. **276**, 142 (1993).
28. D. Kocer, S. J. Adelman, H. Caliskan, *et al.*, Astron. Astrophys. **406**, 975 (2003).
29. O. Kochukhov, Astron. Astrophys. **404**, 669 (2003).
30. O. Kochukhov, N. Piskunov, I. Ilyin, *et al.*, Astron. Astrophys. **389**, 420 (2002).
31. F. Kupka, N. Piskunov, T. A. Ryabchikova, *et al.*, Astron. Astrophys., Suppl. Ser. **138**, 119 (1999).
32. F. Kupka, T. A. Ryabchikova, W. W. Weiss, *et al.*, Astron. Astrophys. **308**, 885 (1996).
33. R. L. Kurucz, CD-ROM No. 18–23 (Smithsonian Astrophysical Observatory, Cambridge, 1993).
34. F. LeBlanc and D. Monin, *IAU Symp. No. 224: A-Star Puzzle,* Ed. by J. Zverko, W. W. Weiss, J. Žižňovský, and S. J. Adelman (Cambridge Univ. Press, Cambridge, 2004), p. 193.
35. F. Leone, F. A. Catalano, and M. Manfré, Astron. Astrophys. **279**, 167 (1993).
36. Z. Lopez-Garcia and S. J. Adelman, Astron. Astrophys., Suppl. Ser. **107**, 353 (1994).
37. Z. Lopez-Garcia and S. J. Adelman, Astron. Astrophys., Suppl. Ser. **137**, 227 (1999).
38. Z. Lopez-Garcia, S. J. Adelman, and O. I. Pintado, Astron. Astrophys. **367**, 859 (2001).
39. G. Michaud, Astrophys. J. **160**, 641 (1970).
40. G. Michaud, I. Charland, S. Vauclair, and G. Vauclair, Astrophys. J. **210**, 447 (1976).
41. G. Michaud, C. Mégessier, and I. Charland, Astron. Astrophys. **103**, 244 (1981).
42. K. Nielsen and G. M. Wahlgren, Astron. Astrophys. **356**, 146 (2000).
43. M. Nishimura, K. Sadakane, K. Kato, *et al.*, Astron. Astrophys. **420**, 673 (2004).
44. O. I. Pintado and S. J. Adelman, Astron. Astrophys. **406**, 987 (2003).
45. T. A. Ryabchikova, S. J. Adelman, W. W. Weiss, and R. Kuschnig, Astron. Astrophys. **322**, 234 (1997a).
46. T. Ryabchikova, R. Kuschnig, N. E. Piskunov, and V. Pavlova, in *Stellar Surface Structure, Poster Proceedings of Symposium 176*, Ed. by K. G. Strassmeier (Wien, 1995), p. 132.
47. T. A. Ryabchikova, J. D. Landstreet, M. J. Gelbmann, *et al.*, Astron. Astrophys. **327**, 137 (1997b).
48. T. Ryabchikova, F. Leone, and O. Kochukhov, Astron. Astrophys. (2005) (in press).

49. T. Ryabchikova, F. Leone, O. Kochukhov, and S. Bagnulo, *IAU Symp. No. 224: The A-Star Puzzle,* Ed. by J. Zverko, W. W. Weiss, J. Žižňovský, and S. J. Adelman (Cambridge Univ. Press, Cambridge, on-line publication, 2005).
50. T. Ryabchikova, N. Nesvacil, W. W. Weiss, *et al.*, Astron. Astrophys. **423**, 705 (2004).
51. T. A. Ryabchikova, N. Piskunov, H. C. Stempels, *et al.*, Phys. Scr., T **83**, 1962 (1999).
52. T. A. Ryabchikova, I. S. Savanov, A. P. Hatzes, *et al.*, Astron. Astrophys. **357**, 981 (2000).
53. T. A. Ryabchikova, I. S. Savanov, V. P. Malanushenko, and D. O. Kudryavtsev, Astron. Zh. **78**, 444 (2001) [Astron. Rep. **45**, 382 (2001)].
54. I. S. Savanov, T. A. Ryabchikov, and E. S. Davydova, Pis'ma Astron. Zh. **22**, 910 (1996) [Astron. Lett. **22**, 814 (1996)].
55. W. Van Rensbergen, H. Hensberge, and S. J. Adelman, Astron. Astrophys. **136**, 31 (1984).
56. O. Varenne and R. Monier, Astron. Astrophys. **351**, 247 (1999).
57. S. Vauclair, J. Hardorp, and D. M. Peterson, Astrophys. J. **227**, 526 (1979).
58. G. A. Wade, M. Smith, D. A. Bohlender, *et al.*, Astron. Astrophys. (2005) (in press).

Translated by N. Samus'

Astronomy Letters, Vol. 31, No. 6, 2005, pp. 398–405. Translated from Pis'ma v Astronomicheskiĭ Zhurnal, Vol. 31, No. 6, 2005, pp. 447–455.

Magnetic Configurations of Streamer Structures in the Solar Atmosphere

S. L. Koutchmy[1] and M. M. Molodensky[2*]

[1] *Astrophysical Institute, Paris, France*

[2] *Institute of Terrestrial Magnetism, Ionosphere, and Radio Wave Propagation, Russian Academy of Sciences, Troitsk, Moscow oblast, 142190 Russia*

Received August 4, 2004

Abstract—We consider two types of streamer structures observed in the solar atmosphere. Structures of the first type are medium-scale configurations with scale lengths comparable to the scale height in the corona, $kT/mg = 100$ thousand km, which appear as characteristic plasma structures in the shape of a dome surrounding the active region with thin streamers emanating from its top. In configurations of this type, gravity plays no decisive role in the mass distribution. The plasma density is constant on magnetic surfaces. Accordingly, the structure of the configurations is defined by the condition $\psi = \text{const}$, where ψ is the flux function of the magnetic field. Structures of the second type are large-scale configurations (coronal helmets, loops, and streamers), which differ from the above structures in that their scale lengths exceed the scale height in the corona. For them, gravity plays a decisive role; as a result, instead of the magnetic surfaces, the determining surface is $\mathbf{B}\text{grad}\Phi = 0$. We constructed three-dimensional images of these structures. Some of the spatial curves called "visible contours" of the $B_r = 0$ surface are shown to be brightest in the corona. We assume that the helmet boundaries and polar plumes are such curves.

Key words: *Sun, solar atmosphere, magnetic field.*

INTRODUCTION

X-ray observations of the solar corona raise a number of questions that have received no unequivocal theoretical interpretation. These include the origin of the characteristic plasma structures above active regions in the shape of a dome surrounding the active region with thin streamers emanating from its top.

The model of an axisymmetric plasma configuration, which satisfies the MHD equilibrium and plasma stability conditions, gives an answer to a number of raised questions. The neighborhood of the separatrix magnetic surface with a saddle singular point on the symmetry axis satisfies the stability condition. This surface is perceived by the observer as a visible dome-shaped surface with a streamer above the active region emanating from it.

The required magnetic configuration can be formed through a superposition of the counter magnetic fields of a sunspot and its surrounding facula with an opposite field. The simplest configuration of the currents needed to construct the suggested model is the axisymmetric configuration of two coaxial ring currents. In a more general case, the equilibrium is described by the Grad–Shafranov equation (see Landau and Lifshitz 1982), whose simplest solutions also yield the required configurations.

Large-scale configurations (coronal helmets, loops, and streamers), which differ in that their scale lengths exceed the scale height in the corona (~100 thousand km), are structures of another type. Just as the Lorentz force in prominences extends the chromospheric scale height (~1.5 thousand km), the same is also true in the structures considered below.

MAGNETIC STREAMER CONFIGURATIONS

Figure 1a illustrates the coronal structure above an active region during the September 11, 1968 solar eclipse (Koutchmy 1972) observed through a radial filter. In the subsequent analysis, the effect of gravity is assumed to be negligible; in the first approximation, this corresponds to the compensation of the plasma density gradient by radial filters.

In Fig. 1a, straight streamers are observed above the dome-shaped coronal condensation (see Koutchmy 1972). Figure 1b shows the YOHKOH images (Shibata *et al.* 1992) obtained during the observations of the active region NOAA 6918. We see that a region similar in shape to a hemisphere lies at the base

* E-mail: moloden@izmiran.ru

of the streamer, while the streamer emerging near its top has a fine structure.

Koutchmy *et al.* (1995) suggested an axisymmetric magnetic configuration produced by two turns with oppositely directed currents located in the plane of the photosphere ($z = 0$) as a model of such a structure in the solar atmosphere. The magnetic surface structures obtained in this way have the characteristic shape of hemispheres with a sharpening at the top and with a bundle of thin streamers emanating from the top. The surface of the hemisphere is the separatrix magnetic surface, while the sharpening is a singular point. Such magnetic configurations are formed by a vortex-free magnetic field, since the currents that produce them are localized in the $z = 0$ plane.

The flux function $\psi = rA_\phi(r, z)$ that describes the magnetic field of a system of two rings with radii a and R and currents I_a and I_R is

$$\psi = \frac{4RI_R}{c}\left[G(r,z) - \frac{aI_a}{RI_R}G_a(r,z)\right], \qquad (1)$$

where

$$G_x(r,z) = \frac{1}{k_x}\sqrt{\frac{r}{x}}\left[(1-\frac{k_x^2}{2})K(k_x) - E(k_x)\right],$$
$$k_x^2 = \frac{4xr}{(x+r)^2+z^2},$$

r, ϕ, z are the cylindrical coordinates, $E(k)$ and $K(k)$ are the complete elliptic integrals.

The meridional sections of the magnetic surfaces (1) have a singular point on the z axis if the magnetic field vanishes on it. The coordinate z_s of this point is given by the relation

$$\frac{r_s^2}{R^2} = \frac{(a/R)^2}{\lambda/3} - a^2R^2 - (a/R)^{2\lambda/3} \qquad (2)$$
$$= \frac{(m_a/m_R)^{2/3-a^2/R^2}}{1-(m_a/m_R)^{2/3}}.$$

Here, $m_a/m_R = (a/R)^\lambda$ is the ratio of the magnetic moments of the current rings, $m_a/m_R = a^2I^2/R^2I_R$, and λ is a parameter ($0 < \lambda < 3$).

Figure 2a shows the configurations for various ratios m_a/m_R. We see that these structures are similar to those in Figs. 1a and 1b. In addition, Fig. 2b shows the computed two-dimensional configuration, $\partial/\partial y \equiv 0$, for which

$$\psi = \frac{2}{c}\sum_i I_i\Big[\ln\sqrt{(x-x_{i1})^2+(z-z_{i1})^2} \qquad (3)$$
$$-\ln\sqrt{(x-x_{i2})^2+(z-z_{i2})^2}\Big],$$

where (x_{i1}, z_{i1}) and (x_{i2}, z_{i2}) are the coordinates of the ith pair of linear currents lying below the $z = 0$ plane (i.e., beneath the photosphere). This structure is similar to that in Fig. 1a.

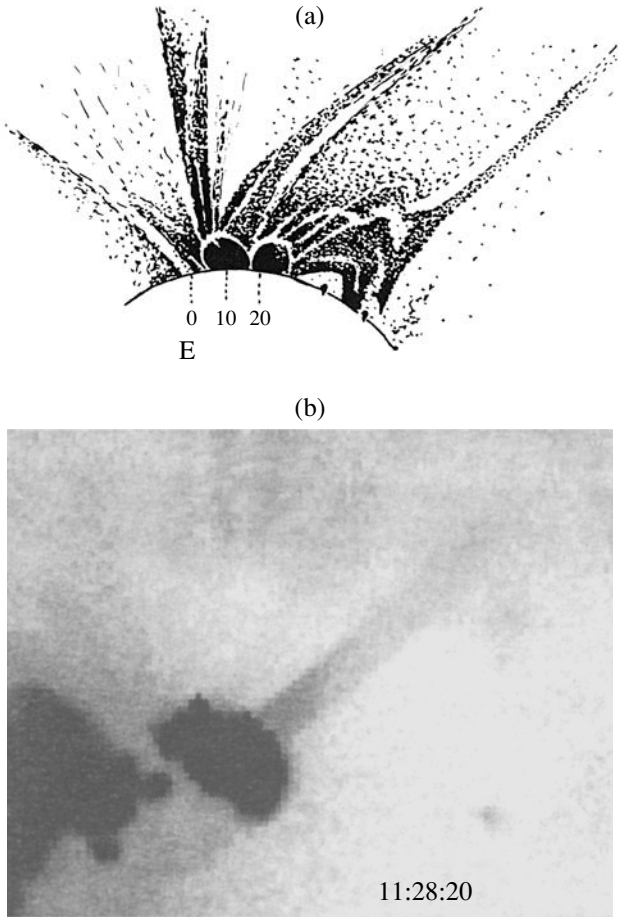

Fig. 1. (a) White-light and (b) X-ray streamer structures.

SURFACE CURRENT IN THE CORONA

Let us now solve the equilibrium equations by taking into account the radial dependence of the gravity and sheet parameters. Subsequently, having obtained the required solution, we consider the simplest shapes of the $B_r = 0$ surface that arise under the action of local field sources.

Molodensky (1993) considered the solution of the equilibrium equations that depended on two parameters and represented a plasma sheet in magnetic and gravitational fields. In the axisymmetric case, the poloidal flux function of the magnetic field was assumed to be

$$\psi = \tau + \frac{M\sin^2\theta}{r}, \quad \tau = -\frac{q}{k}\ln\cosh x, \quad x = k\cos\theta, \qquad (4)$$

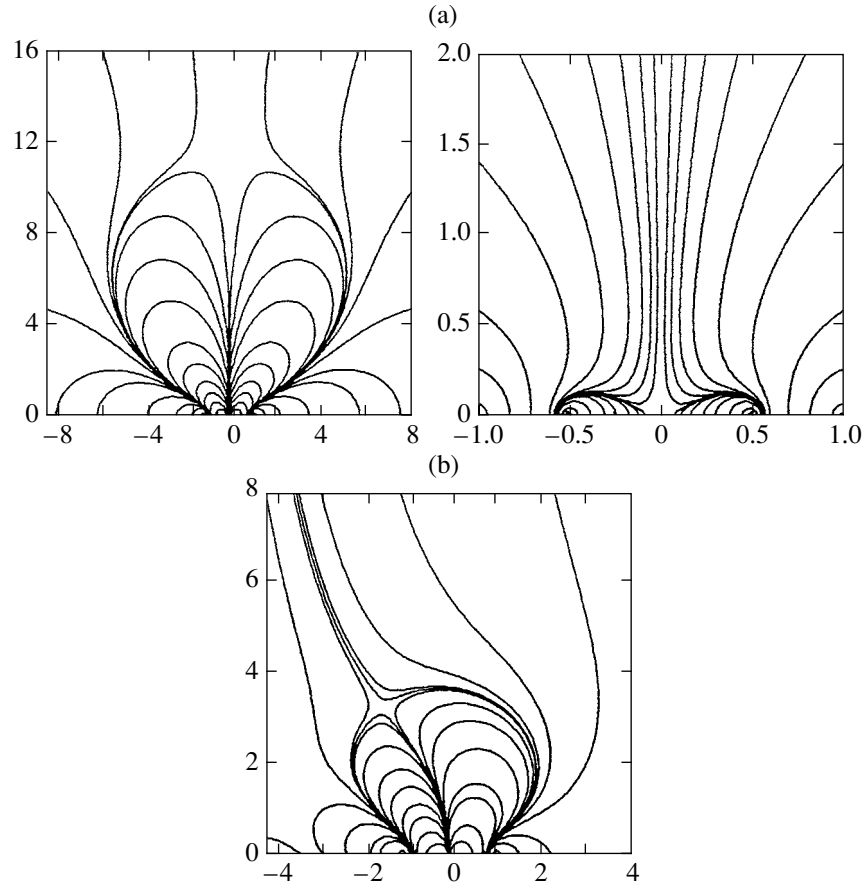

Fig. 2. Magnetic surface configurations for various models of streamer structures: (a) axisymmetric configurations and (b) configurations with a translational symmetry.

where M is the dipole moment of the configuration, q and k are the constants that can take on various values, and r, θ, φ are the spherical coordinates.

Note the following: The equilibrium equation relates the pressure to the function $\tau(\theta)$. We can imagine the case where $p(r, \theta)$ is a known function. The θ component of the equilibrium equation then serves to find the function $\tau(\theta)$.

In this case, we have a nonlinear ordinary differential equation of the first order for $\tau(\theta)$ that can be reduced in several cases to the Clairaut equation (see Kamke 1951). However, the situation is different in the case under consideration: we only know that the function $p(\theta)$ is nonzero in a small (or infinitesimal) θ interval near $\theta = \pi/2$ and know virtually nothing about the pressure distribution in sheet thickness. Under these conditions, $\tau(\theta)$ can be specified as such a function that $p(\theta)$ satisfies the above conditions.

The magnetic field and the current can be determined from (4):

$$B_r = \frac{1}{r^2 \sin\theta}\frac{\partial\psi}{\partial\theta}, \quad B_\theta = -\frac{1}{r\sin\theta}\frac{\partial\psi}{\partial r}, \quad B_\phi = 0, \tag{5}$$

or

$$B_r = q\frac{\tanh x}{r^2} + \frac{2M\cos\theta}{r^3}, \quad B_\theta = \frac{M\sin\theta}{r^3}, \tag{6}$$

$$j = j_\varphi = \frac{c}{4\pi}\frac{qk\sin\theta}{r^3\cosh^2 x}. \tag{7}$$

Expressions (6) for $r = \text{const}$ correspond to the Kippenhahn–Schluter prominence model; for this reason, we chose ψ in form (4). We see from (4)–(7) that a plasma sheet with a magnetic field has a thickness of $\sim 1/k$, and this thickness is small when $k \to \infty$. In this case, the above expressions can be simplified. Indeed, $\lim_{k\to\infty} \ln(\cosh(k\cos\theta)) \to |k\cos\theta|$ and, since

$$\frac{d}{dx}|x| = -\Theta(x), \tag{8}$$

where the known theta-function

$$\Theta(x) = \begin{cases} -1 \text{ for } x < 0 \\ 1 \text{ for } x > 0, \end{cases}$$

it follows from (5) and (8) that

$$B_r = \frac{q}{r^2}\Theta(x) + \frac{2M\cos\theta}{r^3}, \qquad (9)$$

and the current j_φ can be written as

$$\frac{4\pi}{c} j_\varphi = \frac{2q}{r^3} k\delta(x)\sin\theta\,. \qquad (10)$$

The function $\delta(x)$ appeared after the differentiation of $\Theta(x)$ in (9). The θ and r components of the equilibrium equation are

$$\frac{\partial p}{\partial\theta} - j_\varphi \frac{r}{c} B_r = 0, \qquad \frac{\partial p}{\partial r} + \frac{j_\varphi}{c} B_\theta + \rho\frac{\partial\Phi}{\partial r}, \quad (11)$$

where Φ is the gravitational potential, $\dfrac{\partial\Phi}{\partial r} = g_\odot \dfrac{R_\odot^2}{r^2}$.

Let us substitute j_ϕ and B_r from (9) and (10) into the first equation in (11):

$$\frac{\partial p}{\partial\theta} - \frac{1}{2\pi}\frac{qk}{r^2}\delta(x) \qquad (12)$$
$$\times \sin\theta\left(g\frac{\Theta(x)}{r^2} + 2M\frac{\cos\theta}{r^3}\right)dx = 0.$$

Since $\int x\delta(x) = 0$ and

$$\frac{d}{dx}\left[\frac{1}{2}\Theta^2\right] = 2\Theta(x)\delta(x), \qquad (13)$$

we obtain from (12)

$$p = p_0 + \frac{1}{8\pi}\frac{q^2}{r^4}(1 - \Theta^2(x)). \qquad (14)$$

Let us then substitute (14) into the second equation in (11) and consider the result as an equation defining ρ:

$$\rho = \frac{1}{g_\odot R_\odot^2} \qquad (15)$$
$$\times\left(-r^2\frac{\partial p_0}{\partial r} + \frac{q^2}{2\pi}\frac{1-\Theta^2}{r^3} - \frac{Mqk}{2\pi}\delta(x)\frac{\sin^2\theta}{r^4}\right).$$

Here, p_0 is the pressure in the absence of a magnetic field, and $\partial p_0/\partial r < 0$. Therefore, the first term in (15) is positive, the second term is proportional to $1 - \Theta^2(x)$, it is larger than or equal to zero, and the last term is also positive if $M_q < 0$. The latter condition is most stringent for a thin sheet. Configurations with $M_q < 0$ were considered by Molodensky (1993).

In particular, we see from Eq. (15) that the stretching action of the current rings for a thin sheet is negligible compared to the interaction of the current with the dipole field (for $k \sim 1$, both terms are of the same order of magnitude).

Let us consider the question of precisely what is observed in the heliospheric sheet. Clearly, the intensity of the radiation, i.e., the number of photons scattered in the corona is

$$I = \int \sigma I_0 n dl,$$

where σ is the Thomson photon scattering cross section, I_0 is the intensity of the photospheric radiation inside the light-scattering volume element of the corona, and n is the electron density. The integration is along the observer's line of sight. In the above approximation of a thin sheet, we can write

$$I = \sigma I_0 n \int dl = \sigma I_0 n \frac{d}{\cos\gamma},$$

where d is the sheet thickness, and γ is the angle between the line of sight and the normal to the sheet. Since the relative intensity distribution of the sheet radiation is of interest and since the result is usually compared with the observed distribution of radiation with a radial filter, the radius-dependent coefficient $\sigma I_0 n d$ should be set equal to one.

HELMET STRUCTURES

The actual coronal configurations constitute a belt of helmets near the equator. The goal of this section is to construct the helmet structures produced by a small number of local field sources (sunspots and active regions).

Vedenov *et al.* (2000) showed that the helmet-related structures and the helmet tops themselves are, respectively, the folds and pleats of the $B_r = 0$ surface in the corona. The pleat is described by a semicubic parabola, a curve with a cuspidal point at the top of the helmet. The curvature vector **æ** is directed outward away from the pleat everywhere below this point. However, a typical helmet observed in the corona is quite a specific structure that resembles most closely an onion. When moving along the helmet contour, the vector **æ** changes its direction: when viewed from the top, it is initially directed outward and subsequently toward the inside of the helmet.

The objective of this section is to explain this behavior of the visible contour of the $B_r = 0$ surface.

Note the following. The $B_r = 0$ surface in the simplest case of a point "charge" in a uniform field is a sphere that rests on the segment (as a diameter) connecting the point at which the charge was placed with the saddle point arising when the above fields are added. In any case, there is a portion of the $B_r = 0$ surface in the shape of a sphere at the base of the

helmet structure. Therefore, the entire helmet structure has at least one region on which the vector **æ** is directed toward the inside of the helmet. This region lies at the base of the helmet represented by the $B_r = 0$ surface.

Let us make some estimates. Consider the following magnetic field model. Let there be two dipoles: one dipole is inside the Sun, **M**, while the other dipole is near the solar surface, $\boldsymbol{\mu}$. We assume for the sake of definiteness that

$$|M| = 10|\mu|.$$

Let the dipole M produce a field $B_0 = 1$ G in polar regions,

$$\frac{M}{R_\odot^3} = B_0,$$

and the dipole μ be located near the photospheric surface at a depth of $0.03\ R_\odot$. It produces a field $B = \dfrac{\mu}{(0.03R_\odot)^3}$ on the photosphere.

The above relations yield $B = 3700$ G. The diameter of the corresponding region is $R_\odot \times 2 \times 0.03 = 42$ thousand km. This is a large bipolar sunspot.

If the depth of the dipole μ is assumed to be several factors (5–6) larger, we obtain the following field of an active region when the above relations are retained: $\sim$10 G, $L = 250$ thousand km.

Finally, we assume that the dipole moments **M** and $\boldsymbol{\mu}$ are directed toward each other. Let us determine the height h of the saddle point emerging in this case. The relation

$$\frac{M}{(R_\odot + h)^3} = \frac{\mu}{h^3},$$

yields $h = 0.86R_\odot$. In order of magnitude, this corresponds to the helmet size.

The field sources can be both the dipoles M and μ and the "charges," which are the ends of the magnetic flux tubes emerging on the photospheric surface. The latter seem preferred, since free parameters (the separations between the tube ends) are added.

In practice, the surface was constructed for a sphere of $R_\odot = 5$ length units with the poles $m_{1,2} = \pm 5$ units located on its θ axis at a distance of ± 4 units from the center of the sphere and with the "charges" $m_3 = -1$ and $m_4 = 1$ placed at the points ($x_3 = -0.5,\ y_3 = 3.6,\ z_3 = 0$) and ($x_4 = 0.5,\ y_4 = 3.6,\ z_4 = 0$) near the equator. The corresponding dipole moment vector is directed toward the initial one.

According to the aforesaid, the $B_r = 0$ surface possesses the following property: a surface current that holds a relatively dense plasma in equilibrium can exist on it.

The $B_r = 0$ surface is described by the equation

$$B_r = \sum_i m_i \frac{(\mathbf{r_i} \cdot \mathbf{r})}{r_i^3 r} = 0, \qquad (16)$$

where m_i are the powers of the sources,

$$\mathbf{r_i} = \mathbf{e_x}(x - x_i) + \mathbf{e_y}(y - y_i) + \mathbf{e_z}(z - z_i),$$

$$\mathbf{r} = \mathbf{e_x}x + \mathbf{e_y}y + \mathbf{e_z}z.$$

The line of sight is specified by the unit vector

$$\tau = \mathbf{e_x}\tau_x + \mathbf{e_y}\tau_y + \mathbf{e_z}\tau_z,$$

$$\tau_x^2 + \tau_y^2 + \tau_z^2 = 1.$$

The observed intensity of the light scattered by surface (16) is

$$\frac{1}{\cos\gamma} = \frac{|\mathrm{grad}B_r|}{(\mathrm{grad}B_r\tau)}. \qquad (17)$$

Let us turn to (16). We multiply (16) by r and take grad of both sides of the derived equality:

$$\mathrm{grad}(rB_r) = r\mathrm{grad}B_r + B_r(\mathbf{e_x} + \mathbf{e_y} + \mathbf{e_z}). \qquad (18)$$

Since the last term in (18) is zero in view of (16),

$$\mathrm{grad}B_r = \frac{1}{r}\mathrm{grad}(rB_r). \qquad (19)$$

Using (16) and (19), we get

$$\mathrm{grad}\frac{1}{r_i^3} \qquad (20)$$

$$= \mathrm{grad}\left[(x - x_i)^2 + (y - y_i)^2 + (z - z_i)^2\right]^{-3/2}$$

$$= -3\frac{\mathbf{r_i}}{r_i^5}.$$

The scalar product $(\mathbf{r_i} \cdot \mathbf{r})$ is $x(x - x_i) + y(y - y_i) + z(z - z_i)$, and, hence,

$$\mathrm{grad}(\mathbf{r_i} \cdot \mathbf{r}) = \mathbf{r} + \mathbf{r_i}. \qquad (21)$$

Turning to (19)–(21), we write

$$\mathrm{grad}B_r = \sum_i \frac{m_i}{r}\left[\frac{\mathbf{r} + \mathbf{r_i}}{r_i^3} - 3(\mathbf{r} \cdot \mathbf{r_i})\frac{\mathbf{r_i}}{r_i^5}\right]. \qquad (22)$$

In coordinate form, the expression in braces is $\mathbf{e_x}\{\} = \mathbf{e_x}\left\{\dfrac{2x - x_i}{r_i^3} - 3(\mathbf{r}\mathbf{r_i})\dfrac{x - x_i}{r_i^5}\right\}$ etc. Denoting the factors of $\mathbf{e_x}$, $\mathbf{e_y}$, and $\mathbf{e_z}$ by a_i, b_i, and c_i, respectively, we have

$$\mathrm{grad}B_r = \frac{1}{r}\sum_i m_i(\mathbf{e_x}a_i + \mathbf{e_y}b_i + \mathbf{e_z}c_i) \qquad (23)$$

$$= \mathbf{e_x}p + \mathbf{e_y}q + \mathbf{e_z}s.$$

Bearing (17) in mind, we discard the common factor $1/r$ to obtain

$$\frac{1}{\cos\gamma} = \frac{h}{j},$$

where

$$h = (p^2 + q^2 + s^2)^{1/2}, \quad j = p\tau_x + q\tau_y + s\tau_z. \quad (24)$$

If we set $\cos\gamma = 0$, then relations (18)–(24), just as (16), define an emitting surface, while the system of equations

$$\begin{cases} B_r = 0 \\ \cos\gamma = 0 \end{cases} \quad (25)$$

defines a spatial curve at the surface of radial magnetic field reversal (its visible contour). Figure 3a shows the $B_r = 0$ surface computed with the above parameters, while Fig. 3b shows the observed structure of this surface.

A MODEL OF POLAR PLUMES

The representation of polar plumes as plasma configurations in magnetic and gravitational fields (see Koutchmy *et al.* 2001; Veselovsky *et al.* 1999) satisfies the equilibrium conditions and, in several cases, the MHD stability conditions. At the same time, since a number of structures in the corona are identified with folds and pleats of the $B_r = 0$ surface (see Vedenov *et al.* 2000), it would also be natural to consider the possibility of describing polar plumes in terms of the same model.

The polar plumes are small perturbations of the equatorial surface of an equivalent dipole farther than $R_\odot$ from the solar center. In the cylindrical r, φ, z coordinates associated with the equatorial plane ($z = 0$), we assume that

$$B_r = z - \frac{\varepsilon}{r^n}\sin(u\varphi), \quad (26)$$

where ε, n, and u are the parameters that characterize the deviations of the magnetic equator from the $z = 0$ plane. As can be seen from the subsequent analysis, the ε amplitude can be a few fractions of a percent. As regards u, this quantity characterizes the diameter and may be related to the supergranule diameter, $d \sim 30$ thousand km. Accordingly, we can assume that

$$u = 2\pi R_\odot/d \approx 146.$$

Finally, n, the rate of decrease of the perturbation with distance, is the most uncertain quantity. In the heliospheric sheet model with sources in the form of "charges" $\pm q$ and a plane separating the fields of the charges, the distortion of the plane that corresponds to $n = 0$ in (26) is admissible. An arbitrary distortion that depends only on the angles θ and φ in spherical coordinates and that conserves the total flux $\int B_r ds = 0$ is also admissible. For such distortions, the energy $\int B^2/8\pi dv$ does not change. The current dependent on θ and φ decreases with distance as $1/r^2$; the field $\mathbf{B} = \{B_r, 0, 0\}$ also decreases.

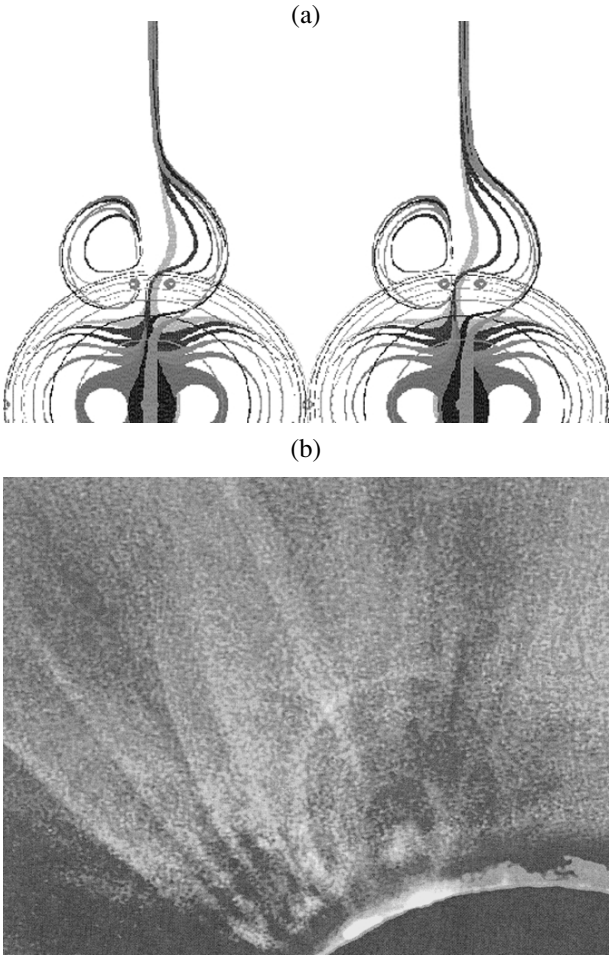

Fig. 3. The simplest helmet system: (a) a three-dimensional image of the $B_r = 0$ surface; (b) Koutchmy's observations of the same surface in August 1999.

The other extreme case is the absence of a current at $r > R_\odot$. It can be easily shown that this case is realized at $n = u$. This is unacceptable for the model under consideration, since the perturbation vanishes at a small distance from $r = R_\odot$. Next, we retain n as a free parameter and choose it after the calculation.

Let us turn to the calculation. In rectangular x, y, z coordinates, the unit vector along the line of sight is

$$\boldsymbol{\tau} = 0, \tau_y, \tau_z,$$

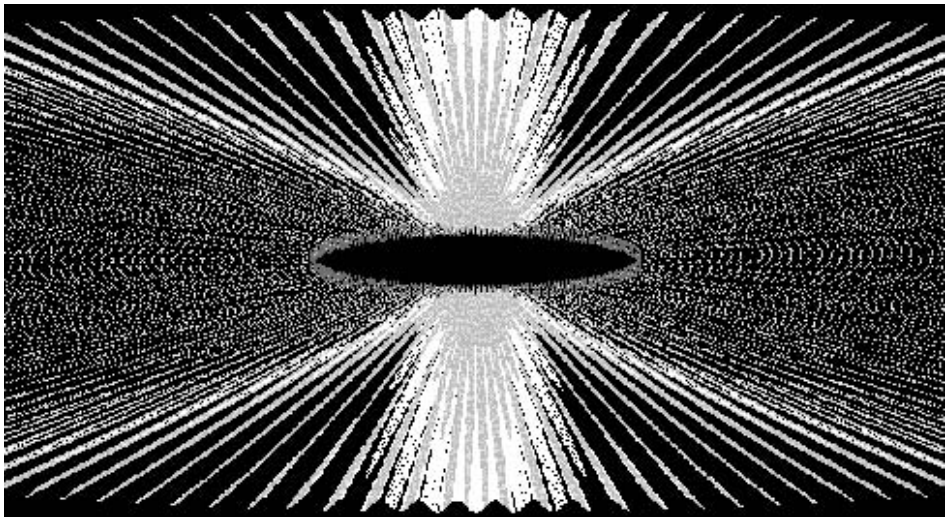

Fig. 4. Equatorial plane of the dipole with a distortion of type (26) can produce corrugations observed as polar plumes.

and the angle

$$\varphi = \arctan\frac{z}{x}, \tag{27}$$

Note that $\mathrm{grad}\dfrac{1}{r^n} = \dfrac{\mathbf{e_x}x + \mathbf{e_z}z}{r^{n+2}}(-n)$ and

$$\mathrm{grad}(\sin u\varphi) = u(\cos u\varphi)\mathrm{grad}(\arctan\frac{z}{x})$$
$$= un(\cos u\varphi)(-\mathbf{e_x}\frac{z}{r^2} + \mathbf{e_y}\frac{x}{r^2}).$$

Taking into account (27), we have

$$\mathrm{grad}B_r = \mathbf{e_x} \tag{28}$$
$$\times\left\{\frac{n\varepsilon x}{r^{n+2}}\sin u\varphi + u\varepsilon(\cos u\varphi)\frac{z}{r^{n+2}}\right\}$$
$$-\mathbf{e_y} + \mathbf{e_z}\left\{\frac{n\varepsilon z}{r^{n+2}}\sin u\varphi - \varepsilon u(\cos u\varphi)\frac{x}{r^{n+2}}\right\}$$

and easily find $1/\cos\gamma$.

RESULTS OF OUR CALCULATION. DISCUSSION

Figure 3a shows the computed $B_r = 0$ surface for four field sources: m_1 and m_2 model the general solar field; m_3 and m_4 model inclusions of the opposite sign. A three-dimensional image of the surface is presented. We see that the surface is a helmet.

Figure 4 shows the $1/\cos\gamma$ distribution for surface (25). We assumed that $\varepsilon = 0.001$, $n = 2$, and $u = 146$. The streamer structure manifests itself clearly, without any noticeable reduction in the contrast at a distance of $\approx 4R_\odot$. At the same time, we clearly see the streamers only in polar regions, while in E- and W-limb regions, the contrast vanishes due to the superposition of many streamers. The smaller the angle between the line of sight and the $z = 0$ plane the brighter the described picture. This is because the line of sight, being almost parallel to the plane, follows along the fold ($u \approx 146$).

It should be noted that a current exists in the equatorial plane at all $n \neq u$; this current increases with decreasing n. At $n = 0$, the current decreases as $1/r^2$, while at all $n > 0$, the rate of decrease of the current is higher than $1/r^2$. Significantly, in contrast to the models given by relation (16), the presence of a current in model (25) is of fundamental importance.

Koutchmy *et al.* (2001) associated the polar plumes with the current flowing in polar regions. In this case, the equilibrium condition for a plasma with a current in a gravitational field was satisfied. The advantage of the model considered above is that the current is localized near the equatorial plane, which, of course, can be verified using observational data. This could be done if continuous data on the coronal structure at $R_\odot < r < 2.2R_\odot$ similar to the SOHO LASCO-2 data were available.

It makes sense to estimate the distance at which the influence of the solar wind in the stationary equations of motion may be disregarded. The critical height r_{cr} is known (Parker 1963) to be determined from the condition for the equality between the thermal energy and the energy of the ordered plasma motion $mv^2 = kT$, where m is the reduced proton mass, v is the velocity, and T is the temperature (10^6 K). At $T = \mathrm{const}$, we have for r_{cr} (see Brandt 1970)

$$r_{\mathrm{cr}}/R_\odot = \frac{GM_\odot}{2R_\odot kT} = 6.8,$$

where G is the gravitational constant.

Given the variability of the temperature, the thermal conductivity, and other parameters, r_{cr} lies within the range $(10–20)R_\odot$ (see the radio observations of Lotova and Vladimirsky 1998). Thus, these values have the meaning of estimates. Significantly, the velocity at $r < r_{cr}$ decreases rapidly with decreasing distance r (in accordance with the plasma continuity condition and the increase in plasma density). Therefore, in several cases, the equilibrium equations in MHD form, to which this paper is devoted, may be considered to be valid.

CONCLUSIONS

We considered two types of filamentary structures in the solar atmosphere. Structures in which the plasma density is constant along the magnetic field lines belong to the first type. The scale lengths of such structures are smaller than their scale heights kT/mg.

The second type of filamentary structures is characterized by an inverse relationship between the scale lengths and scale heights in the corona. This type results from the formation of folds on the $B_r = 0$ surface.

Vedenov *et al.* (2000) showed that the Whitney folds and pleats of the $B_r = 0$ surface describe the tops of helmets and their surroundings. In this paper, we showed that the same is true for a more general case: almost all the structures of a coronal helmet can be described by the projection of the $B_r = 0$ surface onto the plane of the sky. As far as we know, this model of helmets has not yet been considered (see the review by Koutchmy and Livshits 1992).

The projection effect plays a significant role in our model calculations of polar plumes. When the corrugated surface is observed at an acute angle, the structures that are elongated along the line of sight are distinguished on it. In general, they owe their existence to an azimuthal current on the equatorial surface of the magnetic dipole.

REFERENCES

1. J. C. Brandt, *Introduction to the Solar Wind* (Freeman, San Francisco, 1970; Mir, Moscow, 1979), p. 71.
2. E. Kamke, *Gewöhnliche Differentialgleichungen* (Academic, Leipzig, 1959; Inostrannaya Literatura, Moscow, 1951), p. 69.
3. S. Koutchmy, These de doctorat d'etat es sciences: physique (A l'Univ. Paris VI, C.N.R.S., Paris, 1972).
4. S. L. Koutchmy, O. K. Koutchmy, V. A. Koutvitsky, *et al.*, Izv. Ross. Akad. Nauk **59**, 119 (1995).
5. S. Koutchmy and M. Livshits, Space Sci. Rev. **61**, 293 (1992).
6. S. L. Koutchmy, M. M. Molodensky, and V. L. Merzlyakov, Astron. Zh. **78**, 953 (2001) [Astron. Rep. **45**, 834 (2001)].
7. L. D. Landau and E. M. Lifshitz, *Electrodynamics of Continuous Media* (Pergamon Press, Oxford, 1982; Nauka, Moscow, 1992), p. 346.
8. N. A. Lotova and K. V. Vladimirsky, Geomagn. Aéron. **38**, 156 (1998) [Geomagn. Aeron. **38**, 373 (1998)].
9. M. M. Molodensky, *Coll. IAU No. 144: Solar Coronal Structures*, Ed. by V. Rusin, P. Heintzel, and J.-C. Vial (1993), p. 122.
10. E. N. Parker, *Interplanetary Dynamical Processes* (Interscience, New York, 1963; Mir, Moscow, 1965).
11. K. Shibata, Y. Ishido, L. Acton, *et al.*, Publ. Astron. Soc. Jpn. **44**, L173 (1992).
12. A. A. Vedenov, V. A. Koutvitsky, S. L. Koutchmy, *et al.*, Astron. Zh. **77**, 134 (2000) [Astron. Rep. **44**, 112 (2000)].
13. I. S. Veselovsky, A. N. Zhukov, S. Koutchmy, *et al.*, in *Plasma Dynamics, 8th SOHO Workshop, Paris, France, 1999*, Ed. by J.-C. Vial and B. Kaldeich-Schumann, ESA SP **446**, 675 (1999).

Translated by V. Astakhov

Astronomy Letters, Vol. 31, No. 6, 2005, pp. 406–413. Translated from Pis'ma v Astronomicheskiĭ Zhurnal, Vol. 31, No. 6, 2005, pp. 456–464.

Rapid Damping of the Oscillations of Coronal Loops with an Azimuthal Magnetic Field

B. B. Mikhalyaev*

Kalmyk State University, Elista, Kalmykia, Russia

Received September 27, 2004

Abstract—We consider the MHD oscillations of an inhomogeneous coronal loop that consists of a dense cord surrounded by a shell. The magnetic field is longitudinal in the cord and has only an azimuthal component in the shell. The parameters of the loop are chosen to be such that there are no resonances; i.e., the resonance points are cut off. This choice is dictated by the formulated problem of considering the influence of the radiation of MHD waves into the surrounding space on the loop oscillations, thereby ruling out the possibility of resonant energy absorption. The wave radiation efficiency is high and allows low oscillation Q-factors, which are equal in order of magnitude to their observed values, to be obtained.

Key words: *Sun*.

INTRODUCTION

Explaining the observed rapid damping of transverse coronal loop oscillations is an important problem of modern solar physics (Aschwanden *et al.* 1999; Nakariakov *et al.* 1999). The loops are thin magnetic flux tubes with diameters (6.3–16.8 thousand km) much smaller than their lengths (146–406 thousand km) (Ofman and Aschwanden 2002). The Q-factor of the observed oscillations is low ($Q \sim 10$). The mechanisms of viscous dissipation with small Reynolds numbers (Nakariakov *et al.* 1999) and phase mixing of Alfvèn waves in a loop or resonant energy absorption in a thin layer surrounding the loop (Ruderman and Roberts 2002; Ruderman 2003; Van Doorsselaere *et al.* 2004) are invoked to account for this effect. There is also the point of view that the damping could be caused by the radiation of magnetosonic waves by a loop into the surrounding corona (Solov'ev *et al.* 2002, 2003; Mikhalyaev and Solov'ev 2004). An advantage of this approach is that there is no need to use dissipative processes, whose existence in the ordinary solar plasma seems problematic. The radiative damping mechanism allows us to restrict our analysis to ideal MHD, which seems most natural under typical conditions in the solar atmosphere.

The radiation of magnetosonic waves is possible if the loop is cross-sectionally inhomogeneous. Solov'ev *et al.* (2003) and Mikhalyaev and Solov'ev (2004) used a simple model of an inhomogeneous loop that consisted of a dense cylindrical cord surrounded by a coaxial shell. The plasma and the magnetic field in the cord and the shell were assumed to be uniform. This model allows low oscillation Q-factors ($Q = 20$–40) to be obtained. In this case, however, the loop radius must be much larger than the cord radius, and the Alfvén speed in the shell must be severalfold higher than that in the surrounding corona. The latter implies that the plasma density in the shell is much lower (by an order of magnitude) than that in the corona, which seems unlikely. In this paper, we attempt to overcome this difficulty and consider a loop with a shell in which the magnetic field has an azimuthal component. The presence of an azimuthal field in the shell changes significantly the pattern of oscillations—the radiation efficiency of magnetosonic waves increases appreciably, and low Q-factors can be obtained when the Alfvèn speed in the shell differs only slightly from that in the corona.

The coronal magnetic flux tubes are known to be twisted; i.e., in addition to the longitudinal magnetic field, they also contain an azimuthal component. The twisting of magnetic field lines in the convection zone, the formation of magnetic flux tubes, and their subsequent expulsion into the atmosphere could give rise to such tubes. In a rarefied atmosphere, the tube undergoes expansion. As the tube expands, the azimuthal magnetic field concentrates on the tube periphery, and a shell with an essentially azimuthal field ($B_z/B_\varphi \to 0$, $B_\varphi \sim r^{-1}$) is formed. The longitudinal magnetic field persists only in the central part of the tube (Parker 1979). The mathematical difficulties that arise in describing such a coronal tube force us to use

*E-mail: bbmikh@kalmsu.ru

1063-7737/05/3106-0406$26.00

its crude model in which the magnetic field has only a longitudinal component in the central part and only an azimuthal component on the periphery.

The presence of an azimuthal magnetic field suggests that longitudinal electric currents flow in the tube. In an actual magnetic flux tube with a continuous field distribution located in an external longitudinal magnetic field, the azimuthal component initially increases and subsequently decreases to zero with distance from the tube axis. Consequently, two regions with oppositely directed longitudinal currents exist. The currents in the central region adjacent to the tube axis produce an azimuthal magnetic field, while the currents in the outer region produce a screening effect. In our model, these currents concentrate at the cord–shell and shell–corona boundaries where there are discontinuities in magnetic induction. The existence of surface currents is an inevitable result of choosing simplified models. For example, in the classical model of a homogeneous magnetic flux tube (Spruit 1982; Edwin and Roberts 1983), there is a discontinuity in longitudinal magnetic field at the tube boundary, and, hence, an azimuthal surface current exists at the boundary. The longitudinal currents could probably be generated by sources in the photosphere or in deeper layers (Alfvèn and Carlqwist 1967). In this case, the coronal magnetic flux tubes resemble electric circuits closed on the photosphere with the emf sources in dense layers.

The complex structure of the solar corona, which consists of many thin magnetic loops, makes it necessary to develop the various theoretical models of magnetic flux tubes to determine the coronal plasma parameters. This is a problem of the so-called coronal seismology (Roberts 2004). The model of a coronal loop presented here is of considerable interest from this point of view as well.

This paper is structured as follows. We describe the plasma and magnetic field distributions in a tube and formulate the basic equations. In the thin-tube approximation, we derive the dispersion relation and the damping coefficient for fast magnetosonic waves. We give numerical calculations, as applied to the description of solar coronal-loop oscillations.

BASIC EQUATIONS

The magnetohydrostatic equilibrium in the absence of gravity in a cylindrical symmetry is described by the equation

$$\frac{dp(r)}{dr}+\frac{1}{4\pi}B_z(r)\frac{dB_z(r)}{dr}+\frac{1}{4\pi}B_\varphi(r)\frac{1}{r}\frac{d}{dr}rB_\varphi(r)=0.$$

The simplest solutions of this equation are: (i) $p=$ const, $B_z=$ const, $B_\varphi=0$ and (ii) $p=$ const, $B_z=0$, $B_\varphi=\text{const}\times r^{-1}$. The first and second solutions give a magnetic field with only longitudinal and azimuthal components, respectively. We use them to develop a model of a double magnetic flux tube.

Let us consider a cylindrical tube of radius a in which a central part of radius b ($b<a$) is isolated. The isolated part is called a cord, and the plasma density $\rho_{0\mathrm{i}}$ in the cord is assumed to exceed the density $\rho_{0\mathrm{e}}$ in the surrounding space of the tube. The cylindrical layer between the cord and the tube surroundings is called a shell. Below, the subscripts i, m, and e denote the parameters that refer to the cord, the shell, and the external surroundings, respectively. Let us consider a cylindrical coordinate system whose axis coincides with the tube axis; in this coordinate system, the cord, the shell, and the external surroundings are specified as the regions $r<b$, $b<r<a$, and $a<r$, respectively. We assume that $\rho_{0\mathrm{i}}$ and $\rho_{0\mathrm{e}}$ are uniform and that the density in the shell decreases with radius: $\rho_{0\mathrm{m}}=\rho_0/(\alpha r)^2$. The parameter α is the scale parameter, which is the reciprocal of the length. The quantity ρ_0 has the dimensions of density and specifies its characteristic values in the shell. The gas pressures $p_{0\mathrm{i}}$, $p_{0\mathrm{m}}$, and $p_{0\mathrm{e}}$ are assumed to be uniform. The induction of the equilibrium magnetic field has the distribution

$$\mathbf{B}_0(r)=\begin{cases}B_{0\mathrm{i}}\mathbf{e}_z, & r<b\\ (B_0/\alpha r)\mathbf{e}_\varphi, & b<r<a\\ B_{0\mathrm{e}}\mathbf{e}_z, & a<r.\end{cases}$$

The constant quantities $B_{0\mathrm{i}}$ and $B_{0\mathrm{e}}$ define a uniform magnetic field in the cord and an external uniform magnetic field, respectively. The field in the shell is purely azimuthal and potential. The quantity B_0 has the dimensions of induction and specify its characteristic values in the shell.

The equilibrium conditions at the boundaries of the regions can be obtained by integrating the magnetohydrostatic equilibrium equation over the variable r within the limits on both sides of the boundary:

$$p(r_2)-p(r_1)+\frac{1}{8\pi}B_z(r_2)^2-B_z(r_1)^2+\frac{1}{8\pi}B_\varphi(r_2)^2-B_\varphi(r_1)^2+\frac{1}{4\pi}\int_{r_1}^{r_2}\frac{B_\varphi(r)^2}{r}\,dr=0.$$

Considering the two boundaries, $r=a$ and $r=b$, in turn and letting the integration limits approach the boundary, we obtain the equilibrium condition for the magnetic flux tube

$$p_{0\mathrm{i}}+\frac{B_{0\mathrm{i}}^2}{8\pi}=p_{0\mathrm{m}}+\frac{B_0^2}{8\pi\alpha^2b^2},$$

$$p_{0m} + \frac{B_0^2}{8\pi\alpha^2 a^2} = p_{0e} + \frac{B_{0e}^2}{8\pi}.$$

The cord and the surroundings of the tube are characterized by the corresponding Alfvèn and sound speeds, $V_{Ai}, C_{si}, V_{Ae}, C_{se}$. In the shell, the sound speed is C_{sm} and the Alfvèn speed has characteristic values given by $V_{Am}^2 = B_0^2/4\pi\rho_0$. If we disregard the gas pressure in the coronal conditions, the equilibrium conditions in terms of the speeds will be

$$\rho_{0i}V_{Ai}^2 = \rho_0 V_{Am}^2/\alpha^2 b^2, \quad \rho_0 V_{Am}^2/\alpha^2 a^2 = \rho_{0e}V_{Ae}^2. \tag{1}$$

Let us consider small plasma and field perturbations that are described by linearized ideal MHD equations:

$$\rho_0\frac{\partial \mathbf{v}}{\partial t} = -\nabla p + \mathrm{curl}\mathbf{B}\times\frac{\mathbf{B}_0}{4\pi} + \mathrm{curl}\mathbf{B}_0\times\frac{\mathbf{B}}{4\pi},$$
$$\frac{\partial p}{\partial t} = -\gamma p_0 \mathrm{div}\mathbf{v} - \mathbf{v}\nabla p_0,$$
$$\frac{\partial \mathbf{B}}{\partial t} = \mathrm{curl}(\mathbf{v}\times\mathbf{B}_0),$$

where $\mathbf{B}_0$ is the unperturbed magnetic induction; p_0 and ρ_0 are the unperturbed plasma pressure and density; and $\mathbf{B}$, p, and $\mathbf{v}$ are the induction, pressure, and speed perturbations, respectively. We seek solutions in the form of cylindrical modes, $f(r,t) = f(r)\exp(im\varphi + k_z z - i\omega t)$, where k_z is the longitudinal wave number, and ω is the oscillation frequency.

For unperturbed distributions of the form $\rho_0 = \rho_0(r)$, $p_0 = p_0(r)$, and $\mathbf{B}_0 = B_{0z}(r)\mathbf{e}_z + B_{0\varphi}(r)\mathbf{e}_\varphi$, the following equations can be derived for the radial speed $v_r(r)$ and the perturbation of the total pressure $P(r) = p(r) + \mathbf{B}(r)\mathbf{B}_0(r)/4\pi$ (Appert *et al.* 1974):

$$D\frac{d}{dr}rv_r = rC_2 i\omega P + rC_1 v_r, \tag{2}$$
$$D\frac{d}{dr}i\omega P = -C_1 i\omega P - C_3 v_r,$$

where

$$D = K_1 K_2, \tag{3}$$
$$C_1 = \frac{B_{0\varphi}}{2\pi r}\left(\rho_0^2\omega^4 B_{0\varphi} - \frac{m}{r}(\mathbf{kB}_0)K_2\right),$$
$$C_2 = \rho_0^2\omega^4 - \left(k_z^2 + \frac{m^2}{r^2}\right)K_2,$$
$$C_3 = D\left(K_1 + \frac{B_{0\varphi}}{2\pi}\frac{d}{dr}\frac{B_{0\varphi}}{r}\right)$$
$$+ \left(\frac{B_{0\varphi}}{2\pi r}\right)^2\left(\rho_0^2\omega^4 B_{0\varphi}^2 - (\mathbf{kB}_0)^2 K_2\right).$$

Here, we use the notation

$$(\mathbf{kB}_0) = k_z B_{0z} + \frac{mB_{0\varphi}}{r}, \tag{4}$$
$$K_1 = \rho_0\omega^2 - \frac{(\mathbf{kB}_0)^2}{4\pi},$$
$$K_2 = \rho_0\omega^2(\gamma p_0 + \frac{|\mathbf{B}_0|^2}{4\pi}) - \frac{\gamma p_0(\mathbf{kB}_0)^2}{4\pi}.$$

An equation for $P(r)$ can be derived from Eqs. (2)–(4):

$$\frac{d^2P}{dr^2} + \left(\frac{C_3}{rD}\frac{d}{dr}\frac{rD}{C_3}\right)\frac{dP}{dr} \tag{5}$$
$$+ \left(\frac{C_3}{rD}\frac{d}{dr}\frac{rC_1}{C_3} + \frac{C_2C_3 - C_1^2}{D^2}\right)P = 0.$$

Since $B_{0z} = 0$ in the shell, the radial equation (5) is the same for $m = \pm 1$. Solutions of the form $f(r,t) = f(r)\cos\varphi\cos(k_z z)\exp(-i\omega t)$, which describe standing waves, can then be obtained. In this case, the tube undergoes transverse displacements like a vibrating string. The solution of the radial equation for the shell for the $m = \pm 1$ modes is given in the Appendix. In addition to the zero and infinite points, it has two singular points, the Alfvèn resonance point r_A and the cusp resonance point r_C. We assume that the tube radius is $a < \min(r_A, r_C)$; in this case, there are two analytical basis solutions of the radial equation in the region $b < r < a$, i.e., in the shell, which we denote by $M(r)$ and $N(r)$. The principal terms of their expansions at zero are

$$M(r) \sim \frac{1}{r}, \quad N(r) \sim \frac{1}{r^3}. \tag{6}$$

We write the total-pressure perturbation in the shell as a linear combination of the basis solutions, $P_m(r) = FM(r) + GN(r)$, where F and G are constants. We express the perturbation of the radial speed $v_{rm}(r)$ in terms of $P_m(r)$ from (2).

In the cord and the external surroundings where the magnetic field and the plasma are uniform, Eqs. (2)–(4) take the form

$$v_r(r) = -\frac{i\omega}{(\omega^2 - V_A^2 k_z^2)\rho_0}\frac{dP(r)}{dr}, \tag{7}$$

$$r^2\frac{d^2P}{dr^2} + r\frac{dP}{dr} + (k^2r^2 - m^2)P = 0, \tag{8}$$

where we use the notation

$$k^2 = \frac{(\omega^2 - V_A^2k_z^2)(\omega^2 - C_s^2k_z^2)}{(V_A^2 + C_s^2)(\omega^2 - C_t^2k_z^2)}, \tag{9}$$
$$C_t^2 = \frac{V_A^2C_s^2}{V_A^2 + C_s^2}.$$

The parameter k has the meaning of a radial wave number; the quantity C_t is called a tube speed. The perturbations of the total pressure in the cord, $P_i(r)$, and the external surroundings, $P_e(r)$, can be expressed in terms of the solutions of the Bessel equation or a modified Bessel equation. The corresponding speeds v_{ri} and v_{re} can be determined using (7).

We subject the solutions in the three regions, $\{v_{ri}(r), P_i(r)\}$, $\{v_{rm}(r), P_m(r)\}$, and $\{v_{re}(r), P_e(r)\}$, to the boundary conditions

$$v_{ri}(b) = v_{rm}(b), \quad v_{rm}(a) = v_{re}(a), \qquad (10)$$
$$P_i(b) = P_m(b) + \frac{B_{0\varphi}^2(b)}{4\pi i\omega b} v_{ri}(b),$$
$$P_m(a) + \frac{B_{0\varphi}^2(a)}{4\pi i\omega a} v_{ri}(a) = P_e(a).$$

The relation between the wave phase velocity ω/k_z and the wave number k_z, i.e., the dispersion relation, can be derived from (10).

THE DISPERSION RELATION FOR A THIN TUBE

Below, we restrict our analysis to the $m = \pm 1$ modes, i.e., consider only the kink oscillations of the tube. If the loop oscillates on one half-wave, then the longitudinal wave number k_z is related to the loop length L by $k_z = \pi/L$. Consider the wavelengths much longer than the tube radius, i.e., $a \ll L$, implying that $k_z a \ll 1$. This is called a thin-tube approximation. In this approximation, the arguments of the solutions found are small, and we can use their approximate expressions by retaining the first terms in the expansions.

The solution in the cord can be expressed in terms of the Bessel function J_1 according to (7)–(9):

$$v_{ri}(r) = -i\omega X_{0i} \frac{J_1'(k_i r)}{J_1'(k_i b)},$$
$$P_i(r) = X_{0i} \frac{\rho_{0i}(\omega^2 - V_{Ai}^2 k_z^2)}{k_i} \frac{J_1(k_i r)}{J_1'(k_i b)}.$$

A similar situation takes place in the external surroundings, where the solution can be expressed in terms of the Hankel function of the first kind:

$$v_{re}(r) = -i\omega X_{0e} \frac{H_1^{(1)\prime}(k_e r)}{H_1^{(1)\prime}(k_e a)},$$
$$P_e(r) = X_{0e} \frac{\rho_{0e}(\omega^2 - V_{Ae}^2 k_z^2)}{k_e} \frac{H_1^{(1)}(k_e r)}{H_1^{(1)\prime}(k_e a)},$$

where X_{0i} and X_{0e} are arbitrary constants.

The solution in the shell is

$$v_{rm}(r) = -i\omega \left[\frac{C_1(r)}{C_3(r)} (FM(r) + GN(r)) + \frac{D(r)}{C_3(r)} (FM'(r) + GN'(r)) \right],$$
$$P_m(r) = FM(r) + GN(r),$$

where F and G are arbitrary constants, while D, C_1, and C_3 are defined by (3).

In coronal conditions, the gas pressure may be ignored compared to the magnetic pressure by formally setting $C_{sm} = 0$. In the calculations presented in the Appendix, we should set $\mu = 0$. The radial wave number for the waves in the shell is then $k_m = \omega/V_{Am}$. If the mode under consideration has a finite phase velocity for $k_z \to 0$, then we can use the thin-tube approximation and the approximate expressions (6) for the solutions in the shell. In the expansions of the functions J_1 and $H_1^{(1)}$, we also retain only the principal terms. Next, using the approximate expressions for D, C_1, and C_3

$$\frac{D}{C_3} \approx -\frac{\alpha^2 r^4}{\rho_0 V_{Am}^2}, \quad \frac{C_1}{C_3} \approx -\frac{2\alpha^2 r^3}{\rho_0 V_{Am}^2},$$

and eliminating the arbitrary constants in the boundary conditions (10), we obtain the dispersion relation for a thin tube

$$\alpha^2 a^2 b^2 (a^2 - b^2) \rho_{0i} (\omega^2 - V_{Ai}^2 k_z^2) \qquad (11)$$
$$\times \rho_{0e} (\omega^2 - V_{Ae}^2 k_z^2) - 2\rho_0 V_{Am}^2$$
$$\times [b^2 \rho_{0i} (\omega^2 - V_{Ai}^2 k_z^2) + a^2 \rho_{0e} (\omega^2 - V_{Ae}^2 k_z^2)] = 0.$$

It should be borne in mind that the tube parameters in this equation are constrained by conditions (1).

Equation (11) is the dispersion relation in the zeroth approximation for small wave numbers k_z. It has two real solutions that describe undamped oscillations, which can be easily found. One of these describes a fast magnetosonic wave whose phase velocity exceeds the Alfvèn speed in the corona. Therefore, it propagates radially into the surrounding space, i.e., is radiated by the tube. The second solution in the conditions under consideration typical of the solar corona yields values of $k_e a$ that are much larger than unity, in opposition to the thin-tube approximation, and we exclude this solution.

Damping manifests itself as the effect of the next (first) order with respect to the small $k_z a$. In the first approximation, the dispersion relation has a complex solution with a relatively small imaginary part. Let us write the complex frequency as

$$\omega = \omega_0 (1 + \epsilon),$$

where ω_0 is the solution of the dispersion relation in the zeroth approximation, and the dimensionless

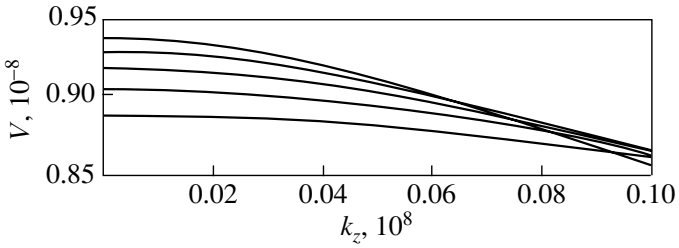

Fig. 1. Dispersion curve for the fast magnetosonic wave radiated by a magnetic flux tube. The tube length is $L = 130$ thousand km, and the cord radius is $b = 2$ thousand km. The curves successively correspond, from top to bottom, to the shell radii $a = 13$, 12, 11, 10, and 9 thousand km. The remaining parameters are given in the text.

quantity ϵ gives the first correction. Its imaginary part determines the damping coefficient $-\omega_0 Im\epsilon$, while the ratio $Q = -1/2Im\epsilon$ is the Q-factor of the oscillations. Since the real part of ϵ gives only a small correction to the zeroth approximation ω_0, we are interested only in its imaginary part, for which the following expression holds:

$$8\omega_0^2 Im\epsilon\Big[\alpha^4 a^2 b^2 (a^2 - b^2)\rho_{0e}\rho_{0i}(2\omega_0^2 \quad (12)$$
$$- V_{Ae}^2 k_z^2 - V_{Ai}^2 k_z^2) - 2\rho_0 V_{Am}^2(\alpha^2 a^2 \rho_{0e} + \alpha^2 b^2 \rho_{0i})\Big]$$
$$+ \pi k_e^2 a^2\Big[\alpha^4 a^2 b^2 (a^2 - b^2)\rho_{0e}\rho_{0i}(\omega_0^2 - V_{Ae}^2 k_z^2)$$
$$\times (\omega_0^2 - V_{Ai}^2 k_z^2) - 2\rho_0 V_{Am}^2(\alpha^2 a^2 \rho_{0e}(\omega_0^2 - V_{Ae}^2 k_z^2)$$
$$- \alpha^2 b^2 \rho_{0i}(\omega_0^2 - V_{Ai}^2 k_z^2))\Big] = 0.$$

Figure 1 shows the dispersion curves at small wave numbers for the chosen fast mode derived from (11) at various tube radii. Figure 2 shows the dependence of the oscillation Q-factor derived from (12).

RESULTS AND THEIR APPLICATION

We considered a cylindrical magnetic flux tube with a radially nonuniform distribution of the plasma parameters and the magnetic field. The tube is a dense cylindrical cord surrounded by a coaxial shell. The magnetic field is longitudinal along the tube axis in the cord and has only an azimuthal component in the shell; for definiteness, the field in the shell was chosen to be potential. This implies that a longitudinal surface current producing the magnetic field in the shell flows at the cord–shell boundary. An oppositely directed current equal in magnitude to it flows at the shell–corona boundary; this current screens the azimuthal magnetic field in the shell. The electromotive forces located in the photosphere or in deeper dense layers could be the sources of these currents (Alfvèn and Carlqwist 1967). This model gives a rough description of a coronal magnetic flux tube with an azimuthal magnetic field. The expansion of a twisted magnetic flux tube after its expulsion into the atmosphere causes the azimuthal field to be raked up to the tube periphery, where a shell with an almost azimuthal magnetic field is formed (Parker 1979).

We studied the kink oscillations of the tube in an external uniform longitudinal magnetic field. There are two singular points of the radial equation in the shell, the Alfvèn and cusp resonance points. We chose the tube parameters at which the resonance points are cut off (they remain outside the tube); therefore, the solutions used in the shell are analytical. Thus, there are no resonance effects in the problem under consideration. This is done to estimate the rate of the oscillation damping attributable to wave radiation, and the possibility of the oscillation energy being absorbed near the resonance surfaces is ruled out.

For the $m = 1$ mode, which describes the kink oscillations of a loop observed with TRACE (Aschwanden *et al.* 1999; Nakariakov *et al.* 1999; Ofman and Aschwanden 2002), we derived the dispersion relation (11) in the thin-tube approximation, where the wavelength is much larger than the tube radius. Its solution describes the fast magnetosonic waves propagating into the external surrounding space of the tube, i.e., radiated by the tube. One solution has large values and increases infinitely when the longitudinal wave number approaches zero; the other solution has a finite limit. For the first mode, the thin-tube approximation is not justifiable; it must be described by the exact dispersion relation. For the second mode, the thin-tube approximation is admissible. We studied the tube oscillations precisely at this mode. We found the oscillation damping coefficient (12) attributable to the energy losses through radiation. In Figs. 1 and 2, the phase velocity and the Q-factor are plotted against the wave number in the range of small longitudinal wave numbers, where the thin-tube approximation is applicable.

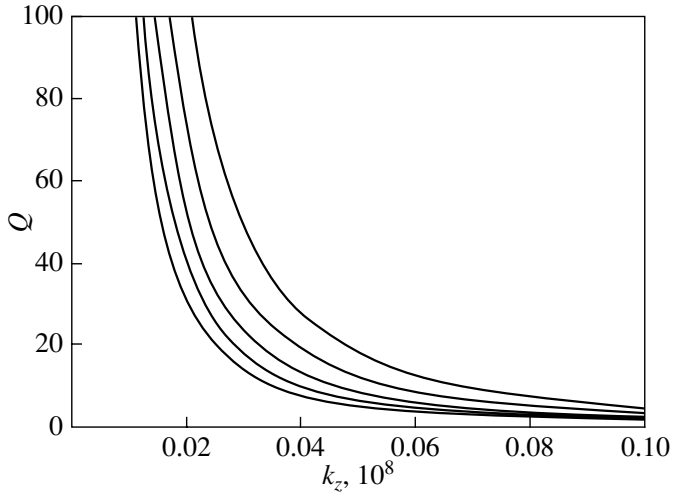

Fig. 2. Q-factor of the tube oscillations at the radiated fast magnetosonic mode. The tube length is $L = 130$ thousand km, and the cord radius is $b = 2$ thousand km. The curves successively correspond, from bottom to top, to the shell radii $a = 13$, 12, 11, 10, and 9 thousand km.

We applied the results obtained to the oscillations of solar coronal loops. The corona is characterized by Alfvèn speeds much higher than the sound speed; we chose $V_{\rm Ae} = 700$ km s^{-1} and $C_{\rm se} = 100$ km s^{-1}. The density in the cord is $\rho_{0\rm i} = 5\rho_{0\rm e}$, and a characteristic density of $\rho_0 = 5\rho_{0\rm e}$ was chosen for the shell. The Alfvèn speeds in the cord, $V_{\rm Ai}$, and the shell, $V_{\rm Am}$, can be determined from conditions (1). For the sound speeds, we chose $C_{\rm si} = 140$ km s^{-1} and $C_{\rm sm} = 120$ km s^{-1}. The scale parameter is $\alpha = 0.25$ cm^{-1}.

We see from Fig. 2 that the Q-factor increases with decreasing wave number, i.e., with increasing tube length. For example, at the tube radius $a = 12$ thousand km and the cord radius $b = 2$ thousand km, the Q-factor increases from 19.7 to 84.9 as the tube length L changes from 110 thousand to 230 thousand km. The oscillation period takes on values within the range 239 to 497 s. The Alfvèn speed in the shell is the same, 939 km s^{-1}. The plasma density in the shell varies with radius; it takes on values of $20\rho_{0\rm e}$ at the boundary with the cord and $0.56\rho_{0\rm e}$ at the boundary with the corona in all cases. We consider a density that is a factor of 20 higher than that in the corona to be admissible, because this is confirmed observationally. The density in coronal loops was estimated to be within the range 8–18 (Aschwanden 2001). Since the longitudinal wave number is small and $k_{\rm e}a < 0.29$, the thin-tube approximation is applicable in this case. The coordinates of the Alfvèn resonance point lie within the range $r_{\rm A} = 35.7$–74.3 thousand km, which exceed the tube radius; therefore, the resonance point does not fall within the shell region under the conditions in question. The cusp resonance in coronal conditions is absent altogether. The Q-factor and the period increase with cord radius. If b changes from 1 to 4 thousand km (at $a = 12$ thousand km and $L = 130$ thousand km), then the period increases from 270 to 328 s, while the Q-factor increases from 18.1 to 190. The Alfvèn speed in the shell is 939 km s^{-1}.

Thus, the Alfvèn speed in the shell can be made close to that in the surrounding corona. We thus overcame the main difficulty of our previous model of a double magnetic flux tube, in which the magnetic field in the shell was assumed to be uniform (Solov'ev *et al.* 2003; Mikhalyaev and Solov'ev 2004). The difficulty was that the effective radiation for which the loop oscillations were rapidly damped was possible only if the Alfvèn speed in the shell exceeded significantly (by several factors) that in the corona, and if the plasma density in the shell was an order of magnitude lower than that of the corona. Here, we obtained more realistic conditions under which the Alfvèn speeds and densities in the shell and the corona are similar.

Our calculations show that low Q-factors close to their observed values (Aschwanden *et al.* 1999; Nakariakov *et al.* 1999; Ofman and Aschwanden 2002) and indicative of rapid oscillation damping can be obtained. Thus, a double magnetic flux tube with a strongly twisted magnetic field in the shell can serve as an acceptable model for coronal loops, and the observed rapid damping of transverse loop oscillations can be explained in terms of the effective radiation of fast magnetosonic waves into the surrounding corona by the loop. In this case, there is no need to invoke dissipative effects; the phenomenon can be explained in terms of ideal magnetohydrodynamics.

ACKNOWLEDGMENTS

This work was supported by the Russian Foundation for Basic Research (project no. 02-02-16156). I wish to thank Prof. Solov'ev for helpful discussions. I am also grateful to the referees whose remarks improved the paper.

APPENDIX

SOLUTION OF THE RADIAL EQUATION

It is well known that the solutions of the radial equation (11) have singularities at $r = 0$ and at zeroes of the coefficient D and that the zeros of C_3 give no singularities (Appert *et al.* 1974). Let us introduce the dimensionless radial variable $\zeta = \alpha r$ and the dimensionless parameters

$$\lambda = \frac{\omega^2}{\alpha^2 V_{\rm Am}^2}, \quad \mu = \frac{C_{\rm sm}^2}{V_{\rm Am}^2}, \quad \nu = \frac{k_z^2}{\alpha^2}.$$

For K_1 and K_2, we then derive the following expression from (4):

$$K_1 = \frac{\lambda\zeta^2 - 1}{\zeta^4}, \quad K_2 = \frac{\lambda\mu\zeta^2 + \lambda - \mu}{\zeta^4}.$$

Clearly, the singular points of the equation are determined by the zeros of these functions. If they lie in the positive part of the real axis in the complex ζ plane, then they give resonance points. In this case, the zeros of the functions K_1 and K_2 give the Alfvèn, $\zeta_{\rm A}$, and cusp, $\zeta_{\rm C}$, resonance points, respectively. In dimensional quantities, we denote the resonance points by $r_{\rm A}$ and $r_{\rm C}$: $r_{\rm A} = \zeta_{\rm A}/\alpha$, $r_{\rm C} = \zeta_{\rm C}/\alpha$. The condition for the absence of a cusp resonance is $\lambda > \mu$. In the original notation, it appears as $\omega > C_{\rm sm}\alpha$.

Let us write the radial equation in reduced form:

$$\frac{d^2P}{d\zeta^2} + p(\zeta)\frac{dP}{d\zeta} + q(\zeta)P = 0.$$

The coefficients $p(\zeta)$ and $q(\zeta)$ are

$$p(\zeta) = \frac{5}{\zeta} - \frac{2\lambda\zeta(2\lambda\mu\zeta^2 + \lambda - 6\mu)}{\lambda^2\zeta^4\mu + \lambda^2\zeta^2 - 6\lambda\mu\zeta^2 - \lambda + \mu} + \frac{2\lambda\mu\zeta}{\lambda\mu\zeta^2 + \lambda - \mu},$$

$$q(\zeta) = -\nu + \frac{3}{\zeta^2} - \frac{\lambda(-28\mu + 3\lambda + 4\lambda\mu\zeta^2 + \lambda^2\zeta^2)}{\lambda^2\zeta^4\mu + \lambda^2\zeta^2 - 6\lambda\mu\zeta^2 - \lambda + \mu} + \frac{-4\mu^2\nu + 4\nu\lambda\mu + 2\lambda^3}{(\lambda\mu\zeta^2 + \lambda - \mu)\lambda} + \frac{4\mu\nu}{\lambda\zeta^2 - 1}.$$

They were written in a form in which a partial expansion was made. We separated out the terms that define the singularity at zero as well as the terms that define the Alfvèn and cusp resonances. For them to be seen, we must compare the denominators with K_1 and K_2. Since we are interested in the expansions of the solutions near $\zeta = 0$, we consider the solutions of the equation in a circle centered at the zero point whose radius is equal to the distance to the other nearest singular point. An analysis of the singular points, except the zero point, is beyond the scope of this paper. We only note that one of the solutions has a logarithmic singularity at the resonance points, which is to be expected (Grossmann and Tataronis 1973; Tataronis and Grossmann 1973). The infinite point is an irregular singularity (Smirnov 1964) at which an oscillating behavior of the solutions similar to the behavior of the solutions of the Bessel equation might be expected. Additional, more cumbersome terms remain in the expressions for the coefficients. They give no singularities in the solutions, since they represent the contribution of C_3 to the radial equation.

Near zero, the equation can be approximately written as

$$\frac{d^2P}{d\zeta^2} + \frac{5}{\zeta}\frac{dP}{d\zeta} + \frac{3}{\zeta^2}P \approx 0.$$

Thus, we can see that the two linearly independent solutions have poles of the first and third orders at zero:

$$M(\zeta) \sim \frac{1}{\zeta}, \quad N(\zeta) \sim \frac{1}{\zeta^3}.$$

We seek solutions of the radial equation using an expansion in a power series of the argument ζ. For this purpose, we rewrite the radial equation as

$$A(\zeta)\frac{d^2P}{d\zeta^2} + B(\zeta)\frac{dP}{d\zeta} + C(\zeta)P = 0,$$

where the coefficients $A(\zeta)$, $B(\zeta)$, and $C(\zeta)$ are polynomials:

$$A(\zeta) = (\lambda - \mu)^2\zeta^2 - 2\lambda(\lambda - \mu)(\lambda - 4\mu)\zeta^4 + \lambda^2(-10\lambda\mu + 14\mu^2 + \lambda^2)\zeta^6 + 2\lambda^3\mu(\lambda - 4\mu)\zeta^8 + \lambda^4\zeta^{10}\mu^2,$$

$$B(\zeta) = 5(\lambda - \mu)^2\zeta - 2\lambda(\lambda - \mu)(4\lambda - 15\mu)\zeta^3 + \lambda^2(\lambda - 2\mu)(3\lambda - 28\mu)\zeta^5 + 2\lambda^3\mu(-17\mu + 3\lambda)\zeta^7 + 3\lambda^4\mu^2\zeta^9,$$

$$C(\zeta) = 3(\lambda - \mu)^2 - (\lambda - \mu)(\lambda^2 + 4\lambda\mu + \lambda\nu - \nu\mu)\zeta^2 - \lambda(\lambda - \mu) \times (\lambda - 6\mu)(3\lambda - 2\nu)\zeta^4 + \lambda^2(14\nu\lambda\mu - 38\nu\mu^2 - 13\lambda^2\mu - \nu\lambda^2 + 12\lambda\mu^2 + \lambda^3)\zeta^6 + \lambda^3\mu(-\lambda\mu + 12\nu\mu + \lambda^2 - 2\lambda\nu)\zeta^8 - \lambda^4\nu\zeta^{10}\mu^2.$$

Let us represent them as

$$A(\zeta) = \sum_{i=0}^{4} a_i \zeta^{2i+2}, \quad B(\zeta) = \sum_{i=0}^{4} b_i \zeta^{2i+1},$$

$$C(\zeta) = \sum_{i=0}^{5} c_i \zeta^{2i}.$$

We seek solutions using the series

$$M(\zeta) = \frac{1}{\zeta} \sum_{j\geq 0} w_j \zeta^{2j},$$

$$N(\zeta) = M(\zeta)\ln(\zeta) + \frac{1}{\zeta^3} \sum_{j\geq 0} u_j \zeta^{2j};$$

we construct standard recurrent procedures to determine these coefficients:

$$\sum_{i=0}^{\min(5,j)} w_{j-i}[(2j-2i-1)(2j-2i-2)a_i + (2j-2i-1)b_i + c_i] = 0,$$

$$\sum_{i=0}^{\min(5,j)} u_{j-i}[(2j-2i-3)(2j-2i-4)a_i + (2j-2i-3)b_i + c_i]$$

$$= -\sum_{i=0}^{\min(5,j-1)} w_{j-i-1}[(4j-4i-7)a_i + b_i], j \geq 0.$$

Here, we should set $a_5 = b_5 = 0$. Next, we normalize the solutions by choosing $w_0 = u_0 = 1$. The constructed series yield analytic functions near zero (Smirnov 1964). The convergence of the series extends to the other nearest singular point. Two linearly independent solutions in the circle centered at zero whose radius is equal to $\min(\zeta_A, \zeta_C)$ may be considered to have been constructed. In general, the radius of convergence is $\min(|\zeta_A|, |\zeta_C|)$. In using the solutions to describe the oscillations of a thin magnetic flux tube, we assume that the tube boundary does not reach the resonance points: $a < \min(r_A, r_C)$. Thus, the resonance points are cut off under the conditions considered here.

REFERENCES

1. H. Alfvèn and J. Carlqwist, Sol. Phys. (1967).
2. K. Appert, R. Gruber, and J. Vaclavik, Phys. Fluids **17**, 1471 (1974).
3. M. J. Aschwanden, Astrophys. J. **560**, 1035 (2001).
4. M. J. Aschwanden, L. Fletcher, C. J. Schrijver, *et al.*, Astrophys. J. **520**, 880 (1999).
5. P. M. Edwin and B. Roberts, Sol. Phys. **88**, 179 (1983).
6. W. Grossmann and J. Tataronis, Z. Phys. **261**, 203 (1973).
7. B. B. Mikhalyaev and A. A. Solov'ev, Pis'ma Astron. Zh. **30**, 307 (2004) [Astron. Lett. **30**, 268 (2004)].
8. V. M. Nakariakov, L. Ofman, and E. E. Deluca, Science **285**, 862 (1999).
9. L. Ofman and M. J. Aschwanden, Astrophys. J. **576**, L153 (2002).
10. E. N. Parker, *Cosmical Magnetic Fields: Their Origin and Their Activity* (Clarendon Press, Oxford, 1979; Mir, Moscow, 1982).
11. B. Roberts, in *Proceedings of SOHO13 "Waves, Oscillations and Small-Scale Transient Events in the Solar Atmosphere: A Joint View from SOHO and TRACE," Palma de Mallorka, Balearic Islands, Spain, 2003*, ESA SP **547**, 3 (2004).
12. M. S. Ruderman, Astron. Astrophys. **409**, 287 (2003).
13. M. S. Ruderman and B. Roberts, Astrophys. J. **577**, 475 (2002).
14. V. I. Smirnov, *A Course of Higher Mathematics* (Addison-Wesley, Reading, Mass., 1964; Nauka, Moscow, 1974), Vol. 3, Part 2.
15. A. A. Solov'ev, B. B. Mikhalyaev, and E. A. Kirichek, Fiz. Plazmy **28**, 758 (2002) [Plasma Phys. Rep. **28**, 699 (2002)].
16. A. A. Solov'ev, B. B. Mikhalyaev, and E. A. Kirichek, Fiz. Plazmy **29**, 1130 (2003) [Plasma Phys. Rep. **29**, 1049 (2003)].
17. H. S. Spruit, Sol. Phys. **75**, 3 (1982).
18. J. Tataronis and W. Grossmann, Z. Phys. **261**, 217 (1973).
19. T. Van Doorsselaere, J. Andries, S. Poedts, *et al.*, Astrophys. J. **606**, 1223 (2004).

Translated by V. Astakhov

Astronomy Letters, Vol. 31, No. 6, 2005, pp. 414–421. Translated from Pis'ma v Astronomicheskiĭ Zhurnal, Vol. 31, No. 6, 2005, pp. 465–473.

On the Periodicity of Energy Release in Solar Active Regions

T. B. Goldvarg[1], Yu. A. Nagovitsyn[2*], and A. A. Solov'ev[2]

[1] *Kalmyk State University, Elista, Kalmykia, Russia*

[2] *Pulkovo Astronomical Observatory, Russian Academy of Sciences, Pulkovskoe sh. 65, St. Petersburg, 196140 Russia*

Received May 28, 2003; in final form, December 21, 2004

Abstract—We investigate the periodic regimes of energy release on the Sun, namely, the recurrence of solar flares in active regions using the Solar Geophysical Data Journal on Hα flares from 1979 until 1981, which corresponds to the maximum of solar cycle 21. We obtained the following series of periods in the manifestation of flare activity by means of a correlation periodogram analysis, a self-similarity function, and a wavelet analysis: ∼1, 2, 3 h as well as ∼0.4, 1, 2, 5 days. We suggest a diffusive model for the quasi-periodic transfer of toroidal magnetic fields from under the photosphere to interpret the retrieved sequence of periods in the enhancement of flare activity. We estimated the typical spatial scales of the magnetic field variations in the solar convection zone: ∼17 000 km. © *2005 Pleiades Publishing, Inc.*

Key words: *oscillations, solar flares, magnetic field diffusion.*

INTRODUCTION

The oscillations of various solar plasma parameters, such as the magnetic field, density, temperature, the sizes of active structures, etc., are encountered in all layers of the solar atmosphere and probably have a common pattern. Determining the characteristic periods of the corresponding nonstationary processes in the solar atmosphere is the first step in finding the common formation mechanisms of the oscillations, since the equality of their values may be indicative of their relationship.

Observations of the Sun revealed pulsations of its emission in various wavelength ranges (see the review by Aschwanden 1987). Various types of quasi-periodic oscillations were found in sunspots through observations: the sunspot material (Gopasyuk 1981), the sunspot areas (Demchenko *et al.* 1985), the sunspot structure (Nagovitsyna 1990), the sunspot magnetic field strength (Nagovitsyn and Vyal'shin 1990; Bortsov *et al.* 1986), the intensity of the sunspot sources of radio emission (Gelfreikh *et al.* 2000), and the sunspot locations (Ikhsanov and Nagovitsyna 1990).

Many observations point to a relationship between oscillatory processes in the solar atmosphere and solar flares (Abramenko *et al.* 1982; Alikaeva 1989; Nagovitsyna and Nagovitsyn 2002). Coronal-loop oscillations in an active region were observed from the TRACE satellite (171 Å, 195 Å) in the ultraviolet immediately after a strong solar flare, suggesting that they are related to the shock wave from the flare. Various oscillation modes can also be excited in flare loops at the impulsive flare phase; the radial and balloon oscillations with periods of 1–30 s are known (see, e.g., Stepanov *et al.* 2004) to modulate the emission most effectively. A wavelet analysis of the emission from the solar flare of August 28, 1999, performed by Stepanov *et al.* (2004) revealed both these types of oscillations (radial and balloon oscillations with periods of $T \approx 2.5$ and 14 s, respectively). The temporal behavior of the oscillations allowed one to identify them with the interaction between two flare coronal loops and to diagnose the plasma parameters in both loops.

The periodicity in flare occurrence was analyzed by using global indices of solar activity. For example, a period of about 24 days was found by studying the time series of the daily number of Hα flares (Bai 1987; Temmer *et al.* 2004). Temmer *et al.* (2004) believe this process to be more likely related to a periodic emergence of magnetic flux from under the photosphere than to the solar rotation. However, since the fact that the flares from the entire solar disk rather than in specific active regions were considered in these papers, this explanation requires an additional study.

In this paper, we analyze the frequency of occurrence of flares in selected solar active regions. To determine the parameters of this process, we use a harmonic approach realized in this case using the method of a correlation periodogram analysis,

*E-mail: nag@gao.spb.ru

1063-7737/05/3106-0414$26.00

CPGA (Kopetskii and Kuklin 1971), a self-similarity function (Nagovitsyn 1992), and a wavelet analysis (Grosmann and Morlet 1984). The latter is now widely used to consider the various nonstationary phenomena on the Sun (see, e.g., Frick *et al.* 1997). Note that a quasi-hour periodicity in the manifestation of flare activity in individual active regions was first found by Kravchuk and Kasinskiĭ (1992) using harmonic methods.

In contrast to Kravchuk and Kasinskiĭ (1992), we expanded significantly the sample of events under study, which makes it possible to analyze the recurrence of flares on various time scales. In addition, the use of a number of methods for analyzing the time series is attributable to the nontrivial dynamics of the process, which, on the one hand, is not strictly periodic and, on the other hand, is represented by sparse data. To generalize the oscillation parameters, we compare the results obtained by using various approaches. All of this is presented in the first section of the paper. In the second section, we suggest a new diffusive model for the transfer of magnetic energy from under the solar photospheric layers, which allows the derived discrete series of periods to be described. In the conclusion, we summarize our main results.

OBSERVATIONS AND DATA ANALYSIS

We used the Solar Geophysical Data Journal on solar Hα flares for 1979–1981 to determine the occurrence periods of flares in active regions. This time interval corresponds to the maximum of solar cycle 21. We chose those regions in which the number of detected flares and subflares was larger than 50, which ensured statistically significant results of our analysis. Note that the 114 regions selected in this way differed in that the time between the first and the last detected flares in each of them was $\Delta T \sim$ 9–15 days, which allowed the long (daily) periods to be reliably determined. The periodicity of the flare process was analyzed by using data on the flare detection time, with the time of their highest brightness being taken as the latter: we studied the samples $f(t_i)$ that were the series of data on the number of flares on the chosen grid of equidistant times t_i, $i = 1, \ldots, m$, where $m = \Delta T/(t_2 - t_1)$. We processed $f(t_i)$ by using both a harmonic analysis, CPGA (Kopetskiĭ and Kuklin 1971), and nonharmonic methods.

In the CPGA method, the temporal process specified by its experimental values of $f(t_i)$ is approximated for a set of trial periods T_i by a function of the form

$$s(t_i) = A\cos(2\pi t_i/T) + B\sin(2\pi t_i/T) + C, \quad (1)$$

where A, B, C are the constants to be determined by the least-squares method. For each value of T, we calculate the correlation coefficient $R(T)$ between the original time series $f(t_i)$ and the series $s(t_i)$. The confidence of the harmonic $P(T)$ with period T, understood as the probability of a nonrandom deviation of $R(T)$ from zero, is defined by the relation (Kopetskiĭ and Kuklin 1971)

$$P(T) = 1 - (1 - R^2(T))^{m/2-1}. \quad (2)$$

Here, we chose the values of T that corresponded to the local maxima of the function $R(T)$ composed of the coefficients $R(T_i)$ with a confidence $P(T) \geq 0.9$.

Figures 1a and 1b show the occurrence histograms of daily and hourly periods for the chosen active regions. As we see, the distributions have maxima at periods of 1, 1.5, 2, 3, 10 h and 1, 2, 5 days.

Note that the process under study is represented by highly sparse observational data. In practice, if we are interested in the oscillations with periods of no less than several dozen minutes, the flare activity is described by a binary series composed of ones (a flare was detected) and zeros (no flare was detected). Therefore, we also used the self-similarity function, which was used previously to study this kind of event sequences (Nagovitsyn 1992). In this approach, the series $f(t_i)$ is used to construct the self-similarity function, an analogue of the autocorrelation function, which is an average similarity of $f(t_i)$ with respect to itself when shifted by a time interval T. The Gauer similarity factor is used as a measure of similarity: $g_{ij} = S_{ij}/W_{ij}$ (Kim *et al.* 1989) for the elements of the series $f(t_i)$ and $f(t_j) = f(t_i + T)$. Here, S_{ij} for the binary data is specified in the form

$$S_{ij} = \begin{cases} 1, & f(t_i) = f(t_j) \\ 0, & f(t_i) \neq f(t_j). \end{cases}$$

The system of information weights W_{ij}, which expresses a moderate confidence in the information, is chosen by the following criteria: if $f(t_i) = f(t_j) = 0$, then it is assumed that a flare might not be detected at a given time, therefore, $W_{ij} = 0$; if $f(t_i) = f(t_j) = 1$, then $W_{ij} = 2$; for $f(t_i) \neq f(t_j)$, we assume that the event is statistically significant and $W_{ij} = 1$. Subsequently, the self-similarity function is calculated:

$$G(T) = \frac{1}{t_m - T - 1} \sum_{i=0}^{t_m - T} g_{i,i+T},$$

and periodicities can be searched for by applying harmonic methods (we used the CPGA method) to it.

The results of the applied procedure are shown as histograms (Figs. 1c and 1d) similar to those in Figs. 1a and 1b. We see that the following characteristic periods are found: 1, 2, 10 h and 1, 2, 3, and

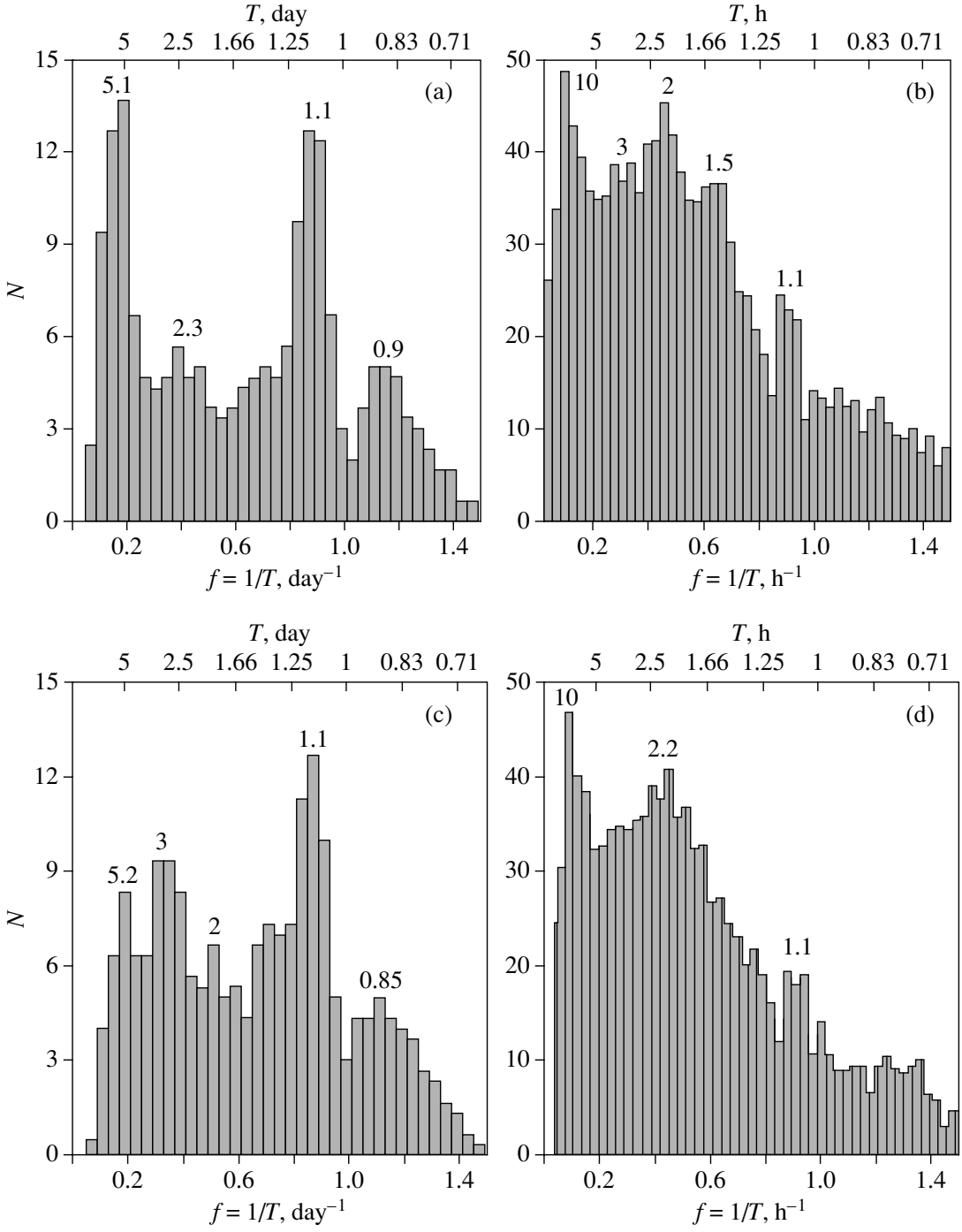

Fig. 1. Occurrence histograms of the quasi-periods obtained by using the CPGA method (a, b) and the self-similarity function (c, d).

5 days, in good agreement with the results of our direct harmonic (CPGA) analysis.

It should be noted that the oscillations under study were initially assumed to be stationary in the methods used above, which may not be a realistic assumption. At present, a wavelet analysis is widely used to analyze time sequences with deviations from strict periodicity (Astaf'eva 1996). It is suitable for studying such nonstationary processes, since the basis is formed from wavelets that are well localized in both frequency and time of the functions, and this allows the current peculiarities of the signal to be successfully revealed. To analyze the series under study, we chose a real MHAT wavelet, $\psi(t) =$

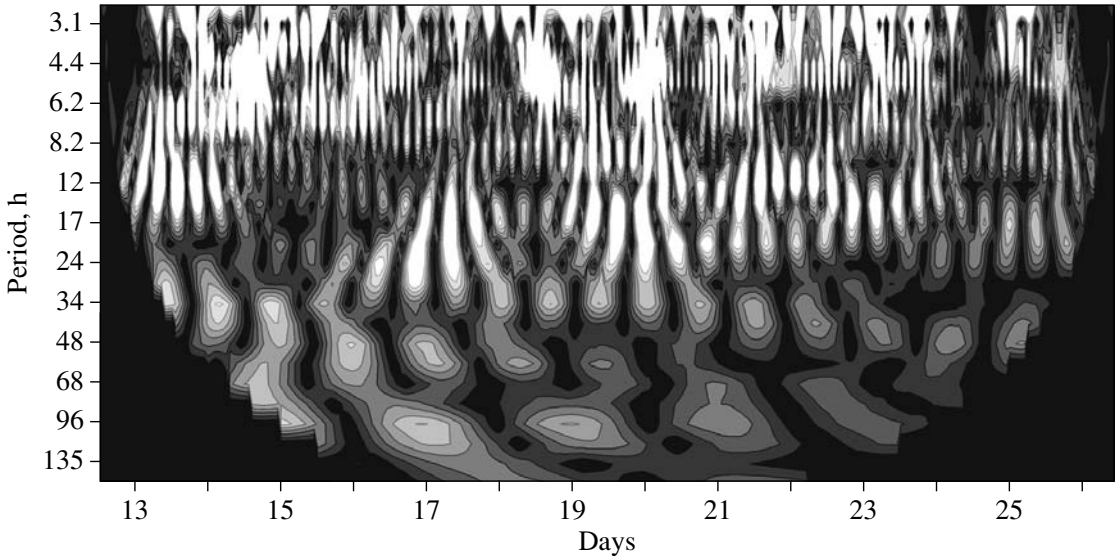

Fig. 2. Variation in the magnitude of the coefficients of the real part of the wavelet transform obtained when analyzing the flare-occurrence oscillations in NOAA no. 16224 (a Morlet wavelet was used).

$(1-t^2)\exp(-t^2/2)$, and a complex Morlet wavelet, $\psi(t) = \exp(i\omega_0 t - t^2/2)$, where ω_0 is the number of extrema of the basis wavelet. Note that the Morlet wavelet has good signal frequency localization, while the MHAT wavelet is more suitable for describing complex signals and is not severely limited by the length of the series under study. The basis wavelet is used to construct an integral wavelet transform of the sequence $f(t_i)$ under study:

$$W_\psi(a,b) = \frac{1}{\sqrt{a}} \int_{-\infty}^{\infty} f(t)\psi^*\left(\frac{t-b}{a}\right)dt, \qquad (3)$$

where ψ^* is the complex conjugate (to ψ) function, $a = 2^q$, $q = 1, \ldots, p$ is the scale factor that determines the dilation of the basis wavelet, and p is chosen so that 2^p does not exceed the number of elements m in the original sample. The translation parameter b is used to slide the wavelet $\psi(t)$ along the length of the realization, i.e., $b = 1, \ldots, m$. By performing the wavelet transforms (3), we find a correlation between the series $f(t_i)$ being analyzed and the chosen wavelet $\psi(t)$ when dilating and sliding the latter along the length of the realization. As a result, a two-dimensional set of coefficients $W_\psi(a,b)$ is formed.

Figure 2 illustrates the projection of the image of the surface $|W_\psi(a,b)|$ obtained by using the real part of the Morlet wavelet onto the ab plane for the active region NOAA no. 16224 that crossed the solar disk from August 13 through August 25, 1979.

To get the overall picture of the period distribution, we constructed the occurrence histograms of flare periods in all of the active regions under consideration by using the MHAT (Figs. 3a, 3b) and Morlet (Figs. 3c, 3d) wavelets. As we see from these figures, the occurrence of periodic components at 1, 2, 3 h as well as 1 and 2 days is enhanced.

Note that the real MHAT wavelet (Fig. 3a) reveals a period of ~5 days, which was also found by the CPGA method (Figs. 1a, 1c). However, the histogram based on the complex Morlet wavelet (Fig. 3d) does not show this period, because the wavelet under consideration is limited by the length of the sample. At the same time, the maximum in the histogram (Fig. 3d), which corresponds to 47 min, is too small to be determined by other methods.

Thus, our analysis reveals a periodicity in the manifestation of solar flare activity that is expressed in the form of two discrete series: hourly (~1, 2, 3, 10 h) and daily (~1, 2, 5 days). The 10-h period is far from the other periods of the hourly sequence, occupying an intermediate position; therefore, it can be attributed to both the first and the second (daily) series.

The values of the hourly series found are close to the periods of the oscillations of sunspot fragments (Nagovitsyna and Nagovitsyn 2002), the intensity of the sunspot radio emission sources (Gelfreikh *et al.* 2000), the latitudinal–longitudinal oscillations of the sunspot locations (Ikhsanov and Nagovitsyna 1990), the sunspot structure (Nagovitsyna 1990), and the sunspot magnetic field oscillations (Nagovitsyn and Vyal'shin 1990; Bortsov *et al.* 1986). The values of the daily series of periods agree with those of Gopasyuk (1981) and Nagovitsyna and Nagovitsyn (1989).

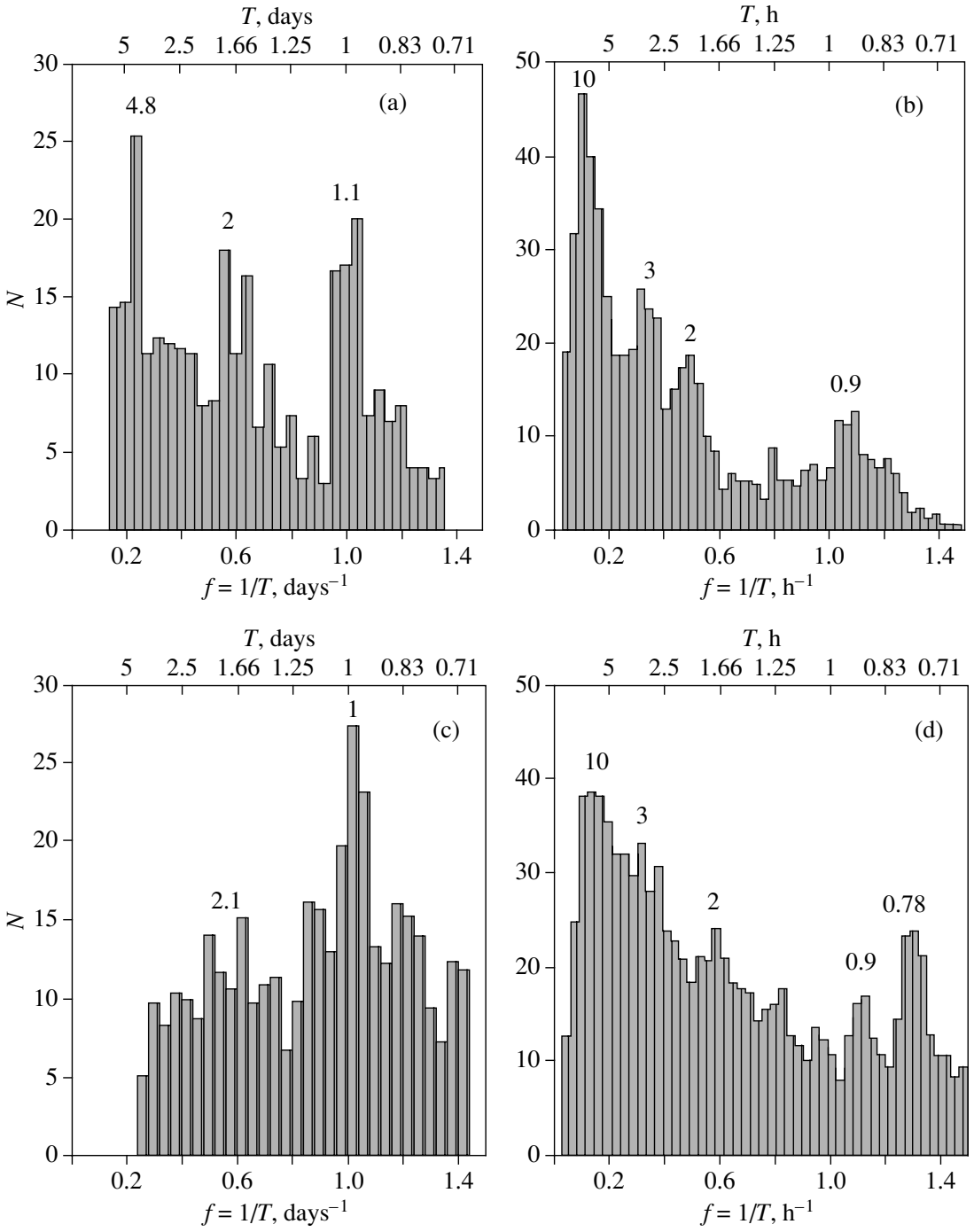

Fig. 3. Occurrence histograms of the quasi-periods obtained by a wavelet analysis (we used the MHAT wavelet to construct Figs. 1a and 1b and the Morlet wavelet to construct Figs. 1c and 1d).

Since we performed no prior classification of solar flares by morphological, spectral, or other properties, the series of periods found should be associated only with nonuniform overall energy release in solar flares. Below, we suggest a model based on the particular solution of the diffusion equation for a magnetic field nonuniformly distributed in space at the initial time in terms of which the periodicity found can be explained.

DIFFUSIVE MAGNETIC-FIELD TRANSFER INTO THE SOLAR ATMOSPHERE

There is no doubt that the solar flares are of a magnetic nature. Their appearance is associated with the emergence of strong magnetic fields on the solar surface. Therefore, some physical process of nonuniform quasi-periodic transfer of magnetic energy from under the photosphere into the upper solar layers must be

responsible for the periodicity found in the occurrence of solar flares of various scales and powers. One possible mechanism behind this emergence of magnetic flux is the diffusion of a magnetic field that is initially nonuniformly distributed in a medium with a finite effective conductivity. The magnetic field transfer to the solar surface is commonly associated with the rise of flux tubes from under the photospheric layers due to magnetic buoyancy (Parker 1979). This process plays an important role in delivering magnetic energy to the solar surface, but the rise of individual magnetic loops is a local effect and does not lead to the release of magnetic flux of the entire flux tube; the bulk of its length remains submerged in the photosphere and the convection zone. Only the magnetic field diffusion relative to the material can provide the emergence of the entire magnetic flux tube in the solar atmosphere.

Let us consider an axisymmetric magnetic field in a spherical (r, θ, φ) coordinate system: $\mathbf{B} = (B_\theta(r,\theta,t), B_\varphi(r,\theta,t), B_r(r,\theta,t))$, where r is the distance to the solar center. The characteristic time scales of the processes considered in our problem are appreciably longer than the time it takes for a mechanical equilibrium to be established between the plasma and the magnetic field. Therefore, the field diffusion process may be assumed to be quasi-static: since the system passes through a continuous sequence of equilibria, the magnetic force $\frac{1}{4\pi}[\mathrm{curl}\mathbf{B}, \mathbf{B}]$ is balanced by the gas pressure gradient ∇P and the gravity $\rho\nabla U$ at any instant in time. To describe this quasi-static process, it will suffice to use only the induction equation,

$$\frac{\partial \mathbf{B}}{\partial t} = \mathrm{curl}[\mathbf{VB}] + v_m \Delta \mathbf{B} \qquad (4)$$

and the equations for a solenoidal magnetic field and for flows of an incompressible fluid, $\mathrm{div}\mathbf{B} = 0$ and $\mathrm{div}\mathbf{V} = 0$, from the entire system of MHD equations.

Since the plasma in the convection zone is in a state of turbulent mixing, the turbulent diffusion coefficient should be meant by v_m in Eq. (4): $v_m \approx (V_T \times l)/3$, where V_T and l are the characteristic plasma velocity and mixing scale length, respectively (Priest 1982). If the solar granulation parameters are used in the above formulas, then $v_m \approx 2 \times 10^{12}$ cm^2 s^{-1}. Below, we use this magnetic viscosity for our numerical estimates. Since in this case we are interested in relatively short time intervals, we set the regular flow velocities in Eq. (4) equal to zero, $\mathbf{V} = 0$, by ignoring, in particular, the effects related to differential rotation. In this case, Eq. (4) is reduced to a diffusion equation in component form:

$$\frac{\partial B_\theta}{\partial t} = \frac{v_m}{r}\frac{\partial}{\partial r}\left(\frac{\partial}{\partial r} r B_\theta - \frac{\partial}{\partial \theta} B_r\right), \qquad (5)$$

$$\frac{\partial B_r}{\partial t} = -\frac{v_m}{r\sin\theta}\frac{\partial}{\partial \theta}\left[\frac{\sin\theta}{r}\left(\frac{\partial}{\partial r} r B_\theta - \frac{\partial}{\partial \theta} B_r\right)\right],$$

$$\frac{\partial B_\varphi}{\partial t} = \frac{v_m}{r}\frac{\partial^2}{\partial r^2}(r B_\varphi) + \frac{v_m}{r}\frac{\partial}{\partial \theta}\left(\frac{1}{r\sin\theta}\frac{\partial}{\partial \theta}\sin\theta B_\varphi\right). \qquad (6)$$

The flare energy release is commonly associated with the emergence of strong toroidal magnetic fields in the solar atmosphere. As we see from Eqs. (5) and (6), the diffusion of the field B_φ is independent of the other components of the vector $\mathbf{B}$; therefore, it will suffice to consider the case of $B_\theta = B_r = 0$. We use the dimensionless variables $\tilde{r} = r/r_0$ and $\tilde{t} = t/t_\mathrm{d}$, where r_0 is the typical spatial scale of the field variations, and $t_\mathrm{d} = r_0^2/v_m$ is the skin time on this scale. Equation (6) has a solution of the form

$$B_\varphi(\tilde{r}, \tilde{t}) = B_0 \frac{\sin\theta}{\tilde{r}} \sum_k M_k(\tilde{r}, \tilde{t}) P_k'(\cos\theta), \qquad (7)$$

where $B_0 = \mathrm{const}$, $k = 0, 1, \ldots$ $P_k'(\cos\theta)$ is the derivative of the Legendre polynomial with respect to its argument $\cos\theta$, and the function $M_k(\tilde{r}, \tilde{t})$ satisfies the scalar diffusion equation

$$\frac{\partial M_k}{\partial \tilde{t}} = \frac{\partial^2 M_k}{\partial \tilde{r}^2} - k(k+1)\frac{M_k}{\tilde{r}^2}. \qquad (8)$$

According to Hale's rule, the toroidal magnetic fields responsible for the formation of active regions on the Sun change their polarity on the equator, having opposite directions in the Northern and Southern Hemispheres in each cycle. Since this condition is satisfied for the even harmonics of series (8), below we assume that $k = 2, 4, 6 \ldots$. Equation (8) has a solution of the form (Solov'ev and Kirichek 2004)

$$M_k(\tilde{r}, \tilde{t}) = C_k \sqrt{\frac{\tilde{r}}{\mu_k^2 + (\tilde{t} - \tilde{t}_{0,k})^2}} \times \exp\left(\frac{-(\tilde{t} - \tilde{t}_{0,k})\tilde{r}^2/4}{\mu_k^2 + (\tilde{t} - \tilde{t}_{0,k})^2}\right) \times J_{(k/2+1/4)}\left(\frac{\mu_k \tilde{r}^2/4}{\mu_k^2 + (\tilde{t} - \tilde{t}_{0,k})^2}\right). \qquad (9)$$

Here, $J_{(k/2+1/4)}$ is the Bessel function of the first kind, C_k are arbitrary amplitudes, and μ_k and $\tilde{t}_{0,k}$ are dimensionless free parameters (constants). Solution (9), whose validity can be easily verified by directly substituting it in (8), describes the oscillatory regime of diffusion, because the time appears (quadratically!) in the argument of the alternating Bessel function. Thus, solution (9) describes a soliton-like wave packet. Figure 4 shows the principal harmonic of the toroidal magnetic field ($k =$

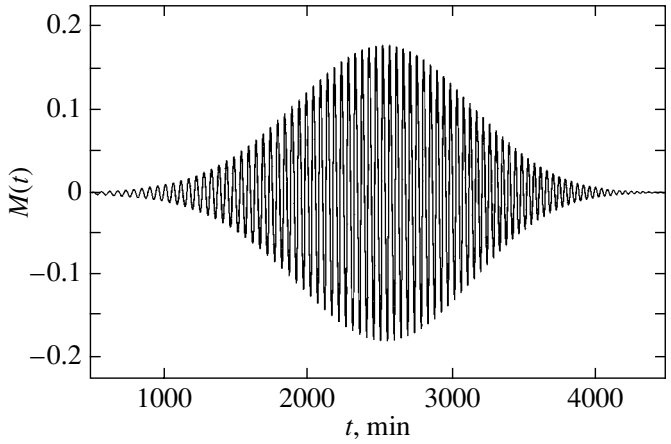

Fig. 4. The second harmonic of the toroidal magnetic field on the solar surface ($r = R$) at $r_0 = 17\,000$ km and $\mu_2 = 0.5$.

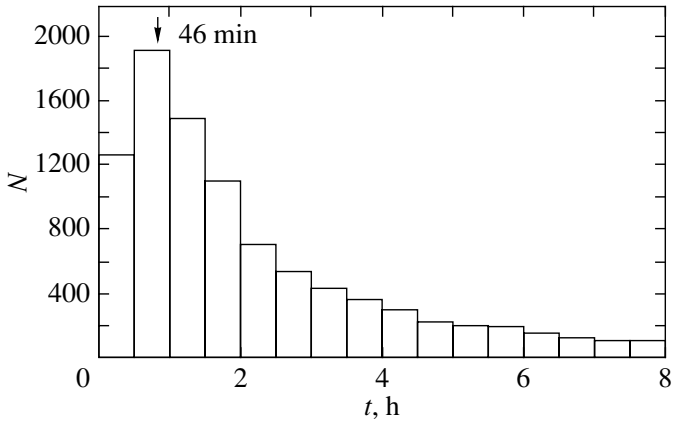

Fig. 5. Recurrence in flare activity.

2) on the solar surface ($r = R$) at $r_0 = 17\,000$ km (the mesogranulation scale length), $\mu_2 = 0.5$, and $\tilde{t}_{0,2} = 1$. For the amplitude coefficient in (9), we took $C_2 = \exp\left(-\dfrac{R^2}{4r_0^2}\right)$. The value of ΔT between the two successive maxima in Fig. 4 is about 46 min, which corresponds to the maximum of the histogram in Fig. 5. Figure 5 shows all of the time intervals between the successive flares. The found sequence of periods from 46 min to 5 days can be obtained by varying only the characteristic scale r_0 within the range from 17 thousand to 30 thousand km (1 h—18 thousand km, 2 h—20 thousand km, 3 h—22 thousand km, 10 h—25 thousand km, 1–5 days—about 30 thousand km).

CONCLUSIONS

Our analysis of the periodicity in the occurrence of solar flares in an active region by various methods (CPGA, a self-similarity function, and a wavelet analysis) has yielded consistent results, which argues for the reliability of the values found. We detected two series of quasi-periods: hourly (about one, two, and three hours) and daily (about half a day, one, two, and five days). In addition, we revealed a maximum in the occurrence of flares of the 47-min period using a Morlet wavelet.

To explain the periods found, we suggest a new solution of the magnetic-field diffusion equation. This allows us to model the discrete transfer of toroidal magnetic-field energy from the convection zone into the photosphere in the form of alternating magnetic layers with a characteristic scale of ~17 000 km. The characteristic scale calculated in this model corresponds to the mesogranulation sizes in the solar photosphere and most likely reflects the peculiarities of the magnetic-field generation in the convection zone.

ACKNOWLEDGMENTS

We wish to thank V.V. Krasinskiĭ and Yu.G. Kopylova for their helpful discussions and remarks. This work was supported by the Astronomy program of the Ministry of Science and Industry (subject 1105), the Nonstationary Phenomena in Astronomy program of the Presidium of the Russian Academy of Sciences, the Solar Wind: Generation and Interaction with the Earth and Other Planets program of the Russian Academy of Sciences, and the INTAS (grant nos. 2000-00543, 2000-00752, and 2001-00550 (in part)).

REFERENCES

1. V. I. Abramenko, I. I. Eryushev, and L. I. Tsvetkov, Izv. Krym. Astrofiz. Obs. **65**, 87 (1982).
2. K. V. Alikaeva, *Physics of Solar Plasma* (Nauka, Moscow, 1989) [in Russian].
3. M. J. Aschwanden, Sol. Phys. **111**, 113 (1987).
4. N. M. Astaf'eva, Usp. Fiz. Nauk **166**, 1145 (1996) [Phys. Usp. **39**, 1085 (1996)].
5. T. Bai, Astrophys. J. **318**, 85 (1987).
6. V. V. Borzov, G. F. Vyal'shin, and Yu. A. Nagovitsyn, Contrib. Astron. Obs. Skalnate Pleso **16**, 75 (1986).
7. B. I. Demchenko, G. S. Minasyants, N. G. Makarenko, and S. O. Obashev, Astron. Tsirk. **1360**, 3 (1985).
8. I. I. Eryushev and L. I. Tsvetkov, Izv. Krym. Astrofiz. Obs. **65**, 87 (1982).
9. P. Frick, S. L. Baliunas, D. Galyagin, *et al.*, Astrophys. J. **483**, 426 (1997).
10. G. B. Gelfreikh, Yu. A. Nagovitsyn, and K. Shibasaki, in *JENAM-2000* (GEOS, Moscow, 2000), p. 119.
11. S. I. Gopasyuk, Izv. Krym. Astrofiz. Obs. **54**, 108 (1981).
12. A. Grosmann and J. Morlet, SIAM (Soc. Ind. Appl. Math.) J. Math. Anal. **15**, 723 (1984).
13. R. N. Ikhsanov and E. Yu. Nagovitsina, Soln. Dannye **4**, 77 (1990).
14. J.-O. Kim, Ch. U. Muller, U. R. Klekk, *et al., Factor, Discriminant, and Cluster Analysis* (Finansy i Statistika, Moscow, 1989).
15. M. Kopetskiĭ and G. V. Kuklin, Issled. Geomagn. Aéronom. Fiz. Solntsa **2**, 167 (1971).
16. P. F. Kravchuk and V. V. Kasinskiĭ, Issled. Geomagn. Aéronom. Fiz. Solntsa **99**, 80 (1992).
17. Yu. A. Nagovitsyn and G. F. Vyal'shin, Soln. Dannye, No. 9, 91 (1990).
18. Yu. A. Nagovitsyn, in *Spatial–Temporal Aspects of Solar Activity* (Fiz.-Tekh. Inst. im Ioffe Ross. Akad. Nauk, St. Petersburg, 1992), p. 197 [in Russian].
19. E. Yu. Nagovitsyna, Soln. Dannye, No. 5, 79 (1990).
20. E. Yu. Nagovitsyna and Yu. A. Nagovitsyn, Pis'ma Astron. Zh. **28**, 140 (2002) [Astron. Lett. **28**, 121 (2002)].
21. E. Yu. Nagovitsyna and Yu. A. Nagovitsyn, Soln. Dannye **6**, 93 (1989).
22. E. N. Parker, *Cosmical Magnetic Fields: Their Origin and Their Activity* (Clarendon Press, Oxford, 1979; Mir, Moscow, 1982), p. 608.
23. E. R. Priest, *Solar Magnetohydrodynamics* (Reidel, Dordrecht, 1982; Mir, Moscow, 1985), p. 589.
24. A. A. Solov'ev and E. A. Kirichek, *Diffusion Theory of Solar Magnetic Cycle* (Kalmytsk. Gos. Univ., 2004), p. 181.
25. A. V. Stepanov, Yu. G. Kopylova, Yu. T. Tsap, *et al.*, Pis'ma Astron. Zh. **30**, 530 (2004) [Astron. Lett. **30**, 480 (2004)].
26. M. Temmer, A. Veronig, J. Rybak, *et al.*, Sol. Phys. **221**, 325 (2004).

Translated by V. Astakhov

Astronomy Letters, Vol. 31, No. 6, 2005, pp. 422–426. Translated from Pis'ma v Astronomicheskiĭ Zhurnal, Vol. 31, No. 6, 2005, pp. 474–479.

Spectral Variations and Long-Period Intensity Variations of Auroral Kilometric Radiation from INTERBALL-2 Satellite Measurements

M. M. Mogilevsky[1*], I. L. Moiseenko[1], and J. Hanasz[2]

[1] *Space Research Institute, Russian Academy of Sciences, Profsoyuznaya ul. 84/32, Moscow, 117810 Russia*

[2] *Space Research Center, Polish Academy of Sciences, ul. Rabiańska 8, 87-100 Toruń, Poland*

Received November 12, 2004

Abstract—A statistical analysis of the auroral kilometric radiation (AKR) measurements in the POLRAD experiment on the INTERBALL-2 satellite has revealed a dependences of the size and location of the AKR generation region on geomagnetic activity: the generation region rises upward and expands with increasing magnetic disturbances. Based on our two-year measurements, we found seasonal AKR intensity variations: the AKR maximum and minimum are observed in winter and summer, respectively. The seasonal variations and the dependence of the spectrum on geomagnetic activity are assumed to have a common physical nature—the background-plasma density variations in the region of the AKR source attributable to plasma flows from the ionosphere into the magnetosphere. © *2005 Pleiades Publishing, Inc.*

Key words: *radio emission, cyclotron maser, magnetosphere, ionosphere.*

INTRODUCTION

The Auroral Kilometric Radiation (AKR), which was first detected by Benediktov *et al.* (1965) on the ELEKTRON satellite, is the most intense radio emission generated in the Earth's magnetosphere; according to Gurnett (1974), its total intensity can reach 10^7–10^9 W. The main AKR generation mechanism is the cyclotron maser instability (Wu and Lee 1979) that grows in regions with a reduced plasma density in the auroral magnetosphere, Calvert's cavity, where the electron plasma frequency is lower than the electron gyrofrequency (Calvert 1987). The fluxes of energetic electrons injected from the magnetospheric tail into the inner regions are the AKR energy source; therefore, the AKR intensity depends on geomagnetic activity, which was pointed out in the first publications by Benediktov *et al.* (1968). Subsequent studies showed that the AKR is very sensitive to variations in geomagnetic activity and could be used to determine the onset of a magnetospheric substorm (Voot *et al.* 1977; Kurth and Gurnett 1998).

Subsequent theoretical studies (Pritchet *et al.* 1999) and FAST satellite measurements in the AKR source with a high time resolution (Ergun *et al.* 2000) showed that the electron distribution function in the AKR source has $\partial f/\partial v$ in both transverse and longitudinal velocities (a horseshoe distribution). This distribution leads to more efficient energy transfer from electrons to waves and allows the high AKR amplitude observed in the experiment to be explained.

Electromagnetic radiations similar in nature to the AKR are typical of all planetary magnetospheres. Such radiations were detected on other planets of the Solar system with fairly strong magnetic fields (Zarka 1998). At present, these radiations are intensively studied in connection with the investigation of processes in the magnetospheres of Jupiter and Saturn (see, e.g., Zaĭtsev *et al.* 2003).

A seasonal dependence of the AKR intensity was first revealed by GEOTAIL satellite measurements (Kasaba *et al.* 1997). Subsequent studies on the Akebono (EXOS-D), POLAR, IMAGE, and INTERBALL-2 satellites have shown the existence of a marked difference between the AKR spectra in summer and winter: in summer, the upper frequency limit shifts toward the lower frequencies (Kumamoto and Oya 1998; Kumamoto *et al.* 2003; Green *et al.* 2004; Olson *et al.* 2004).

In this paper, we analyze the statistical characteristics of the location of the AKR generation region as a function of geomagnetic activity and the long-period variations of the AKR intensity measured in the POLRAD experiment on the INTERBALL-2 satellite; we also compare our results with those of other experiments. We interpret our results concerning the dynamics of the generation region and the intensity variations in terms of a single mechanism—variations of the ionospheric plasma flows from the ionosphere into the magnetosphere and, as a result,

[*] E-mail: mogilevsky@romance.iki.rssi.ru

1063-7737/05/3106-0422$26.00

violation of the AKR generation conditions at various altitudes in the auroral magnetosphere.

EXPERIMENTAL DATA AND THEIR ANALYSIS

The POLRAD experiment, which was designed for spectropolarimetric measurements of electromagnetic fields in the frequency range 4 kHz–2 MHz with a frequency resolution of 4.096 kHz, was carried out on board the INTERBALL-2 satellite (Galeev *et al.* 1996). This experiment was prepared by Polish researchers with the participation of Russian scientists (Hanasz *et al.* 1998). The INTERBALL-2 orbit was chosen in such a way that the spacecraft moved for a relatively long time over the same L-shell in the apogee region (Nazirov and Prokhorenko 1998). This allowed measurements to be performed under approximately identical radiation reception conditions for two to three hours in the same orbit. In this paper, we used measurements obtained in the frequency range up to 1 or 2 MHz to trace the variation in both the lower and upper limits of the AKR frequency range. For our statistical analysis, we selected data of two years of measurements (from October 1996 through August 1998). To find the patterns of AKR intensity variations and the dynamics of the frequency limits of the generation region, we constructed average AKR spectra in each observing session; the averaging was performed over 280–1700 spectra measured onboard the satellite (the number of measured spectra was determined by the session duration and the operating mode of the instrument). Subsequently, we selected the spectra depending on geomagnetic activity. As a characteristic of geomagnetic activity, we chose the *Kp* index.[1] The spectra were subsequently averaged over a month of measurements for each *Kp* value separately. The derived database was used in our analysis whose results are presented below.

Spectral Variations

Figure 1 shows the average AKR spectra constructed from the measurements in December 1997 for quiet and disturbed geomagnetic conditions. The signal below 20–30 kHz is the whistler mode of the radiation that is not analyzed in this paper. The AKR intensity increases by more than 1.5 orders of magnitude with increasing geomagnetic activity, while its lower and upper frequency limits shift toward the low frequencies by ~150 and ~100 kHz, respectively. It should be noted that the spectral shape also changes: under disturbed conditions, the width of the spectrum decreases in comparison with the spectrum under quiet conditions, while the spectral peak shifts toward the low frequencies. This change in the spectrum implies that the AKR source displaces to the higher altitudes: the lower and upper boundaries of the source rise to 300–350 and ~2500 km, respectively. Thus, our analysis of the AKR spectral variations with geomagnetic conditions reveals that the generation region rises upward along the magnetic field line and expands under disturbed magnetic conditions.

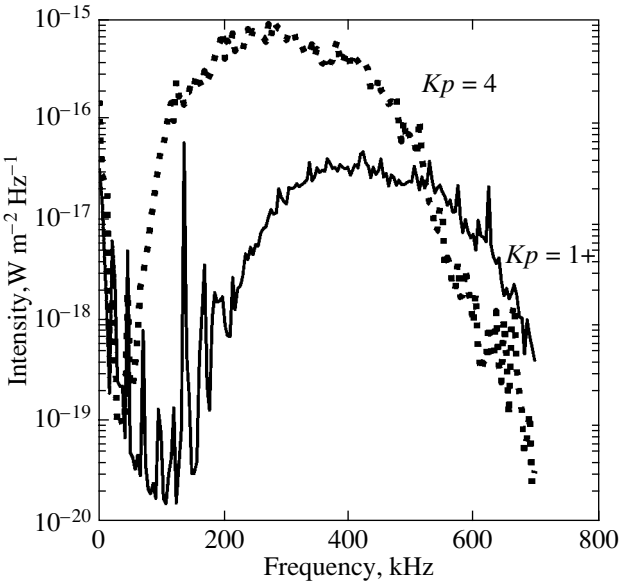

Fig. 1. AKR spectra (averaged over one month) constructed from the measurements in December 1997 with the POLRAD instrument onboard the INTERBALL-2 satellite; the solid and dotted curves represent the AKR spectra under quiet ($Kp = 1+$) and disturbed ($Kp = 4$) geomagnetic conditions, respectively.

Another example of the AKR spectral variations in October 1997 is shown in Fig. 2. In this case, the lower frequency limit also shifts to the low-frequency range. However, in contrast to the previous case, the width of the spectrum increases, its shape remains virtually unchanged, the position of the frequency peak does not change, and the upper frequency limit slightly shifts toward the high frequencies. These spectral variations correspond to an expansion of the generation region: the upper boundary rises to 1500 km, while the lower boundary sinks to ~200 km. It should be noted that such spectral variations are encountered much more rarely than those shown in Fig. 1.

[1] The *AE* index is more suitable for studying auroral phenomena. However, the available databases contain no values of this index for the second half of 1996. Therefore, we used the *Kp* index to keep a longer series of measurements and a uniform approach to data analysis

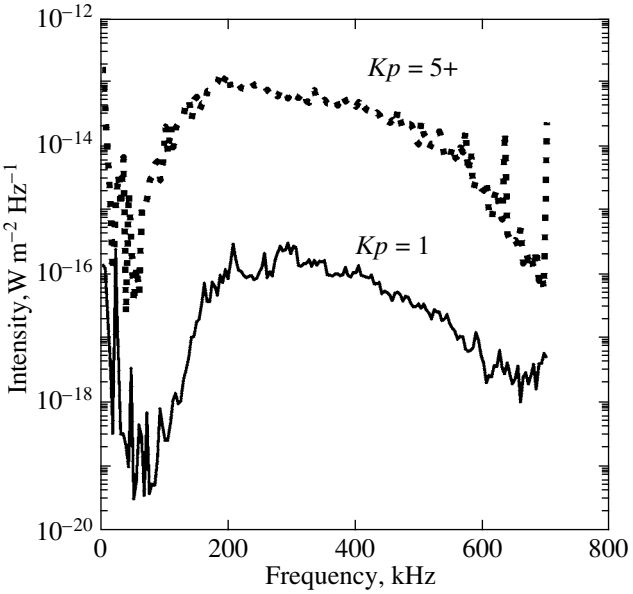

Fig. 2. Average AKR spectra in October 1997 under various geomagnetic conditions (similar to Fig. 1); the solid and dotted curves are shown for $Kp = 1$ and $Kp = 5+$, respectively.

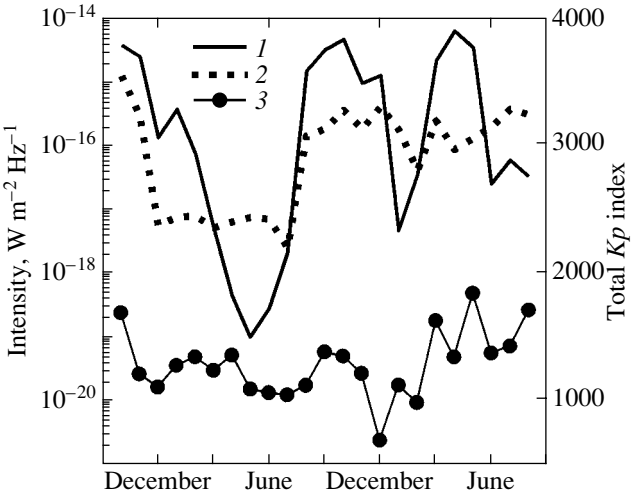

Fig. 3. Variations in the average AKR intensity and total monthly *Kp* indices during two years (October 1996–August 1998); *1* and *2*—the AKR intensities under quiet geomagnetic conditions ($Kp < 1$) for frequencies of 300 and 50 kHz, respectively (left scale); *3*—the total *Kp* indices (right scale).

Long-period AKR Intensity Variations

Using the database of average AKR intensities for two years of measurements, we analyzed the AKR intensity variations over this period. Figure 3 shows the variations in the average AKR intensity at frequencies of 300 kHz (near the spectral peak) and 50 kHz (near the lower frequency limit of the spectrum). In analyzing the time dependence of the AKR intensity, we used the measurements in one frequency band. The average intensities in several close frequency bands (not shown) differ only slightly from the presented results. We used the measurements made under quiet geomagnetic conditions ($Kp < 1$). Intensity variations on a timescale of several months are observed in both frequency bands and, in general, are similar. However, the maximum of the amplitude of the average intensity variations at 300 kHz is an order of magnitude higher. We discuss the cause of this difference below. Figure 3 also shows the total monthly *Kp* indices for comparison with geomagnetic activity. It may be concluded from this comparison that a number of peculiarities in the behavior of the AKR variations cannot be caused by variations in geomagnetic activity. Therefore, we analyzed the conditions of the measurements related to the change in the relative positions of the INTERBALL-2 satellite and the AKR source.

Separating the Source's Variations

The INTERBALL-2 measurements were made at an altitude of $2–3R_\odot$, i.e., close to the AKR generation altitudes. Therefore, the signal reception conditions on the satellite also depended on the relative positions of the satellite and the AKR source (Hanasz *et al.* 1998). To separate the source's variations in explicit form, we must "clean" the results of the measurements from the effects of the reception conditions. According to previous works (in particular, Hanasz *et al.* 2003), the radiation source is, in general, located near 22 MLT (Magnetic Local Time). Taking into account the orbital evolution law (Nazirov and Prokhorenko 1998), we can fit the dependence of the results of the satellite measurements on the conditions in the source and on the satellite position as follows:

$$I = I_0(Kp) - M(Kp)[1 - \cos(2\pi t/T_\mathrm{p} + \phi_\mathrm{p})] \times [1 - \cos(2\pi t/T_i + \phi_i)], \quad (1)$$

where $I_0(Kp)$ is the AKR intensity, which depends only on the particle flux from the magnetotail and does not depend on ionospheric particles; $M(Kp)$ is the dependence of the "variable" part of the AKR on the particle flux; T_p and ϕ_p are the period and phase of the satellite motion relative to the radiation source; T_i and ϕ_i are the period and phase of the sought long-period variations; and t is the current time.

The first term in Eq. (1) does not depend on the influence of the ionosphere. The second term in Eq. (1)

includes the dependence on both the fluxes of energetic particles from the magnetotail and the rising ionospheric electrons.

The values of T_p and ϕ_p were determined from the motion of the satellite with respect to the radiation source (Moiseenko 2004). The parameters I_0, $M(Kp)$, T_i, and ϕ_i were chosen in such a way that the model curve was close to the results of the measurements (see Fig. 4): Kp, $Kp/4$, 12, and 0.5236, respectively. Substituting these value in (1) yields the following formula for the AKR intensity variations:

$$I = Kp - (Kp/4)[1 - \cos(2\pi t/8.5 - 2.217)] \quad (2)$$
$$\times [1 - \cos(2\pi t/12 - 0.5236)].$$

An analysis of (2) shows that the source's intensity variations occur periodically during the year, the period is 12 months, the radiation is at a maximum in December and at a minimum in June.

EXPERIMENTAL RESULTS

The presented experimental results can be summarized as follows:

(1) The results of previous studies were confirmed: as geomagnetic activity grows from $Kp = 1$ to 4, the AKR intensity increases by one or two orders of magnitude;

(2) The AKR spectrum varies with geomagnetic activity: in disturbed periods, the lower frequency limit shifts to the low-frequency range by 100–200 kHz, and the upper frequency limit shifts more often toward the low frequencies; however, in several cases, the inverse shift toward the high frequencies is observed (see Fig. 2);

(3) The seasonal AKR intensity variations were calculated: the radiation is at a maximum in winter and at a minimum in summer.

DISCUSSION

Green *et al.* (2004) and Olson *et al.* (2004) showed that the AKR spectrum varies seasonally: in summer, the radiation is not observed at high frequencies and becomes more intense at low frequencies. These measurements led the authors to conclude that the AKR generation region rises upward along the flux tube in summer. This results from the heating of the ionosphere under solar radiation and, as a consequence, an increase in the fluxes of charged particles rising from the ionosphere. The increase in the plasma density produced by rising fluxes leads to a violation of the AKR generation conditions at low altitudes.

In our experiment, we observed similar spectral variations with geomagnetic activity. This could be because the properties of the auroral ionosphere depend strongly on the fluxes of precipitating particles. Precipitating energetic particles cause a heating of the ionosphere and an increase in its density similar to the variations in ionospheric parameters under solar radiation. Such changes in the ionosphere increase the fluxes of rising particles, which, in turn, leads to an increase in the altitude of the AKR generation region. The rising fluxes have a stronger effect at low altitudes, because for an isotropic particle velocity distribution in the ionosphere, only a small fraction of them will reach the altitudes of the upper AKR generation boundary. Thus, the mechanism of the AKR spectral variation with geomagnetic activity is similar to the mechanism of seasonal variations suggested by Green *et al.* (2004).

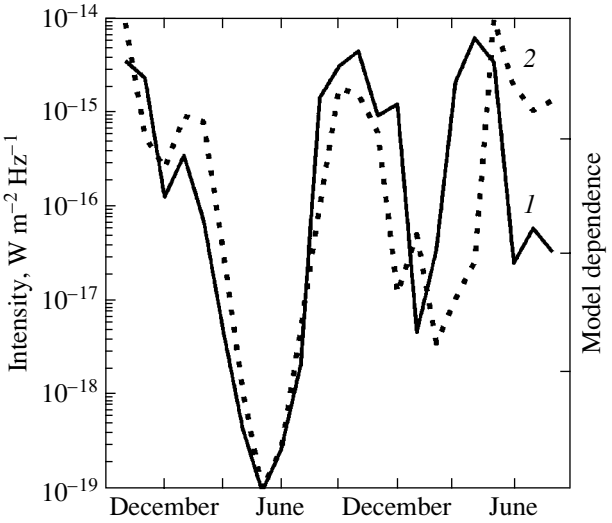

Fig. 4. Comparison of the model intensity with the results of the AKR measurements at 300 kHz during two years (October 1996–August 1998); *1*—the measurements (left scale); *2*—the model dependence of the AKR intensity calculated using formula (2).

In general, the results of our analysis of the seasonal AKR intensity variations recorded on the INTERBALL-2 satellite agree closely with previous measurements. The difference between the modulation depths of the AKR intensity at 50 and 300 kHz is attributable to different AKR generation altitudes at these frequencies and to the higher noise level at low frequencies. The frequency of 50 kHz is generated at lower altitudes, closer to the ionosphere and, accordingly, in a region with a higher plasma density. Therefore, even at the same fluxes of energetic particles, the AKR intensity at 50 kHz is lower than that at higher frequencies.

ACKNOWLEDGMENTS

We are grateful to T.V. Romantsova and A.A. Rusanov for their help with the data analysis. This

work was supported by the Russian Foundation for Basic Research (project no. 02-02-17553a) and a Presidential grant for Support of Leading Scientific Schools (no. NSh-1739.2003.2).

REFERENCES

1. E. A. Benediktov, G. G. Getmantsev, N. A. Mityakov, *et al., Space Research*, Ed. by G. A. Skuridin (Nauka, Moscow, 1965), p. 581 [in Russian].
2. E. A. Benediktov, G. G. Getmantsev, N. A. Mityakov, *et al.*, Kosm. Issled. **6**, 946 (1968) [Cosmic Res. **6**, 791 (1968)].
3. W. Calvert, J. Geophys. Res. **92**, 1267 (1987).
4. R. E. Ergun, C. W. Carlson, J. P. McFaden, *et al.*, Astrophys. J. **538**, 456 (2000).
5. A. A. Galeev, Yu. I. Gal'perin, and L. M. Zelenyĭ, Kosm. Issled. **34**, 339 (1996) [Cosmic Res. **34**, 313 (1996)].
6. J. L. Green, S. Boardsen, L. Garcia, *et al.*, J. Geophys. Res. **109**, A05223 (2004).
7. D. A. Gurnett, J. Geophys. Res. **79**, 4227 (1974).
8. J. Hanasz, Z. Kravchik, and M. M. Mogilevsky, Kosm. Issled. **36**, 617 (1998) [Cosmic Res. **36**, 575 (1998)].
9. J. Hanasz, M. Panchenko, H. de Feraudy, *et al.*, J. Geophys. Res. **108**, 1408 (2003).
10. Y. Kasaba, H. Matsumoto, K. Hashimoto, and R. R. Anderson, Geophys. Res. Lett. **24**, 2483 (1997).
11. A. Kumamoto, T. Ono, M. Iizima, and H. Oya, J. Geophys. Res. **108**, 1032 (2003).
12. A. Kumamoto and H. Oya, Geophys. Res. Lett. **25**, 2369 (1998).
13. W. S. Kurth and D. A. Gurnett, Adv. Space Res. **22**, 73 (1998).
14. I. L. Moiseenko, in *Proceedings of the Conference of Young Scientists Devoted to the Day of Cosmonautics* (Inst. Kosm. Issled. Ross. Akad. Nauk, Moscow, 2004), p. 20.
15. R. R. Nazirov and V. I. Prokhorenko, Kosm. Issled. **36**, 311 (1998) [Cosmic Res. **36**, 292 (1998)].
16. A. Olson, P. Janhunen, M. Mogilevsky, *et al.*, Ann. Geophys. **22**, 3571 (2004).
17. P. L. Pritchet, R. Strangewey, C. W. Carlson, *et al.*, J. Geophys. Res. **104**, 10 317 (1999).
18. G. R. Voot, D. A. Gurnett, and S.-P. Akasofu, J. Geophys. Res. **82**, 2259 (1977).
19. C. S. Wu and L. C. Lee, Astrophys. J. **230**, 621 (1979).
20. V. V. Zaĭtsev, V. E. Shaposhnikov, and Kh. O. Ruker, Astron. Zh. **80**, 761 (2003) [Astron. Rep. **47**, 701 (2003)].
21. P. Zarka, J. Geophys. Res. **103**, 20159 (1998).

Translated by G. Rudnitskiĭ

Astronomy Letters, Vol. 31, No. 6, 2005, p. 427.

ERRATA

Erratum: "Study of the Optical Variability of T Tau in the Period 1962–2003" [*Astron. Lett.* 31 (2), 109 (2005)]

S. Yu. Mel'nikov and K. N. Grankin

There was a misprint in the final pages (in both the Russian and English versions): Instead of October 5, 1999, the text should have read September 5, 1999 (see the description in the text and the caption to Fig. 2).